

Masing and Non-Masing Behaviors of Materials under Low Cycle Fatigue Loading

Doctoral Thesis

by

Sanjeev Singh Yadav

Roll Number: 2018MEZ0004



DEPARTMENT OF MECHANICAL ENGINEERING
INDIAN INSTITUTE OF TECHNOLOGY ROPAR

October, 2023

**Masing and Non-Masing Behaviors of Materials under Low Cycle
Fatigue Loading**

A Thesis Submitted
In Partial Fulfillment of the Requirements
for the Degree of

DOCTOR OF PHILOSOPHY

by

Sanjeev Singh Yadav

Roll Number: 2018MEZ0004



DEPARTMENT OF MECHANICAL ENGINEERING
INDIAN INSTITUTE OF TECHNOLOGY ROPAR

October, 2023

Sanjeev Singh Yadav: Masing and Non-Masing Behaviors of Materials under Low Cycle
Fatigue Loading

Copyright ©2023, Indian Institute of Technology Ropar, All Rights Reserved.

Dedicated to

My dear Parents

(Mr. M. S. Yadav & Mrs. Sudha Yadav)

Respected Teachers

(For your kind help, faith, encouragement, and guidance)

Beloved Wife

(Mrs. Mamta Yadav)

Brother

(Mr. R. S. Yadav)

Son

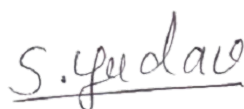
(Shivansh)

and

My Friends

Declaration of Originality

I hereby declare that the work being presented in the thesis entitled **Masing and Non-Masing Behaviors of Materials under Low Cycle Fatigue Loading** has been authored by me. It presents the result of my own independent investigation/research conducted during the time period from **July 2018** to **May 2023**. Thesis submission under the supervision of **Dr. Samir Chandra Roy**, Assistant Professor, Department of Mechanical Engineering, Indian Institute of Technology Ropar. To the best of my knowledge, it is an original work, both in terms of research content and narrative, and has not been submitted or accepted elsewhere, in part or in full, for the award of any degree, diploma, fellowship, associateship, or similar title of any university or institution. Further, due credit has been attributed to the relevant state-of-the-art collaborations (if any) with appropriate citations and acknowledgments in line with established ethical norms and practices. I also declare that any idea/data/fact/source stated in my thesis has not been fabricated/falsified/misrepresented. All the principles of academic honesty and integrity have been followed. I fully understand that if the thesis is found to be unoriginal, fabricated, or plagiarized, the Institute reserves the right to withdraw the thesis from its archive and revoke the associated Degree conferred. Additionally, the Institute also reserves the right to appraise all concerned sections of society of the matter for their information and necessary action (if any). If accepted, I hereby consent for my thesis to be available online in the Institute's Open Access repository, inter-library loan, and for the title & abstract to be made available to outside organizations.



Signature

Name: **Sanjeev Singh Yadav**

Entry Number: **2018MEZ0004**

Program: **Ph.D.**

Department: **Mechanical Engineering**

Indian Institute of Technology Ropar

Rupnagar, Punjab 140001, India

Date:

Certificate

This is to certify that the thesis entitled **Masing and Non-Masing Behaviors of Materials under Low Cycle Fatigue Loading**, submitted by **Sanjeev Singh Yadav (2018MEZ0004)** for the award of the degree of **Doctor of Philosophy** of Indian Institute of Technology Ropar, is a record of bonafide research work carried out under my guidance and supervision. To the best of my knowledge and belief, the work presented in this thesis is original and has not been submitted, either in part or full, for the award of any other degree, diploma, fellowship, associateship or similar title of any university or institution.

In my opinion, the thesis has reached the standard fulfilling the requirements of the regulations relating to the Degree.



Signature of the Supervisor

Dr. Samir Chandra Roy

Department of Mechanical Engineering

Indian Institute of Technology Ropar

Rupnagar, Punjab 140001, India

Date: 19/10/2023

Acknowledgment

This journey has been a great challenge. However, the journey would not have been possible without adequate help, moral support, and motivation from my family members, especially my parents, beloved wife, brother, and other members. So, I first take the opportunity to thank and express my gratitude to them. I will always be grateful to them for their unconditional affection and support.

First and foremost, I would like to thank the thesis advisor, **Dr. Samir Chandra Roy**, Assistant Professor, Department of Mechanical Engineering, Indian Institute of Technology (IIT), Ropar. This project would not have been possible without his help and guidance. I appreciate his valuable help and support during this work. I also take the opportunity to thank the various scientists who made contributions to the field of materials' Masing/non-Masing behavior. I want to extend my respect and gratitude to the Chairman of the Doctoral Committee (DC): **Dr. Ekta Singla**, and other DC members, **Dr. Sachin Kumar**, **Dr. Prabir Sarkar**, and **Dr. Muthulingam Subramaniyan** for their valuable suggestions. I would like to extend my greatest respect and gratitude to the reviewers of dissertation: **Prof. Takashi Nakamura**, Professor, Division of Mechanical Engineering, Hokkaido University, Japan and **Prof. S. Ganesh Sundara Raman**, Department of Metallurgical and Materials Engineering, IIT Madras, India, for their careful reading, valuable suggestions, and recommendation.

I am honored to express my gratitude and thank **Dr. Sunil Goyal**, Scientific Officer (G), Nuclear Fuel Complex, Kota Project, Rawatbhata, Rajasthan, for his help during the journey, especially for many fruitful discussions, suggestions, and ideas to overcome some problems during the research. I also take this opportunity to thank **Dr. A. Nagesha**, Scientific Officer (G), IGCAR Kalpakkam, for his support and encouragement during the progress of this work. I sincerely thank **Mr. J. Veerababu** (Scientific Officer), IGCAR Kalpakkam, for his help in conducting the LCF tests. I want to thank **IIT Ropar** for the fellowship and **MBRL** for providing infrastructural support for this investigation. I would also like to thank the **HOD** and **faculty members** of Mechanical Engineering Department, IIT Ropar, for their help. The help received from **technical staffs** and **workshop members** of Mechanical Engineering, are acknowledged with sincere thanks.

The help extended by my colleagues (**Er. Neha Mehani**, **Er. Himanshu Mardanday**, **Er. Rajat Dhiman**, **Er. Nikhil Suman**, **Er. Ashish Kumar**, **Er. Subha Nath**, and **Er. Manish Kumar**) at IIT Ropar is greatly appreciated. These friends have always extended their hands of cooperation without any hesitation. The discussion with them was very fruitful and appreciated. At this moment, I would like to thank **Er. Amanpreet Chander** for his help and support. I also would like to thank my dear friends, **Mr. Rohit Parihar**, **Mr. Gaurav Soni**, **Er. Sumit Devraye**, **Er. Rajneesh Gupta**, **Er. Jitendra Chauhan**, **Er. Rakesh Choudhary**, **Er. Souvik Gantait**, **Er. Sourabh Gupta**, **Er. Abhiram Singhanian**, **Er. Atul Kumar Choudhary**, and **Er. Uttam Kachhawah**. Finally, I would like to thank to everyone for their help and support during the different stages of this journey.

Lay Summary

Have you ever thought about how gold/silver could be drawn into a wire? Why did the comet jet airliner fail? What was the reason behind the sinking of the titanic ship? Well, all these questions can be answered with some knowledge of the “Deformation Mechanism of Materials.” Understanding the deformation behavior of the material is crucial for designing and developing advanced materials, which are required to meet the upcoming energy demand of India and the world. India has been planning to install more nuclear power plants in the country because nuclear power plants would help to get a status of carbon neutral country well before 2070 (target set by Ministry of Environment, Forest and Climate Change, Government of India). Several materials are used in the nuclear power plant’s components; however, stainless steel (304L) has been considered a primary structural material due to its good mechanical properties, corrosion resistance, and low cost. As we feel tiredness (or fatigue) after doing some work, materials also during their service experience fatigue, which is detrimental to material strength and component’s life. Therefore, the comprehensive study of fatigue life assessment methods and different microstructural aspects of 304L SS and other materials is vital for designing a safe, long-lasting nuclear power plant that meets the safety standards. Thus, an effort has been made to investigate the materials' strain-controlled fatigue behavior with a special emphasis on the Masing and non-Masing behaviors.

In this investigation, fatigue tests were performed at room temperature on 304L SS specimens, and then analysis of different types of LCF behavior (Masing and non-Masing) was done for 304L SS and 12 other materials. A material behavior is said to be Masing when the loading branches of the hysteresis loops follow the same loading curve irrespective of strain amplitude, otherwise it is called non-Masing. Based on the comprehensive analysis, a model has been proposed to predict the cyclic plastic strain energy density (CPSED) and, thereby, the fatigue life of materials under LCF loading, irrespective of Masing or non-Masing behavior. The proposed model is a simple and handy relationship that requires a few LCF tests (at least three) data to estimate the material constants; then, it can be used to predict the CPSED and fatigue life for any unknown amplitude. Thus, the developed model can assess the fatigue life of various materials used in different industries, from structural to nuclear power plants. Further, the different microstructural aspects of the deformation behavior of the 304L SS have been studied using various experimental techniques and numerical simulation. The fundamental causes of the different kinds of deformation behavior (namely the Type-I and Type-II non-Masing) have been identified by analyzing the internal structure and defects of 304L SS at different life fractions. The qualitative correlation between the mechanical response of 304L SS and the material internal state variables has been established. The developed qualitative correlation is a step forward to establishing the empirical relation/phenomenological relationship, which would help to establish a quantitative correlation or develop a constitutive model for predicting fatigue behavior under realistic loading conditions. This study contributes toward developing the microstructural-based constitutive model to predict the actual behavior of materials under fatigue.

Abstract

Understanding the material's Masing/non-Masing behavior has immense significance in the plastic strain energy density-based fatigue life prediction methods, constitutive model development, and design/selection of advanced materials for extreme environmental conditions. Low cycle fatigue (LCF) tests were performed on 304L SS at room temperature, applying strain amplitude ranging from $\pm 0.25\%$ to $\pm 1.0\%$ at a strain rate of $1 \times 10^{-3} \text{ s}^{-1}$. The Masing/non-Masing behavior has been investigated at 5%, 8%, 10%, 12%, 15%, 20%, 30%, 40%, and 50% of fatigue life. It was observed that the master curve could be constructed with the hysteresis loops at lower fractions of fatigue life (up to 10%); however, the master curve could not be constructed at life fractions higher than 10%. Therefore, the non-Masing behavior of the material has been classified into two types, viz. Type-I non-Masing behavior (i.e., when construction of the master curve is possible) and Type-II non-Masing behavior (i.e., when construction of the master curve is not possible). Further, a model has been proposed to quantify and predict the cyclic plastic strain energy density (CPSED) and fatigue life for Type-II non-Masing behavior, which can also be used for Type-I non-Masing and Masing behavior. This model has been validated with 13 different types of materials and could predict the CPSED and fatigue life within a scatter band of 1.2 and 2, respectively.

The interrupted LCF tests were conducted at the strain amplitudes of $\pm 0.25\%$, $\pm 0.6\%$, and $\pm 1.0\%$ for life fractions up to 8%, 30%, and 50%, and detailed microstructural investigations were done to explore the underlying cause of the Type-I and Type-II non-Masing behavior. The dislocation tangles, deformation twins, less local misorientation, and minimal martensite were observed at a low life fraction (8%), causing Type-I non-Masing behavior. However, at higher life fractions (30% and 50%), a high amount of martensite, high dislocation density, high local misorientation, stacking faults, deformation twins, shear bands, and cells have caused the Type-II non-Masing behavior. Further, these microstructural variables have been qualitatively correlated with the proportional stress limit and strain hardening rate behavior. It is concluded that the proportional stress limit changes in Type-I, whereas for Type-II, the proportional stress limit and the strain hardening rate behavior change with strain amplitude. However, neither the proportional stress limit nor the strain hardening rate behavior changes with strain amplitude for Masing behavior. The effect of the martensite on the cyclic plastic deformation behavior has been analyzed using 2D numerical simulation in the finite element analysis tool ABAQUS. The strain localization, equivalent plastic strain, and effective stress increase with the increase in martensite content in 304L SS. This type of plastic strain localization would promote more martensitic transformation and, thereby, changes in the material's strain hardening rate and mechanical properties, leading to non-Masing behavior. This study contributes fundamental understanding toward developing the microstructural-based robust phenomenological model to predict the non-Masing behavior of materials under low cycle fatigue.

List of publications

Journals

1. **S. S. Yadav**, S. C. Roy, J. Veerababu, S. Goyal, Quantitative Assessment and Analysis of Non-Masing Behavior of Materials under Fatigue, Journal of Materials Engineering & Performance 30: 2021; 2102–2112. <https://doi.org/10.1007/s11665-021-05494-w>.
2. **S. S. Yadav**, S. C. Roy, J. Veerababu, S. Goyal, Prediction of Cyclic Plastic Strain Energy Density and Fatigue Life of Non-Masing Behavior Materials Without Master Curve, Transaction of the Indian National Academy of Engineering, 7: 2022; 411–416. <https://doi.org/10.1007/s41403-021-00274-3>.
3. **S. S. Yadav**, S. C. Roy, S. Goyal, A comprehensive review and analysis of Masing/non-Masing behavior of materials under fatigue, Fatigue & Fracture of Engineering Materials & Structures, 46: 2023; 759–783. <https://doi.org/10.1111/ffe.13906>.
4. **S. S. Yadav**, S. C. Roy, J. Veerababu, S. Goyal, Type-I to Type-II non-Masing behavior of 304L SS under low cycle fatigue: Material's internal changes, International Journal of Fatigue, 175: 2023; 107789. <https://doi.org/10.1016/j.ijfatigue.2023.107789>.
5. **S. S. Yadav**, S. C. Roy, P. C. Chakraborti, “Influence of Deformation-Induced Martensite on Non-Masing Behavior of 304L Stainless Steel” (To be submitted)

Table of contents

Declaration	iv
Certificate	v
Acknowledgment	vi
Lay Summary	vii
Abstract	viii
List of Publications	ix
List of Figures	xiii
List of Tables	xix
Notations and Abbreviations	xx
Preface	xxiii
1. Literature Survey	1
1.1 Introduction	2
1.2 Material behavior under LCF	6
1.3 Factors affecting the Masing/non-Masing behavior of materials	9
1.3.1 Influence of the stacking fault energy (SFE)	9
1.3.2 Influence of temperature	11
1.3.3 Influence of strain amplitude	14
1.3.4 Influence of loading conditions	17
1.4 Assessment of Masing/non-Masing response	20
1.4.1 Bauschinger strain method	20
1.4.2 Probability density function (PDF)	22
1.4.3 Change in proportional stress limit ($\delta\sigma_0$)	24
1.4.4 CPSED Method	26
1.5 Constitutive modeling	26
1.6 Fatigue life prediction of non-Masing behavior	29
1.7 Summary and conclusions	30
1.8 Research scope and objectives	32
1.9 Some highlights and remarks	33
2. Mechanistic Analysis	35
2.1 Introduction	36
2.2 Experimental details	37
2.3 Results	38
2.3.1 Cyclic stress response	38

2.3.2 Assessment of non-Masing behavior	40
2.3.3 Proposed model for estimation of CPSED and fatigue life	41
2.3.4 Validation of proposed model	46
2.4 Discussion	48
2.5 Superiority of the proposed model	51
2.6 Summary and conclusions	52
2.7 Some highlights and remarks	53
3. Validation of Proposed Model	55
3.1 Introduction	56
3.2 Test data	57
3.3 Results and discussion	57
3.3.1 Analysis of non-Masing behavior	57
3.3.2 Validation of the proposed model	58
3.4 Summary and conclusions	60
3.5 Some highlights and remarks	61
4. Microstructural Investigation	63
4.1 Introduction	64
4.2 Experimental details	65
4.2.1 Material and specimen	65
4.2.2 LCF testing	65
4.2.3 Microstructural characterization	65
4.3 Results	66
4.3.1 Cyclic stress response (CSR)	66
4.3.2 Analysis of non-Masing behavior	67
4.3.3 Localized deformation analysis	69
4.3.4 Substructural analysis	73
4.4 Discussion	77
4.4.1 Influence of secondary hardening	77
4.4.2 Influence of martensite fraction	79
4.4.3 Influence of misorientation distribution	80
4.4.4 Influence of strain hardening rate behavior	81
4.5 Qualitative correlation	82
4.6 Summary and conclusions	84
4.7 Some highlights and remarks	85
5. Numerical Simulation	87

5.1 Purpose of investigation	87
5.2 Introduction to constitutive modeling	88
5.3 Simulation methodology	89
5.3.1 2D numerical simulation	89
5.3.2 Combined isotropic and kinematic hardening	92
5.3.3 Determination of material parameters	92
5.4 Results and discussion	93
5.4.1 Hysteresis loop analysis	93
5.4.2 Strain hardening rate	95
5.4.3 Influence of strain amplitude	96
5.4.4 Influence of martensite	97
5.5 Cyclic stress response (CSR)	99
5.6 Summary and conclusions	100
5.7 Some highlights and remarks	101
6. Conclusions and Scope of Future Work	103
6.1 Summary and conclusions	103
6.2 Scope of future work	105
References	107

List of Figures

Figure 1.1	Schematic representation of Masing behavior.	2
Figure 1.2	Schematic representation of Masing behavior with respect to cyclic stress-strain curve. Only two hysteresis loops are shown in the figure.	2
Figure 1.3	Representation of (a) Type-I [19] and (b) Type-II [19] non-Masing behavior of LY225 steel and 304L SS, respectively. First published in [19] [Transactions of the Indian National Academy of Engineering, 7, 411-416, 2022] by Springer Nature.	3
Figure 1.4	Classification of material behavior under low cycle fatigue.	4
Figure 1.5	Variation of the cyclic plastic strain energy density with strain amplitude for Masing and non-Masing behaviors of three different materials. The plots are generated by extracting the data for LY225 steel [5], BLY160 steel [8], and AISI 321 SS [6]. The data for Masing behavior were obtained by constructing the hysteresis loops for an idealized Masing behavior of the materials, as discussed in the article [7].	4
Figure 1.6	Dislocation cell formation in aluminum (high SFE material) for strain amplitude of $\pm 1.0\%$ (a) after the onset of saturation (30 cycles) shows random cell structure [15]; (b) after failure (11,300 cycles) shows well-defined cell structure [15]. Reprinted from Plumtree and Abdel-Raouf [15] and with permission from Elsevier.	10
Figure 1.7	Influence of the stacking fault energy on materials' Masing/non-Masing behavior. Note: LSFE = low stacking fault energy, ISFE = intermediate stacking fault energy, HSFE = high stacking fault energy.	10
Figure 1.8	Dislocation substructure in 316LN SS during deformation at (a) $\pm 0.4\%$ and (b) $\pm 0.8\%$ strain amplitude at 600°C [28]. Reprinted from Goyal et al. [28] and with permission from Elsevier.	11
Figure 1.9	Schematic representation of various loading sequences (a) constant step test, (b) increment step test, and (c) decremental step test.	18
Figure 1.10	TEM pictures show the dislocation cell structure development in 304LN SS at strain amplitudes of (a) $\pm 0.85\%$ and (b) $\pm 1.0\%$ [30]. Reprinted from Sivaprasad et al. [30] and with permission from Elsevier.	18
Figure 1.11	Fishbone diagram representing the parameters that affect the Masing/non-Masing behavior. Note: CST = constant step test, IST =	19

incremental step test, DST = decremental step test, SFE = stacking fault energy.

Figure 1.12	Schematic representation of the Bauschinger strain. (Note: σ_{\max} = peak tensile stress, ε_t = total strain amplitude, and β = Bauschinger strain).	21
Figure 1.13	Variation of Bauschinger strain with plastic strain range for different materials [47]. The plots are generated by extracting the data for 2024-T6 aluminum, 1018 steel, A36 steel, and 1018 hot rolled steel from the article [47].	21
Figure 1.14	Schematic representation of the Masing model (elastic-perfectly plastic elements).	22
Figure 1.15	Probability density distribution for 304LN SS steel showing non-Masing behavior [30]. Reprinted from Sivaprasad et al. [30] and with permission from Elsevier.	24
Figure 1.16	Schematic representation of the change in the proportional stress limit ($\delta\sigma_0$) with strain amplitude.	25
Figure 1.17	Variation of change in proportional stress limit ($\delta\sigma_0$) with strain amplitude for different materials.	25
Figure 1.18	Simulated hysteresis loops of (a) 1 st cycle, (b) 10 th cycle, and (c) 20 th cycle of initial cyclic hardening period at different strain amplitudes.	28
Figure 1.19	Highlights of different components associated with Masing/non-Masing behavior.	31
Figure 2.1	Low cycle fatigue testing specimen.	38
Figure 2.2	(a) The variation of peak tensile stress with cyclic loading at different strain amplitudes for 304L SS fatigue tested at room temperature. Initial hardening, softening and secondary hardening regions are marked by different σ -terms for $\pm 1.0\%$ of strain amplitude, (b) variation of degree of initial hardening (DOIH), degree of softening (DOS), and degree of secondary hardening (DOSHS) of 304L SS with strain amplitude.	39
Figure 2.3	Variation of the martensite content with strain amplitude at the fracture surface and two different locations, 2 mm and 10 mm away from the fracture surface.	40
Figure 2.4	Hysteresis loops of 304L SS fatigue tested at different life fractions ((a) 10% and (b) 50%) translated to generate the master curves.	41

Figure 2.5	Schematic representation of different types of hysteresis loops for calculation of the plastic strain energy density for Masing and non-Masing behaviors.	42
Figure 2.6	(a) Hysteresis loops constructed by extrapolation of the loading branch of the experimental hysteresis loop from $\pm 0.25\%$ strain amplitude represent an ideal Masing behavior and (b) variation of plastic strain range with total strain range.	43
Figure 2.7	(a) The variation of normalized CPSED difference with strain amplitude for 304L SS, (b) comparison of the predicted and the experimental cyclic plastic strain energy densities for the 304L SS.	44
Figure 2.8	(a) Predicted cyclic plastic strain energy density vs. experimental fatigue life plots for 304L SS material, (b) comparison of the experimental and predicted fatigue lives.	45
Figure 2.9	(a) Normalized CPSED difference vs. strain amplitude plots for all materials. Linear fit curves are also shown, (b) comparison of the predicted and the experimental cyclic plastic strain energy densities of the hysteresis loops for all materials.	47
Figure 2.10	(a) Predicted cyclic plastic strain energy density vs. experimental fatigue life plots for all materials, (b) comparison of the experimental and predicted fatigue lives for all materials.	48
Figure 2.11	Comparison of experimental and predicted values of cyclic plastic strain energy densities. The prediction was made by using the existing method (master curve approach: Equation 2.13).	49
Figure 2.12	(a) Predicted cyclic plastic strain energy density vs. experimental fatigue life plots for all materials. The prediction of CPSED was made by using the existing method (master curve approach: Equation 2.13), (b) comparison of experimental and predicted fatigue lives. The prediction was made by using the existing method (master curve approach Equation 2.13).	49
Figure 2.13	Comparison of error percentage in the prediction of (a) CPSED and (b) fatigue life obtained by the proposed new method and the existing method (master curve approach). Total number of data points is 50 in each plot.	50

Figure 3.1	Representation of (a) Type-I and (b) Type-II non-Masing behavior for LY225 steel [5] and 304L SS [7], respectively.	57
Figure 3.2	Construction of master curve at half-life for two different materials (a) BLY160 steel [8] and (b) AISI 321 SS [6].	58
Figure 3.3	Variation of E_f with strain amplitude for different materials.	58
Figure 3.4	(a) Variation of plastic strain range with total strain range (b) comparison of predicted and experimental CPSED for six different materials.	59
Figure 3.5	(a) Variation of predicted CPSED with number of cycles to failure (b) comparison of the experimental and predicted fatigue life for different materials.	59
Figure 4.1	(a) Peak stress variation with the number of cycles obtained from the full-life and interrupted (8%, 30%, and 50% of life fractions) LCF tests. The solid lines indicate the full-life tests performed until specimen failure, and the lines with symbols indicate the interrupted LCF tests. (b) variation of martensite content with strain amplitudes at different locations (midpoint and 10 mm away from midpoint) of the specimens for different life fractions. Note: LF = life fraction.	67
Figure 4.2	Construction of master curve for different life fractions (a) 5%, (b) 8%, (c) 10%, (d) 12%, (e) 15%, (f) 20%, (g) 30%, (h) 40%, and (i) 50%.	68
Figure 4.3	Construction of master curve from the interrupted test data. Tests were conducted for life fractions of (a) 8% (Type-I), (b) 30% (Type-II), and (c) 50% (Type-II).	68
Figure 4.4	Representation of the (a) image quality (IQ) map, (b) kernel average misorientation (KAM) map, and (c) inverse pole figure (IPF) of the untested sample.	69
Figure 4.5	Representation of (a-c) image quality maps, (d-f) kernel average misorientation maps, and (g-i) phase maps at different life fractions at the strain amplitude of $\pm 0.25\%$.	70
Figure 4.6	Representation of (a-c) image quality maps, (d-f) kernel average misorientation maps, and (g-i) phase maps at different life fractions at the strain amplitude of $\pm 0.6\%$.	71
Figure 4.7	Representation of (a-c) image quality maps, (d-f) kernel average misorientation maps, and (g-i) phase maps at different life fractions at the strain amplitude of $\pm 1.0\%$	72

Figure 4.8	TEM images of an untested sample of 304L SS showing the (a) low dislocation density, (b) magnified view of the highlighted region in image (a).	74
Figure 4.9	TEM images showing the internal state of 304L SS at life fractions of (a-c) 8%, (d-f) 30%, and (g-i) 50%, fatigue tested at the strain amplitude of $\pm 0.25\%$.	74
Figure 4.10	TEM images showing the internal state of 304L SS at life fractions of (a-c) 8%, (d-f) 30%, and (g-i) 50%, fatigue tested at the strain amplitude of $\pm 0.6\%$.	75
Figure 4.11	TEM images showing the internal state of 304L SS at life fractions of (a-c) 8%, (d-f) 30%, and (g-i) 50%, fatigue tested at the strain amplitude of $\pm 0.1\%$. Note: DT = deformation twins, SBs = shear bands.	76
Figure 4.12	(a) Variation of peak stress with the number of cycles. The dotted line connects the data points at 10% of fatigue life for different strain amplitudes. (b) variation of the number of cycles at the onset of secondary hardening with strain amplitude.	78
Figure 4.13	Variation of the (a) twin fraction and (b) martensite content (phase fraction) with life fraction at different strain amplitudes.	79
Figure 4.14	(a) KAM profile for different life fractions at various strain amplitudes (b) The average KAM value with life fraction at $\pm 1.0\%$ strain amplitude. Note: LF = life fraction, SA = strain amplitude.	80
Figure 4.15	Variation of the strain hardening rate behavior with true strain for different strain amplitudes at life fractions of (a) 10% and (b) 50%.	81
Figure 4.16	Schematic illustration of life fraction and strain amplitude effect on internal state variables of 304L SS fatigue tested at room temperature.	82
Figure 4.17	Qualitative correlation between the internal state variables and Masing/non-Masing behavior of materials under fatigue loading. Note: ε = strain amplitude, $\delta\sigma_0$ = change in proportional stress limit.	83
Figure 5.1	Schematic representation of the 2D model and boundary conditions used for numerical simulation of LCF of 304L SS. The circles indicate the martensite phase.	90
Figure 5.2	Schematic representation of various models considered for the numerical simulation of 304L SS with varying percentages of austenite	91

(A) and martensite (M); (a) 0.45% M + 99.55% A, (b) 4.34% M + 95.66% A, (c) 7.84% M + 92.16% A, and (d) 8.75% M + 91.25% A.

- Figure 5.3** Comparison of the simulated and experimental hysteresis loops of 304L SS at $\pm 1.0\%$ of strain amplitude, (a) first hysteresis loop and (b) first ten hysteresis loops. 94
- Figure 5.4** Comparison of the simulated hysteresis loop of 1st cycle at (a) $\pm 0.6\%$ and (b) $\pm 1.0\%$ of strain amplitudes for different martensite fractions. Note: Hysteresis loops of austenite (A) and martensite (M) phase are shown. 94
- Figure 5.5** The stress/strain fields developed around the martensite phase at $\pm 0.6\%$ of strain amplitude in 304L SS; (a) von Mises stress (MPa) and (b) equivalent plastic strain (PEEQ). Note: X is the loading direction, and the plastic strain is PE11 i.e. along X-direction and on a plane normal to X. 95
- Figure 5.6** (a) First quarter parts of the simulated hysteresis loops at $\pm 0.6\%$ and $\pm 1.0\%$ of strain amplitudes for different martensite fractions (b) magnified view of the plastic region in (a) 96
- Figure 5.7** Variation of the plastic strain, von Mises stress (MPa), and equivalent plastic strain (PEEQ) distribution for 0.45% martensite fraction at the strain amplitudes of (a-c) $\pm 0.6\%$ and (d-f) $\pm 1.0\%$. Note: X is the loading direction, and the plastic strain is PE11 i.e. along X-direction and on a plane normal to X. 97
- Figure 5.8** Variation of the plastic strain, von Mises stress (MPa), and equivalent plastic strain distribution at $\pm 0.6\%$ of strain amplitude for martensite fractions of (a-c) 0.45% and (d-f) 4.34%. Note: X is the loading direction, and the plastic strain is PE11 i.e. along X-direction and on a plane normal to X. 98
- Figure 5.9** Variation of plastic strain, von Mises stress (MPa), and equivalent plastic strain at $\pm 1.0\%$ of strain amplitude for martensite fractions of (a-c) 0.45%, (d-f) 7.84%, and (g-i) 8.75%. Note: X is the loading direction, and the plastic strain is PE11 i.e. along X-direction and on a plane normal to X. 99
- Figure 5.10** (a) The variation of peak tensile stress with martensite fraction for 100 cycles at different strain amplitudes, and (b) variation of the equivalent plastic strain (PEEQ) with the number of cycles for different martensite fractions at $\pm 0.6\%$ and $\pm 1.0\%$ of strain amplitude. 100

List of Tables

Table 1.1	The landmark developments in the field of Masing/non-Masing behavior	7
Table 1.2	Microstructural factors responsible for Masing/non-Masing behavior of various materials under different conditions	12
Table 1.3	The critical strain amplitude for Masing/non-Masing behavior of various materials under fatigue	15
Table 2.1	The source of the extracted LCF data and the estimated values of the different constants associated with the proposed and existing methods	46
Table 3.1	The various constants estimated for the different materials	60
Table 4.1	Variation of the fraction of LAGBs, twin fraction, martensite fraction, and average KAM for various life fractions at different strain amplitudes.	73
Table 5.1	Martensite fraction (%Vol.) at different fatigue life at different strain amplitudes, measured at the midpoint of gage length of the fatigue tested sample	91
Table 5.2	Material parameters of austenite and martensite used for the numerical simulation	93

Notations and Abbreviations

Symbol	Description
b	Rate at which the isotropic function attains the saturation value
d	Distance from the midpoint of the gage
C	Kinematic hardening modulus
E	Modulus of elasticity
f	Yield function
$f(\sigma_{yt})$	Probability density function
K	Cyclic strain hardening coefficient for ideal Masing behavior
K_1	Material constant, the coefficient obtained from Equation 2.11
K'	Cyclic strain hardening coefficient of the master curve for non-Masing behavior
M_d	Martensite transformation limiting temperature
M_s	Martensite start temperature during stress/strain-induced transformation
n	Cyclic strain hardening exponent for ideal Masing behavior
n_1	Material constant, the exponent obtained from Equation 2.11
n'	Cyclic strain hardening exponent of the master curve for non-Masing behavior
N_f	Number of cycles to failure
$N_{f,exp}$	Experimental fatigue life of the material
$N_{f,pre}$	Predicted fatigue life of the material
p	Accumulated plastic strain
Q	Maximum value of isotropic hardening function
$r(p)$	Isotropic hardening function
S_1, S_2	Material constants, the coefficient obtained from Equation 2.4
S_3, S_4	Material constants used in Equation 2.9
E_f	Normalized cyclic plastic strain energy density difference
E_m	Cyclic plastic strain energy density for Masing behavior
$E_{nm,exp}$	Experimental cyclic plastic strain energy density for non-Masing behavior
$E_{nm,pre}$	Predicted CPSED for non-Masing behavior
$E_{nm(I)}$	Cyclic plastic strain energy density of Type-I non-Masing behavior

σ_{\max}	Maximum tensile stress
σ_y	Yield strength
$\sigma_1, \sigma_2, \sigma_3, \sigma_4$	Stress corresponds to the onset of the initial hardening, softening, saturation, and secondary hardening, respectively
α'	Back stress tensor
β	Bauschinger strain
ε	Strain amplitude
γ	Rate of saturation of back stress
ε^p	Plastic strain increment
ε_p	Plastic strain
ε_t	Total strain amplitude
ν	Poisson ratio of material
ΔE	Extra CPSED due to non-Masing behavior
$\Delta \varepsilon_p$	Plastic strain range
$\Delta \varepsilon'_p$	Plastic strain range of the master curve for non-Masing behavior
$\Delta \varepsilon_t$	Total strain amplitude range
σ'	Deviatoric stress tensor
$\Delta \sigma$	Stress range
$\delta \sigma_o$	Change in proportional stress limit due to non-Masing behavior

Abbreviation	Description
AISI	American Iron and Steel Institute
ASTM	American Society for Testing and Materials
CPSED	Cyclic plastic strain energy density
CSR	Cyclic stress response
CST	Constant step test
CW	Cold work
DIM	Deformation induced martensite
DOIH	Degree of initial hardening
DOS	Degree of softening
DOSH	Degree of secondary hardening
DP	Dual Phase
DSA	Dynamic strain aging
DST	Decremental step test

DTs	Deformation twins
EBSD	Electron backscatter diffraction
FCC	Face centered cubic
FN	Ferrite number
FWHM	Full width at half maximum
GBs	Grain boundaries
HAGBs	High angle grain boundaries
HSFE	High stacking fault energy
IPF	Inverse pole figure
ISFE	Intermediate stacking fault energy
IST	Incremental step test
IQ	Image Quality
KAM	Kernel average misorientation
LAGBs	Low angle grain boundaries
LCF	Low cycle fatigue
LF	Life fraction
LSFE	Low stacking fault energy
ODS	Oxide dispersion strengthened
OIM	Orientation imaging microscopy
PDF	Probability density function
PEEQ	Equivalent plastic strain
PSB	Persistent slip band
RT	Room temperature
SBs	Shear bands
SFs	Stacking faults
SFE	Stacking fault energy
SS	Stainless steel
TBs	Twin boundaries
TEM	Transmission electron microscopy

Preface

This thesis investigates and analyzes materials' Masing/non-Masing behavior under strain-controlled fatigue loading using experimental and numerical simulation techniques. Masing and non-Masing are the two types of material behavior exhibited under low cycle fatigue (LCF), depending on the evolution of the hysteresis loops with strain amplitude. For Masing behavior, the loading branches of the hysteresis loops follow the same path irrespective of strain amplitude, whereas they do not follow the same path in the case of non-Masing behavior. A comprehensive understanding of the Masing/non-Masing behavior is crucial for various reasons, like - (i) the development of constitutive laws for the non-Masing behavior of materials, (ii) the quantification of non-Masing behavior of different classes of materials, (iii) the selection/development of advanced fatigue resistance structures/materials, (iv) identification of the various factors affecting the non-Masing behavior, and (iv) fatigue life prediction.

Researchers worldwide have been working on understanding the Masing/non-Masing behavior of various classes of materials under LCF for over five decades. However, the research was started in the field of Masing/non-Masing a long back with the Bauschinger experiments conducted in 1886 and the proposed Bauschinger effect [1]. Later, Masing [2] tried to model the Bauschinger effect and proposed a Masing hypothesis which states that the proportional stress limit does not change with strain amplitude. In 1984, a breakthrough came in the field of non-Masing behavior when researchers [3] proposed a relationship to estimate the cyclic plastic strain energy density (CPSED) and, subsequently, the fatigue life of the non-Masing behavior.

There are several methods to predict the materials' fatigue life; details are mentioned in the review article [4]. However, the CPSED-based fatigue life prediction is gaining popularity because CPSED considers the influence of strain and stress, and it is a scaler quantity. Therefore, since 1984 many researchers [3,5] have extensively used the CPSED-based fatigue life prediction method. However, it has some drawbacks/limitations. These are (i) the necessity of construction of the master curve for estimation of the CPSED and, thereby, the fatigue life [3]; however, there are materials [6–8] for which the construction of the master curve is not possible, (ii) the available methods can be used only to estimate the CPSED, not for prediction, as the prediction of the change in proportional stress limit ($\delta\sigma_0$) is not possible, and (iii) nonconservative estimation of CPSED and, subsequently, fatigue life [5,9]. Moreover, to the best of our knowledge, systematic and dedicated microstructural investigation of materials' Masing/non-Masing behavior is not available in the open literature. Based on these research gaps/problems associated with the Masing/non-Masing of materials, the objectives of this work

have been formulated to address the abovementioned issues regarding predicting the CPSED and fatigue life of non-Masing behavior. Further, the microstructural investigation and underlying cause of the non-Masing behavior have also been investigated using various experimental and numerical techniques.

In the present study, the Masing/non-Masing behavior has been analyzed at 5%, 8%, 10%, 12%, 15%, 20%, 30%, 40%, and 50% of fatigue life. It was observed that the construction of the master curve is possible up to the fatigue life of 10%, whereas it is not possible beyond the 10% of fatigue life. Masing/non-Masing analysis of 12 more materials has been performed, and it was found that there are two other materials for which the construction of a master curve is not possible [6,8]. Based on the analysis, the non-Masing behavior of the materials has been classified into two categories, viz., (i) Type-I non-Masing behavior (when construction of the master curve is possible) and (ii) Type-II non-Masing behavior (when construction of the master curve is not possible). Further, a model has been proposed to quantify and predict the CPSED and, subsequently, the fatigue life of Type-II non-Masing behavior, which can also be used for Type-I non-Masing behavior and Masing behavior. The proposed model has been validated with 13 different classes of materials and could predict the CPSED and fatigue life within a scatter band of 1.2 and 2, respectively.

The interrupted LCF tests and detailed microstructural investigations at 8%, 30%, and 50% of fatigue lives have been conducted to investigate the underlying cause of the Type-I and Type-II non-Masing behavior. The various internal state variables, such as dislocation tangles, stacking faults, deformation twins, dislocation cells, shear bands, martensite, etc., have been observed, and their dependence on the strain amplitude and life fraction has been investigated. The less microstructural heterogeneity and martensitic transformation led to Type-I non-Masing behavior at the low life fraction of 8%, whereas high microstructural heterogeneity and martensite caused the Type-II non-Masing behavior at the life fractions of 30% and 50%. Further, these internal state variables have been qualitatively correlated with the material's proportional stress limit and strain hardening rate behavior. It is concluded that the proportional stress limit changes in Type-I, whereas for Type-II, the proportional stress limit and the strain hardening rate behavior change with strain amplitude. However, neither the proportional stress limit nor the strain hardening rate behavior changes with strain amplitude for Masing behavior. Based on the experimental finding, it is observed that the martensite content (or fraction) is the dominating internal state variable. Thus, the influence of martensite on cyclic plastic deformation and non-Masing behavior has been investigated and analyzed using finite element simulation in ABAQUS. The results show that the equivalent plastic strain and effective stress localization increase with the increase in martensite content in 304L SS. The higher plastic

strain localization would promote more martensitic transformation and, thereby, changes in the material's strain hardening rate behavior and mechanical properties, leading to non-Masing behavior.

Generally, the materials exhibit Masing/non-Masing behavior under actual/realistic loading conditions, and it is influenced by various external factors. Apart from the above-mentioned findings of this work, the thesis also identifies strain amplitude, temperature, stacking fault energy, and loading condition as the four main external factors influencing the non-Masing behavior under LCF loading. The various assessment methods, such as Bauschinger strain, probability density function, and change in proportional stress limit, have also been identified and discussed in our invited review article [4]. A new assessment method (CPSED method) has been proposed to quantify materials' Masing/non-Masing behavior. It is a simple and versatile method that can be used for Masing, Type-I, and Type-II non-Masing behavior. The thesis comprises chapters, sections, and sub-sections to assemble the scientific observations and findings. The complete research work of the present thesis has been divided into six chapters. A chapter-wise breakup of the proposed thesis work is as follows:

Chapter – 1 Introduction

It briefly introduces the Masing/non-Masing behavior of materials under LCF. It discusses the extensive literature on Masing/non-Masing behavior under different loading conditions. A brief review of the factors that affect the material's Masing/non-Masing behavior and assessment methods of non-Masing behavior are discussed. The modeling aspect of the Masing/non-Masing behavior has also been discussed. Finally, research problems/gaps are highlighted, and the objectives of the thesis have been formulated.

Chapter – 2 Mechanistic Analysis

This chapter discusses the material selection, specimen geometry, heat treatment, and the experimental procedures adopted for LCF testing. Masing/non-Masing analysis has been conducted, and the non-Masing behavior of materials has been classified into two categories, viz., (i) Type-I non-Masing behavior and (ii) Type-II non-Masing behavior. A model has been proposed to predict the CPSED and the fatigue life of different classes of materials. The proposed model has been validated with eight different materials, including Masing, Type-I, and Type-II non-Masing behavior.

Chapter – 3 Validation of Proposed Model

Efforts have been made to identify more materials with Type-II non-Masing behavior from the open literature. As Type-II non-Masing was not reported in the literature, raw data were extracted from the published articles, and Masing/non-Masing behavior was analyzed to identify the materials with Type-I and Type-II behavior. The proposed model of CPSED and

life prediction has been validated with three Type-I and three type-II non-Masing behavior materials. The results presented in this and the previous chapter confirm/demonstrate the applicability of the proposed model for Masing, non-Masing (Type-I and Type-II) behavior.

Chapter – 4 Microstructural Investigation

The microstructural analysis and underlying cause of Type-I and Type-II non-Masing behavior of 304L SS have been investigated using various characterization techniques (EBSD & TEM). Further, the qualitative correlation between the material's internal state variables such as dislocations, dislocation tangles, stacking faults, deformation twins, dislocation cells, martensite content, etc., and the Masing/non-Masing behavior has been established with the help of the strain hardening rate behavior and the proportional stress limit. The dominant role of the deformation-induced martensitic transformation in the non-Masing behavior of 304L SS has been discovered.

Chapter – 5 Numerical Simulation

The influence of martensite fraction on the cyclic plastic deformation and, subsequently, the Masing/non-Masing of materials has been investigated and analyzed. The localization and level of equivalent plastic strain and effective stress increase with the increase in martensite content in 304L SS under fatigue. The higher plastic strain localization would promote more martensitic transformation and, thereby, changes in the material's strain hardening rate behavior and mechanical properties, leading to non-Masing behavior.

Chapter – 6 Conclusions and Scope of Future Work

In this chapter, a brief summary and major conclusions have been provided. Finally, the potential researcher problems that need to be resolved in the future are pointed out.

***Note**

The thesis has been written based on the articles published (or under review) in different journals. All the results, discussions, and conclusions published in those articles were part of the thesis work. Each chapter of the thesis contains the results of a particular article; however, some modifications were made to get continuity in the story and avoid repetitions. Each chapter represents a part of the whole story and could be read independently.

Sanjeev Singh Yadav

Email: 2018mez0004@iitrpr.ac.in

Date:

Place: Rupnagar, Punjab, India

Chapter – 1

1. Literature Survey

This chapter includes the content of our invited review article [4] published in the *Fatigue & Fracture of Engineering Materials & Structures* (volume: 46, issue: 3 and pages: 759-783). The details of the article are given below. Some additional contents are also included, which could not be presented in the review article.

A Comprehensive Review and Analysis of Masing/Non-Masing Behavior of Materials under Fatigue

Sanjeev Singh Yadav^{*a}, Samir Chandra Roy^{*a} and Sunil Goyal^b

^aMaterial Behavior Research Laboratory, Department of Mechanical Engineering, Indian Institute of Technology Ropar, Rupnagar, Punjab 140001, India

^bNuclear Fuel Complex, Kota Project, Rawatbhata, Rajasthan 323303, India

*Corresponding authors' email ids: 2018mez0004@iitrpr.ac.in (S. S. Yadav), scroy@iitrpr.ac.in (S. C. Roy)

Corresponding authors' address: Material Behavior Research Laboratory, Department of Mechanical Engineering, Indian Institute of Technology Ropar, Rupnagar, Punjab 140001, India

Abstract

Over the last 50 years, many researchers have contributed significantly towards understanding the Masing/non-Masing behavior of materials. However, there has been no review article or scientific report published to date that highlights the progress made in this domain. This article presents a state-of-the-art comprehensive review and analysis of the Masing/non-Masing behavior of materials under low cycle fatigue loading. Understanding of Masing/non-Masing behavior is important for the development of fatigue-resistant materials, prediction of fatigue life, and constitutive models and simulation. The influence of various factors such as stacking fault energy, temperature, strain amplitude, and loading conditions on Masing/non-Masing behavior has been summarized in this article. The literature pertaining to the internal microstructural changes observed in different materials by various researchers has been collected and compiled. The different methods of analyzing Masing/non-Masing behavior reported in the open literature are assessed and presented. The importance/significance of Masing/non-Masing behavior in constitutive modeling and fatigue life prediction has also been highlighted. Finally, conclusions based on the review and the potential problems required to be resolved in the future are also pointed out.

Keywords: low cycle fatigue, non-Masing behavior, assessment methods, plastic strain energy density, constitutive modeling, life prediction

1.1 Introduction

Engineering materials used in structural applications, nuclear power plants, and aerospace industries are subjected to cyclic loading. Hence, cyclic plastic deformation is an inevitable phenomenon that occurs during their service life. The cyclic plastic behavior of materials manifests itself in various ways viz-a-viz cyclic hardening, softening, saturation, secondary hardening, stress relaxation, etc. [10–13], which leave their signature in the stress-strain hysteresis loops that form during fatigue cycling of materials [14]. The hysteresis loops can be classified into two categories depending on their evolution with strain amplitude - (a) Masing and (b) non-Masing [3]. A material is said to exhibit the Masing behavior if the stable cyclic stress-strain hysteresis loops are geometrically similar (**Figure 1.1**), irrespective of strain amplitude [15,16]. The loading (or unloading) branches of the geometrically similar hysteresis loops of different strain amplitudes coincide with one another when plotted with a common tip, as shown in **Figure 1.1**. Alternatively, it can be said that for Masing behavior, the cyclic stress-strain curve, magnified by a factor of two, resembles (geometrically) the loading branches of the hysteresis loops at different strain amplitudes [17], as shown in **Figure 1.2**.

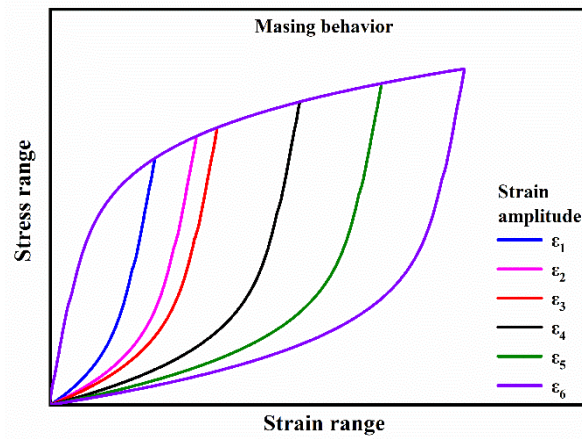


Figure 1.1 Schematic representation of Masing behavior.

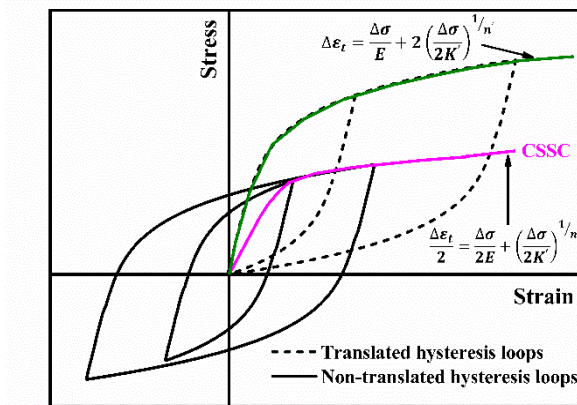


Figure 1.2 Schematic representation of Masing behavior with respect to cyclic stress-strain curve. Only two hysteresis loops are shown in the figure.

In the case of non-Masing behavior, the coincidence may occur only when the stable hysteresis loops of different strain amplitudes are translated along the linear elastic slope to match the loading branches, called the master curve (OAB) [18,19], as shown in **Figure 1.3(a)**. The classification of low cyclic fatigue (LCF) behavior into Masing and non-Masing has been in use for many decades. However, Yadav et al. [7] recently (2021) reported that the non-Masing behavior could further be classified into two categories, **Figure 1.3**. In one category (Type-I), the materials [3,19] were found to exhibit non-Masing behavior while the master curve could be constructed (**Figure 1.3(a)**). In another category (Type-II), a few other materials [6,8,19] were found to exhibit non-Masing behavior, while the master curve could not be constructed (**Figure 1.3(b)**). The latest classification of material behavior under LCF has been summarized in **Figure 1.4**. Although the classification is done based on the loop shape, it should be noted that the non-Masing behavior of Type-I and Type-II could fundamentally represent some characteristic differences in the material behavior.

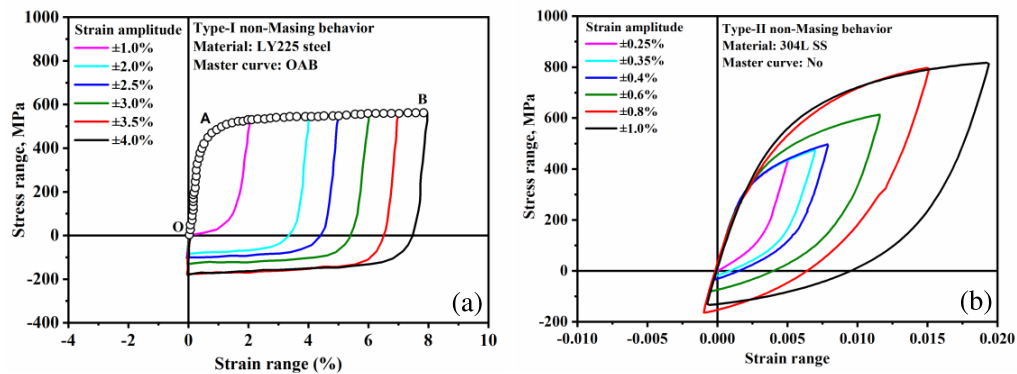


Figure 1.3 Representation of (a) Type-I [19] and (b) Type-II [19] non-Masing behavior of LY225 steel and 304L SS, respectively. First published in [19] [Transactions of the Indian National Academy of Engineering, 7, 411-416, 2022] by Springer Nature.

Numerous studies [16,20] have been conducted to understand the characteristics of Masing/non-Masing behavior; however, no comprehensive literature could be found in the open platform that summarizes all the knowledge and information available. A comprehensive understanding of the Masing/non-Masing behavior is important for various reasons like- (i) development of constitutive laws for simulating such behavior of materials, (ii) design/development of advanced fatigue resistance structures/materials for extreme environmental conditions, and (iii) life prediction. When a material shows non-Masing behavior, the shape of the hysteresis loop changes significantly with the strain amplitude. Thus, the material parameters obtained from the fatigue test data at a particular strain amplitude cannot be used for simulating the material response at other strain amplitudes [21]. Proper

understanding of the factors that contribute to the Masing/non-Masing behavior and changes in the materials' internal structure would help researchers develop a robust constitutive model for simulating the materials' Masing/non-Masing behavior. Khutia et al. [22] made an attempt to develop such a constitutive model for non-Masing behavior by incorporating a stress memory function term in the Ohno-Wang model [23,24]. However, the model could not predict the shape of hysteresis loops accurately.

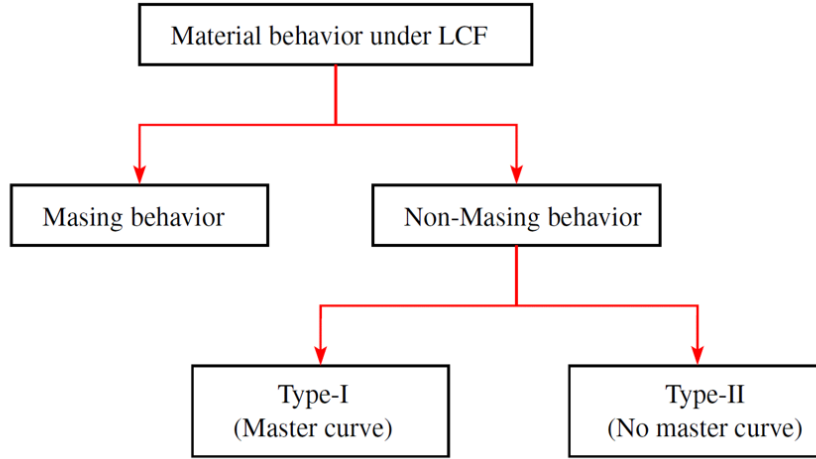


Figure 1.4 Classification of material behavior under low cycle fatigue.

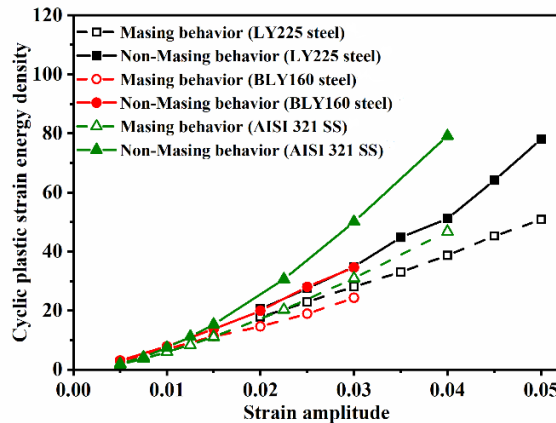


Figure 1.5 Variation of the cyclic plastic strain energy density with strain amplitude for Masing and non-Masing behaviors of three different materials. The plots are generated by extracting the data for LY225 steel [5], BLY160 steel [8], and AISI 321 SS [6]. The data for Masing behavior were obtained by constructing the hysteresis loops for an idealized Masing behavior of the materials, as discussed in the article [7].

Many researchers [16,25] believe that microstructural stability is essential for Masing behavior. The alteration in strain amplitude [16,26], stacking fault energy (SFE) [15], temperature [27,28], and type of loading [29,30] may cause microstructural instability in materials leading to non-Masing behavior. During fatigue, the material absorbs a certain amount of energy represented by the area within the hysteresis loops, called the cyclic plastic strain energy density

(CPSED) [3]. In the literature, many researchers have made efforts to use the estimate of the area within the hysteresis loop of stabilized cycles at different strain amplitudes to describe the Masing/non-Masing behavior [3,7]. For Masing behavior, owing to the microstructural stability, the CPSED varies in a slightly nonlinear manner with strain amplitude (**Figure 1.5**). However, for non-Masing behavior, the material absorbs some extra energy that causes the microstructural instability in terms of phase transformation, dislocations generation, creation of stacking faults and deformation twins, etc., which leads to a strong nonlinear variation of CPSED with strain amplitude [7,31,32], as shown in **Figure 1.5**. Thus, the non-Masing behavior would result in the reduction of fatigue life compared to the Masing behavior.

The fatigue life of a material depends on various parameters such as strain, stress, initial crack size, crack growth rate, etc. One parameter, or a combination of more, can be used as input variables for the estimation of fatigue life. However, the most commonly used methods consider only one input variable (with some material constants) to predict fatigue life [33]. The strain-based method (Coffin-Manson relationship) [34,35], stress-based method (Basquin relationship) [36], and damage tolerant method (Paris law) [37], consider the strain range, stress range, and crack growth rate as input variables, respectively. Although stress and strain can be used independently for life prediction, they are fundamentally linked to each other through material properties (*i.e.*, stiffness). The estimate of CPSED depends on both stress and strain experienced by the material. Thus, the CPSED can be considered a fundamental quantity and is used in various strain energy-based life prediction methods [3,5]. It should be noted that the existing methods based on the CPSED can be used only for Type-I non-Masing behavior, not for Type-II. Yadav et al. [7,19] have proposed a model (will be discussed in **Section 2.3.3**) that takes care of all kinds of behaviors such as Masing, non-Masing (Type-I), and non-Masing (Type-II).

The combined nonlinear isotropic-kinematic hardening model has been used extensively for the simulation of the fatigue behavior of materials or components [21,38]. This model and a few others [39] are available in the commercial finite element analysis codes like ABAQUS, ANSYS, etc., but none of these has the ability to simulate the non-Masing behavior. An actual component or structure with a variable cross-section experiences different levels of stress/strain at different locations under cyclic loading. Thus, the simulation and design of an actual component with complex geometry become difficult as it is difficult to define the material parameters that would be valid for the whole range of stress or strain that the structure would undergo. The development of such a versatile model would significantly improve the design and development of engineering components and structures.

Most of the continuum models are empirical in nature, and thus don't explain the physics involved with the response of materials under cyclic loading. Therefore, researchers [40] have been trying to develop internal variable dependent phenomenological models, which require in-depth knowledge of microstructural changes of materials under cyclic loading. Some researchers [15,16] have contributed significantly to revealing the material microstructural changes that occur while exhibiting non-Masing behavior. The number of articles being published has increased tremendously over the years. However, there has been minimal effort to model non-Masing behavior [21,22]. This chapter aims to compile all the information about the materials' Masing and non-Masing behavior available in the open literature and provide a detailed discussion on the current status of understanding.

1.2 Material behavior under LCF

Depending upon the initial microstructural state, loading condition, strain amplitude, and stacking fault energy, materials may exhibit cyclic hardening, softening, saturation, and secondary hardening behavior under low cycle fatigue [15,16,25]. Cyclic hardening [12] is associated with the dislocation generation and their interaction among themselves, as well as with solute atoms or precipitates, whereas cyclic softening is associated with the annihilation of dislocations or rearrangement of dislocations to cells/sub-grains [11,41]. The secondary hardening occurs if phase transformation takes place during cyclic deformation [42]. Materials' hardening/softening behavior promotes change in microstructural/substructural conditions during deformation. These changes are reflected in the shape and size of the hysteresis loop during cyclic loading. Microstructural stability is an essential requirement for a material to exhibit Masing behavior. However, materials undergo various microstructural changes under certain loading conditions, causing them to exhibit non-Masing behavior.

From the historical point of view, the research on the Masing/non-Masing behavior started with the Bauschinger experiment [1]. In 1886, Bauschinger investigated the tensile and compressive behavior of various steels and observed a reduction in the yield strength in the compression direction, known as the Bauschinger effect [1]. Masing (1923) made an effort to model this reduction in yield strength due to the Bauschinger effect, which is a characteristic response of crystalline material under cyclic loading [2]. Interestingly, while analyzing the results, he discovered that the proportional stress limit of the loading or unloading branches of the hysteresis loops at different strain amplitudes remains constant for Masing behavior, whereas it is not true for non-Masing behavior. Generally, microstructural events such as dislocation generation, resistance to dislocation motion, formation of stacking faults, and twins lead to a change in proportional stress limit ($\delta\sigma_0$) with strain amplitude [18,30]. There has been

very limited progress in this field from 1923 to 1965, and only a very few articles are available in the literature describing the Masing/non-Masing behavior under different conditions [43,44]. In 1966, Halford [45] proposed a relationship to estimate the CPSED based on the analysis of the hysteresis loops. Morrow [46] used that relationship to estimate fatigue damage in different materials. Further, the plot between the cyclic stress amplitude and cyclic plastic strain amplitude was reported to be linear (on log-log plot) for Masing behavior, where the slope of the plot represented the cyclic strain hardening exponent. However, in the case of non-Masing behavior, the shape of the plot was nonlinear or bilinear on a log-log plot [28]. Many researchers investigated hysteresis loops of materials showing non-Masing response [3,7,30]. Jhansale and Topper (1971) [18] proposed a method of master curve formation by translating each loop along the linear elastic portions to coincide with the loading branches of stable hysteresis loops at different strain amplitudes (**Figure 1.3(a)**). In 1984, Ellyin and Kujawski [3] extended the master curve approach [18] and proposed a relationship to calculate the CPSED for the non-Masing (Type-I) behavior of the material. Yadav et al. [7] proposed a new model and further extended the applicability of CPSED to non-Masing (Type-II) behavior. The summary of the historical development of Masing/non-Masing behavior is listed briefly in **Table 1.1**.

Table 1.1 The landmark developments in the field of Masing/non-Masing behavior

Sr. No.	Year/decades	Landmark developments in the field of Masing/non-Masing	Reference
1	1880s	Bauschinger effect was proposed	Bauschinger [1]
2	1920s	Masing tried to model the Bauschinger effect	Masing [2]
3	1950s	The term “Masing behavior” was proposed	Woolley [43]
4	1960s	Estimation of the CPSED for Masing behavior	Halford [45]
5	1960s	Influence of strain amplitude on Masing/non-Masing behavior	Morrow [46]
6	1970s	Proposed the master curve approach for non-Masing behavior	Jhansale and Topper [18]
7	1977	Masing/non-Masing behavior of different materials was analyzed by the Bauschinger strain method	Abdel-Raouf et al. [47]
8	1984	Estimation of the CPSED for non-Masing behavior	Ellyin and Kujawski [3]

9	1984 - present	Use of CPSED for life prediction by various researchers	Ellyin and Kujawski [3] and Shi et al. [5]
10	1988	Influence of loading sequence on Masing/non-Masing behavior	Wang and Laird [48]
10	2001	Influence of stacking fault energy on Masing/non-Masing behavior	Plumtree and Abdel-Raouf [15]
11	2004	Influence of temperature on Masing/non-Masing behavior	Ye et al. [49]
12	2010	Application of the probability density function method to analyze the Masing/non-Masing behavior	Sivaprasad et al. [30]
14	2021	Classification of non-Masing behavior into two categories viz., (i) Type-I and (ii) Type-II non-Masing behavior	Yadav et al. [7]
15	2021	Proposed a universal method (will be discussed in Section 2.3.3) to predict the CPSED and the fatigue life	Yadav et al. [7]

Many researchers [27,30,50] have also investigated microstructural aspects of Masing/non-Masing behavior. Nellessen et al. [51] found an increase in dislocation density with strain amplitude that promotes cell formation in austenitic stainless steel. Such dislocation cell formation is reported to be responsible for the non-Masing behavior of materials [15,52]. Sivaprasad et al. [30] attributed the non-Masing behavior of 304LN SS to the martensite and unstable dislocation substructure. The microstructure of materials under fatigue may consist of soft PSBs regions and hard matrix regions. As reported by Jameel et al., [53] if the volume fractions of persistent slip bands (PSBs) do not change with cycling, the material would exhibit a Masing behavior. However, an increase in the volume fraction of PSBs with cycling would create a condition of microstructural instability leading to non-Masing behavior. Liu et al. [54] observed that the dislocation density increases during austenite to martensite phase transformation due to strain misfit associated with the process, promoting non-Masing behavior. Li et al. [50] noticed a non-uniform dislocation structure in the material, causing the deviation from the Masing behavior. They further tried to quantify the deviation from the Masing behavior in terms of the change in the proportional stress limit ($\delta\sigma_0$).

Many factors, such as stacking fault energy, strain amplitude, temperature, and loading conditions, affect materials' Masing/non-Masing behavior. Understanding the effects of various factors on Masing/non-Masing behavior can significantly improve fatigue life assessment techniques. The various factors and their effects are discussed in detail in the next section.

1.3 Factors affecting the Masing/non-Masing behavior of materials

1.3.1 Influence of the stacking fault energy (SFE)

The deformation mechanism of the face-centered cubic materials mainly depends upon the magnitude of the SFE [55]. For the low SFE ($< 20 \text{ mJ m}^{-2}$), intermediate SFE ($20\text{--}45 \text{ mJ m}^{-2}$), and high SFE ($>45 \text{ mJ m}^{-2}$), the deformation mechanisms are dominated by the phase transformation, twinning, and dislocation glide, respectively [55,56]. The dislocation cross slip is difficult for low SFE materials due to large stacking fault width [57]. In contrast, it is easy for high SFE materials, leading to dislocation cell formation during cyclic deformation (**Figure 1.6**), responsible for the non-Masing behavior [15,52]. Mughrabi [58] observed that multiple slips, low friction stress, and cross slip promote the formation of dislocation cell structure in order to reduce the strain energy of the dislocations by clustering into the cell walls. In aluminum alloy (grade 3003) under LCF, Yaguchi et al. [59] observed that dislocation cell structure initially develops into random cells, followed by the formation of rough cells, and finally, well-defined cell structure with the number of cycles. Moreover, the cell wall thickness decreases due to the dynamic recovery of the dislocation during the deformation. Similar kinds of random (**Figure 1.6(a)**) and well-defined cell structures (**Figure 1.6(b)**) have been reported by Plumtree and Abdel-Raouf [15]. The evolution of microstructure, which depends on SFE, has been investigated under fatigue at room and high temperatures by many other researchers in the literature [60]. For intermediate SFE materials, more twin boundaries act as obstacles to dislocation movement by the dynamic hall patch effect [61], which leads to significant microstructural instability and, consequently, non-Masing behavior and vice versa. In low SFE materials, a large fraction of the transformed phase along with high dislocation density leads to non-Masing behavior [7], whereas the Masing behavior is attributed to the low fraction of the transformed phases, causing minimal microstructural changes [27].

The SFE of materials mainly depends on chemical composition [62,63]. Researchers [64] have investigated the effects of various alloying elements on electronic structure and, consequently, SFE of materials. Some of the alloying elements, such as carbon [65], aluminum [66], and nickel [64], increase the SFE, and other elements, such as silicon and manganese decrease it [63,67]. The SFE of materials also depends on the deformation temperature. It increases with an increase in temperature [68], thereby leading to the suppression of phase

transformation in metastable stainless steel at high temperatures. According to Plumtree and Abdel-Raouf [15], the phase transformation can be responsible for the non-Masing behavior of some materials. The high strain rate of testing may increase the material temperature, which increases the SFE of the materials [42]. The SFE influences the deformation mechanisms or microstructural conditions of the materials during deformation, ultimately leading to Masing/non-Masing behavior. The influence of SFE on materials' Masing/non-Masing behavior is summarized in **Figure 1.7**.

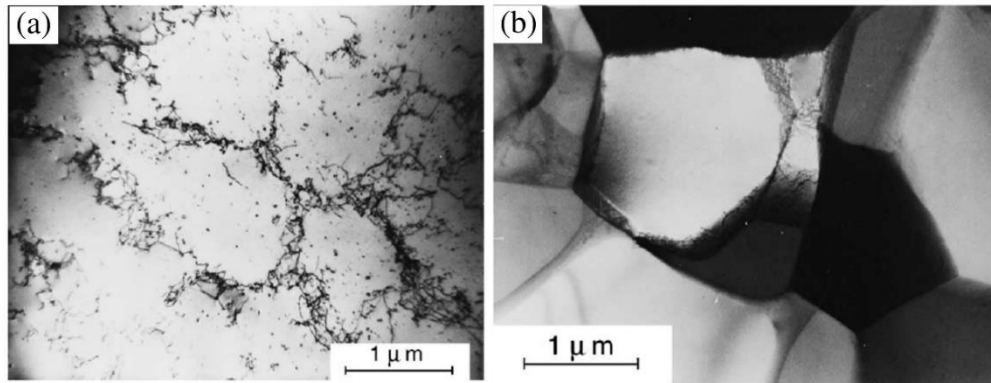


Figure 1.6 Dislocation cell formation in aluminum (high SFE material) for strain amplitude of $\pm 1.0\%$ (a) after the onset of saturation (30 cycles) shows random cell structure [15]; (b) after failure (11,300 cycles) shows well-defined cell structure [15]. Reprinted from Plumtree and Abdel-Raouf [15] and with permission from Elsevier.

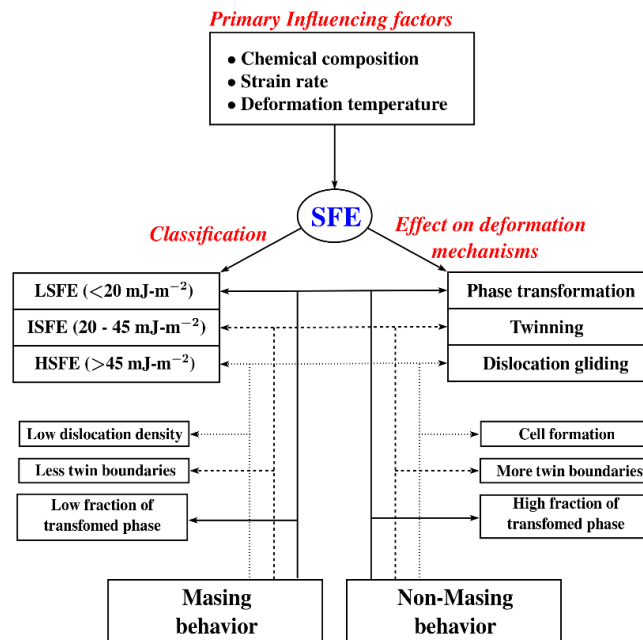


Figure 1.7 Influence of the stacking fault energy on materials' Masing / non-Masing behavior. Note: LSFE = low stacking fault energy, ISFE = intermediate stacking fault energy, HSFE = high stacking fault energy.

1.3.2 Influence of temperature

The influence of temperature on the Masing/non-Masing behavior of materials under different loading conditions has been investigated by many researchers [69,70]. The nickel-based superalloy (GH4145/SQ) under the companion specimen test and the incremental step test at 538°C yields high slip band density at high strain amplitudes, leading to non-Masing behavior [49]. Goyal et al. [28] have investigated the 316LN SS at 600°C; the non-Masing behavior was observed due to dislocation pinning (**Figure 1.8(a)**) resulting from dynamic straining aging (DSA) at lower strain amplitude ($<\pm 0.5\%$). In contrast, the Masing behavior was due to well-developed microstructural conditions, *i.e.*, dislocation cell structure (**Figure 1.8(b)**) at relatively higher strain amplitudes ($>\pm 0.5\%$). In hot-rolled polycrystalline AISI 1025, Watanabe et al. [71] found the Masing behavior due to fully homogeneous dislocation cell structures. It should be noted that dislocation cell structure forms when a material exhibits non-Masing behavior as well [15]. Dynamic strain aging influences the deformation behavior of materials, especially at high temperatures. Depending on the material, DSA occurs in a specific range of temperatures and strain rates [72,73]. From a microstructural point of view, the influence of temperature on deformation behavior has been studied extensively in the literature [70,74]. In 301 SS, Neding et al. [75] have observed that the martensite content and tendency to form stacking faults decrease with an increase in temperature, owing to higher critical stress needed to create the stacking faults and martensite. The variation of the aforementioned microstructural conditions of materials with temperature leads to Masing/non-Masing type of responses under fatigue.

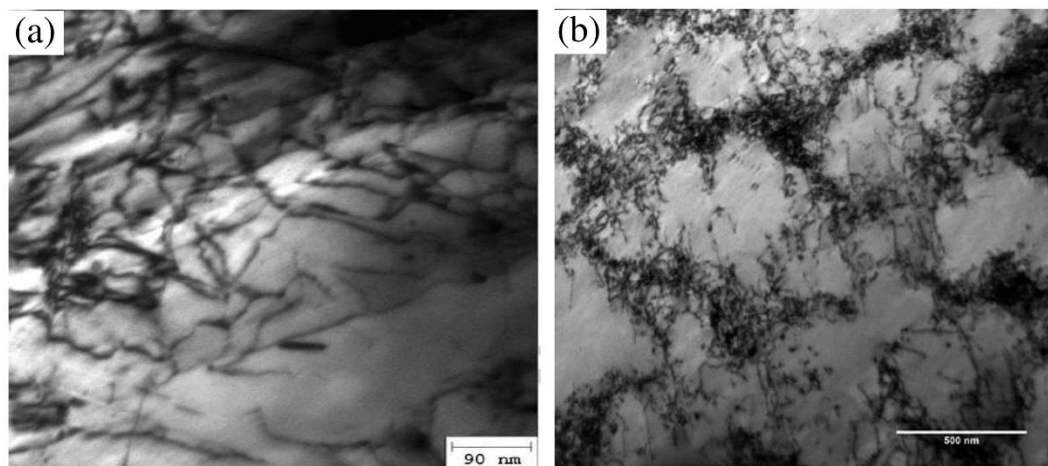


Figure 1.8 Dislocation substructure in 316LN SS during deformation at (a) $\pm 0.4\%$ and (b) $\pm 0.8\%$ strain amplitude at 600°C [28]. Reprinted from Goyal et al. [28] and with permission from Elsevier.

In 304LN SS, Dey et al. [27] observed Masing behavior at -50°C due to stable microstructural conditions, whereas non-Masing behavior at 28°C and 285°C because of the deformation mechanism controlled by the dislocation activities such as high rate of dislocation generation and multiplication of dislocations. For SA333 Gr-6 steel, non-Masing behavior was observed at room temperature and 300°C ; however, deviation from Masing behavior was more at 300°C owing to the generation of more dislocations and interactions leading to microstructural instability [76]. In the modified 9Cr–1Mo steel, Guguloth et al. [77] observed the non-Masing behavior at ambient temperature, whereas partial non-Masing behavior at elevated temperature (600°C) due to coarsening of precipitates and dynamic strain aging effect. Moreover, the same material at 300°C exhibited non-Masing behavior due to equiaxed cell structure and Masing behavior due to elongated cell structure [69].

The ability to cross slip due to activation of secondary slip system [78], DSA [28], high dislocation activities [27], such as high rate of dislocation generation, multiplication, and interactions with dislocations or precipitates, etc., at elevated temperature, cause the microstructural instability, which leads to non-Masing behavior under different temperature ranges for various materials. Inconel 617 alloy exhibited the non-Masing behavior at high temperature (750°C) due to localized deformation with multiple cross slip activation, causing the changes in dislocation configuration [79]. In the case of P92 steel at RT and 650°C , Zhang et al. [80] concluded that the non-Masing behavior is associated with changes in dislocation configuration and cell structure. The non-Masing behavior of G115 steel at high temperature (650°C) is attributed to the phase instability and transient dislocation substructure [70]. The different microstructural factors responsible for Masing/non-Masing behavior are critically reviewed and listed briefly in **Table 1.2**.

Table 1.2 Microstructural factors responsible for Masing/non-Masing behavior of various materials under different conditions

Material	Test conditions	Masing	Non-Masing	Microstructural factors	Reference
316LN SS	LCF (600°C)	---	Yes	Dislocation pinning due to DSA	Goyal et al. [28]
316LN SS	LCF (600°C)	Yes	---	Dislocation cell structure	Goyal et al. [28]
AISI 1025	LCF (RT)	Yes	---	Dislocation cell formation	Watanabe et al. [71]

304L SS	LCF (RT)	---	Yes	Phase transformation	Mughrabi and Christ [16]
304LN SS	LCF (RT)	---	Yes	Phase transformation	Sivaprasad et al. [30]
Nickel superalloy (GH4145/SQ)	LCF (538°C)	---	Yes	High slip band density	Ye et al. [49]
304LN SS	LCF (-50°C)	Yes	---	Microstructural stability	Dey et al. [27]
304LN SS	LCF (285°C)	---	Yes	More dislocation activities	Dey et al. [27]
SA333 Gr-6 steel	LCF (300°C)	---	Yes	Microstructural instability	Kumar et al. [76]
Modified 9Cr-1Mo steel	LCF (600°C)	---	Yes	Coarsening of precipitates and DSA effect	Guguloth et al. [77]
Modified 9Cr-1Mo steel	LCF (300°C)	---	Yes	Equiaxed dislocation cell structure	Verma et al. [69]
P92 steel	LCF (600°C)	---	Yes	Phase transformation and cell formation	Zhang et al. [80]
Martensitic steel (G115)	LCF (650°C)	---	Yes	Phase instability and transient dislocation substructure	Jing et al. [70]
AA6060-T6	LCF (RT)	Yes	---	Dislocation-dislocation interactions	Borrego et al. [81]
AA6082-T6	LCF (RT)	---	Yes	Precipitates-dislocation interactions	Borrego et al. [81]

AA6063 alloy	LCF (RT)	---	Yes	Precipitates- dislocation interactions	Nandy et al. [82]
Multiple phase materials	LCF (RT)	Yes	---	Precipitates- dislocation interactions	Christ and Mughrabi [83]
Sanicro 25 alloy	LCF (700°C)	---	Yes	Non-uniform dislocation microstructure	Li et al. [50]
Maraging steel	LCF (RT)	---	Yes	Formation of dislocation cells	Branco et al. [84]

Plumtree and Abdel-Raouf [15] found that the phase stability depends on strain rate. Pegues et al. [42] observed that the high strain rate ($\sim 0.024 \text{ s}^{-1}$) leads to adiabatic heating, which suppresses the martensite formation during the deformation of 304L SS at room temperature. A similar observation was made by Talonen et al. [85] as well. Based on the extensive literature review, it can be concluded that the adiabatic heating at a high strain rate leads to suppression of phase transformation which ultimately affects the Masing/non-Masing behavior [86,87]. Researchers have also investigated the influence of temperature on phase transformation in various steels under different loading conditions [88]. In 304L SS, the critical plastic strain amplitude for phase transformation is about 0.3% at ambient temperature [16,26,89]. Baudry and Pineau [90] have concluded that the critical value of strain for initiation of the phase transformation increases with temperature in the range of martensite start temperature (M_s) and martensite transformation limiting temperature (M_d). The martensite start temperature (M_s) denotes the temperature above which martensitic transformation would require additional mechanical driving force in terms of the applied stress. Similarly, after the martensite transformation limiting temperature (M_d), the mechanical driving force required for the transformation would be very high.

1.3.3 Influence of strain amplitude

The influence of strain amplitude on the Masing/non-Masing behavior has been investigated for different classes of materials in the literature [91–93]. In 316LN SS, Roy et al. [94] observed Masing behavior at lower strain amplitudes ($< \pm 0.5\%$) and non-Masing behavior at higher strain amplitudes ($> \pm 0.5\%$). Further investigations by Goyal et al. [28] on the 316LN SS revealed the presence of planar slip with dislocation pile-up at a lower strain amplitude

($\pm 0.4\%$), and at high strain amplitude ($\pm 0.8\%$), the tendency towards cell structure formation had been observed by TEM. However, the ferritic-martensitic steel (Mod. 9Cr-1Mo) exhibited non-Masing behavior at lower strain amplitudes ($< \pm 0.375\%$) and Masing behavior at higher strain amplitudes ($> \pm 0.375\%$) [95]. In mod. 9Cr-1Mo steel, the non-Masing behavior at low strain amplitude was attributed to the equiaxed cell structure or ill-defined cell structure, whereas the Masing behavior at higher strain amplitude was associated with well-defined cell structure [95]. In general, Mod. 9Cr-1Mo steel possesses significantly higher dislocation density compared to annealed 316LN SS. The difference in the initial dislocation density attributes to the cyclic softening in Mod. 9Cr-1Mo steel [95], whereas cyclic hardening in 316LN SS [28] under fatigue. A material would exhibit Masing or non-Masing behavior depending on whether the microstructure is stable or not under different amplitudes of cyclic loading. Both the materials, 316LN SS and Mod. 9Cr-1Mo steel exhibited non-Masing behavior due to microstructural instability. However, the instability occurred at low strain amplitudes in Mod. 9Cr-1Mo steel and at higher strain amplitudes in 316LN SS. In austenitic stainless steel, Kundu et al. [96] have found that high dislocation density promoted the formation of vein structures at high strain amplitude leading to heterogeneity within the microstructure responsible for the non-Masing behavior.

Borrego et al. [81] have found that the aluminum alloy (AA6060-T6) exhibited a nearly Masing behavior for all strain amplitudes due to dislocations-dislocation interactions. However, the other aluminum alloy (AA6082-T6) showed non-Masing behavior at higher strain amplitudes due to particle-dislocation interaction. Similarly, Nandy et al. [82] have investigated the aluminum alloy (AA6063-T6) under different aging conditions and found that the dislocation-precipitate interaction led to the non-Masing behavior at high strain amplitude. However, in multiple phase materials, Christ and Mughrabi [83] concluded that dislocation-precipitate interactions played a dominating role compared to dislocation-dislocation interactions, leading to the Masing behavior. The critical strain amplitude up to which the various materials exhibited Masing or non-Masing behavior under different loading conditions is critically reviewed and listed in **Table 1.3**.

Table 1.3 The critical strain amplitude for Masing/non-Masing behavior of various materials under fatigue

Sr. No.	Name of material	Condition	Critical strain amplitude for non-Masing	Critical strain amplitude for Masing	Reference

1	Ferritic pearlite steel	LCF (RT)	$>\pm 0.36\%$	$<\pm 0.36\%$	Abdel-Raouf et al. [47]
2	Al-4 %Cu	LCF (RT)	$>\pm 0.45 \%$	$<\pm 0.45 \%$	Abdel-Raouf et al. [47]
3	Pure copper	LCF (RT)	$>\pm 0.43\%$	$<\pm 0.43\%$	Abdel-Raouf et al. [47]
4	Mod. 9Co-1Mo	LCF (300°C)	$<\pm 0.375\%$	$>\pm 0.375\%$	Verma et al. [69]
5	Austenitic steel (304L SS)	LCF (RT)	$>\pm 0.35\%$	$<\pm 0.35\%$	Mughrabi and Christ [16]
6	Austenitic steel (304LN SS)	LCF (RT)	$>\pm 0.5 \%$	$<\pm 0.5 \%$	Sivaprasad et al. [30]
7	Austenitic steel (316LN SS)	LCF (RT)	$>\pm 0.5\%$	$<\pm 0.5\%$	Roy et al. [94]
8	Austenitic steel (316LN SS)	LCF (RT)	$>\pm 0.5\%$	$<\pm 0.5\%$	Goyal et al. [28]
9	Bridge (Q345qD) steel	LCF (RT)	$>\pm 0.4\%$	$<\pm 0.4\%$	Liao et al. [97]
10	Sanicro 25 alloy	LCF (RT)	$>\pm 0.35\%$	$<\pm 0.35\%$	Li et al. [50]
11	SA333 Gr.6 steel	LCF (RT)	$>\pm 0.7\%$	$<\pm 0.7\%$	Sivaprasad et al. [30]
12	Aluminum alloy 6060 T6	LCF (RT)	$>\pm 1.5\%$	$<\pm 1.5\%$	Borrego et al. [81]
13	Aluminum alloy 6082 T6	LCF (RT)	$>\pm 0.75\%$	$<\pm 0.75\%$	Borrego et al. [81]
14	Inconel 617 alloy	LCF (750°C)	$>\pm 0.25\%$	$<\pm 0.25\%$	Rao et al. [79]
15	Plain C-Mn steel	LCF (RT)	$>\pm 0.5\%$	$<\pm 0.5\%$	Sarkar et al. [32]
16	Pressure vessel steel (20MnMoNi55)	LCF (RT)	$>\pm 0.3\%$	$<\pm 0.3\%$	Sarkar et al. [98]
17	Zircaloy-2	LCF (RT)	$>\pm 0.5\%$	$<\pm 0.5\%$	Rao et al. [93]

Materials undergo various substructural and microstructural changes during cold work (CW) operation. Such microstructural changes within a material can cause non-Masing behavior. Many researchers have investigated the influence of cold work on the Masing/non-Masing behavior of different materials [99]. Raman and Padmanabhan [100] observed Masing behavior for 30% cold worked condition owing to stable microstructural condition; however, deviation from the Masing behavior was observed for 10% and 20% CW during fatigue behavior of 304LN SS at room temperature. Mallick et al. [99] have investigated 304 SS under different degrees of cold work (10%, 20%, 30%, and 40%) and observed that the martensite content increases with the degree of cold work. The formation of martensite may significantly change the microstructural condition of materials due to the misfit strain (volume expansion) associated with phase transformation, thus leading to non-Masing behavior [50]. The extent of martensite transformation in metastable materials during deformation depends on various factors such as the composition of materials [101], grain size [101], strain rate [85], strain amplitude [102], stress state [103], degree of cold work [100], and temperature [104]. Shrinivas et al. [105] found a higher amount of martensite formation during rolling in 304 SS with small grain size, a high degree of cold work, and under a multiaxial stress state. On the other hand, large grain size, low degree of cold work, and uniaxial stress state lead to low martensite formation. Similarly, researchers [99] have also investigated the influence of other factors on martensite transformation responsible for the non-Masing behavior of materials.

1.3.4 Influence of loading conditions

The multiple loading sequence experiments can provide more realistic material behavior than the single-step constant load amplitude test. Therefore, many researchers have investigated the effect of loading sequence on materials' Masing/non-Masing behavior [106,107]. There can be different types of the loading sequences, such as constant step test (**Figure 1.9(a)**), incremental step test (**Figure 1.9(b)**), and decremental step test (**Figure 1.9(c)**). Multiple specimens are used for different strain amplitudes in the case of constant step test (CST), whereas a single specimen is used in incremental step test (IST) and decremental step test (DST). For IST, the specimen is tested at a lower strain amplitude, and upon cyclic saturation, the strain amplitude is increased to the next level. This procedure continues until the required strain amplitude is reached. Similarly, for DST, the test is started at the highest strain amplitude and stepwise decreases to the lowest value.

A material system that exhibits Masing behavior in one load path might exhibit a non-Masing response in another load path or vice versa [83]. Ye et al. [52] observed Masing response for incremental load step whereas non-Masing behavior for companion specimen test

on austenitic stainless steel. The deviation from Masing to non-Masing response was attributed to the high slip band density and cellular-like structure formed during the deformation. Polycrystalline copper exhibited Masing behavior during incremental step loading [83]; however, the monocrystalline copper showed Masing behavior under multi-step loading condition due to stable dislocation substructure [29]. The multi-step loading condition refers to a situation where various loading sequences are combined according to the test requirement.

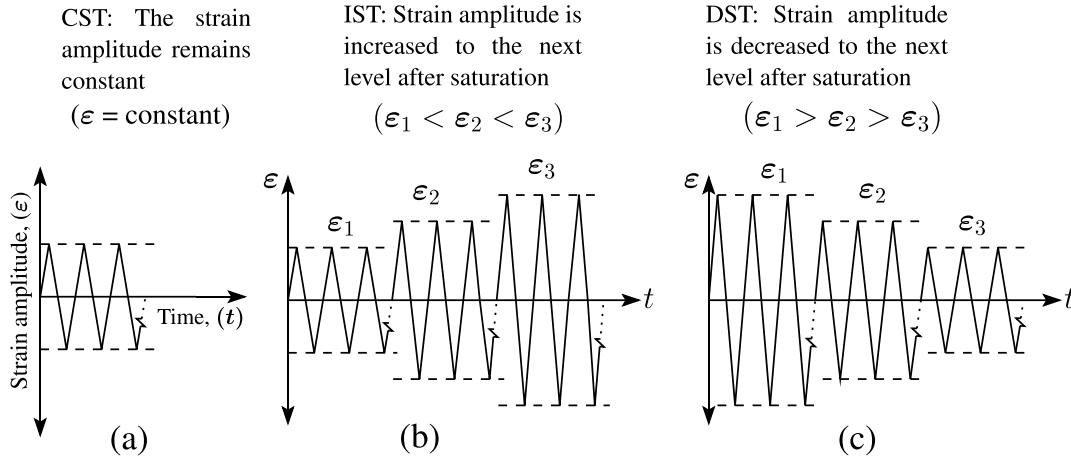


Figure 1.9 Schematic representation of various loading sequences (a) constant step test, (b) increment step test, and (c) decremental step test.

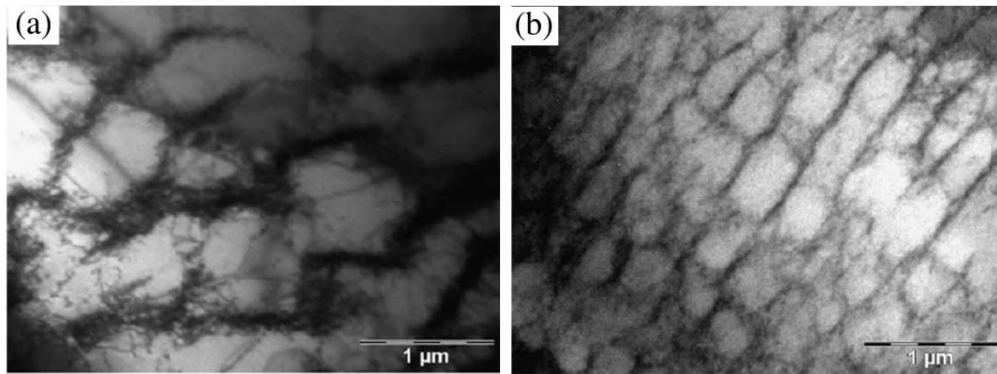


Figure 1.10 TEM pictures show the dislocation cell structure development in 304LN SS at strain amplitudes of (a) $\pm 0.85\%$ and (b) $\pm 1.0\%$ [30]. Reprinted from Sivaprasad et al. [30] and with permission from Elsevier.

Jiang and Kurath [108] studied the deformation behavior of 304 SS by applying a decreasing loading sequence and observed a strong dependency of material response on prior loading strain. Depending on the strain amplitude, the loading sequence might lead to minor or significant changes in the microstructural conditions. Generally, the high localized dislocation density, cell structure formation, dislocation pile-up near grain boundaries, and the presence of various phases in the material describe a heterogeneous microstructure, which causes the non-Masing response. **Figure 1.10** shows the heterogeneous microstructures that consist of

dislocation cells responsible for non-Masing behavior of 304LN SS under fatigue [30]. The dislocation density within dislocation cell walls gradually reduces with an increase in strain amplitude, leading to the transformation of the random cell structure (**Figure 1.10(a)**) to a well-defined cell structure (**Figure 1.10(b)**) at high strain amplitude [30]. It is reported that the microstructural heterogeneities are always dependent on prior loading history in the case of planar slip materials, whereas it is prior history dependent after a certain threshold value of strain amplitude for cross-slip materials [109].

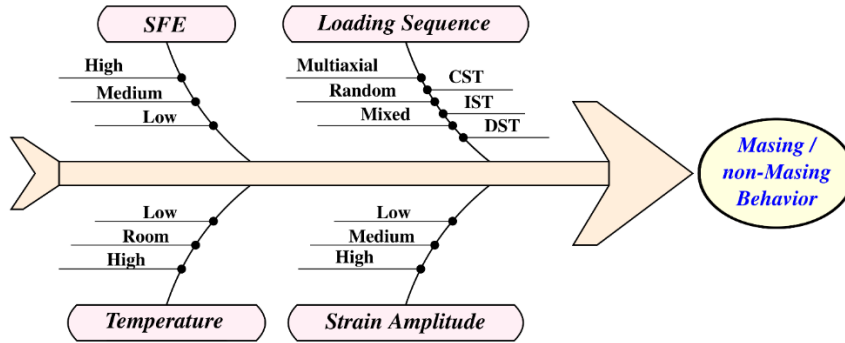


Figure 1.11 Fishbone diagram representing the parameters that affect the Masing/non-Masing behavior. Note: CST = constant step test, IST = incremental step test, DST = decremental step test, SFE = stacking fault energy.

Under the variable amplitude load control test in which the applied load is lower than the previous load, Masing behavior is observed in copper single crystals as the volume fraction of PSBs remains constant during the deformation. However, when the volume fraction of PSBs changes, the non-Masing behavior is observed [53]. In ODS nickel-base superalloy (PM 1000), at high temperature, the non-Masing behavior was observed under the constant amplitude test, whereas the behavior was Masing for the IST, owing to the constancy of dislocation arrangement [110]. Sivaprasad et al. [30] have investigated 304LN SS and SA333 Gr.6 steel under CST, IST, and DST loading at room temperature. They found that both the materials exhibited a non-Masing behavior that is caused by phase transformation in 304LN SS and non-uniform dislocation arrangement in SA333 Gr.6 steel. Further, Arora et al. [111] have observed non-Masing behavior of SA333 Gr.6 steel under multiaxial fatigue loading. There is inadequate knowledge in the literature describing the Masing/non-Masing behavior of various materials under multiaxial, random, and mixed loading conditions. Thus, more research is required in that direction. In summary, there are mainly four parameters that influence the Masing/non-Masing behavior. These are highlighted in **Figure 1.11**.

1.4 Assessment of Masing/non-Masing response

As highlighted earlier, innumerable research has been carried out to understand the internal structural changes a material undergoes during cyclic loading resulting in Masing/non-Masing behavior. The knowledge gained from these investigations would help a material engineer to develop new materials with improved fatigue life by avoiding non-Masing response. The fatigue life is reduced as the materials that exhibit non-Masing behavior absorb extra energy in each cycle. Thus, non-Masing behavior can be considered an undesirable phenomenon that the materials often exhibit under cyclic loading. Although unwanted, the evaluation or quantification of the degree of non-Masing (deviation from Masing behavior) is an important step forward. As of now, four methods viz. (i) Bauschinger strain method [43,47], (ii) Probability density function method [112], (iii) Change in proportional stress limit method [18], and (iv) Cyclic plastic strain energy density method [7] are available in the open literature to analyze the cyclic stress-strain hysteresis loop data for assessing or quantifying the extent of non-Masing response. These methods have been summarized below, along with their limitations while implementing those in practical application.

1.4.1 Bauschinger strain method

The Bauschinger strain (β) is defined as the plastic strain on stress reversal at 75% of maximum tensile stress in the forward direction [15,47]. It is schematically shown in **Figure 1.12**. The 75% of the peak tensile stress is conventionally considered to avoid the effect of creep on the loop shape [43]. Plumtree and Abdel-Raouf [15] considered nine different materials and estimated the β for all the materials subjected to fatigue. The β was found to increase linearly with plastic strain range for materials that exhibited Masing behavior. However, the relationship was nonlinear for materials that exhibited non-Masing behavior. Further, the Masing behavior of 2024-T6 aluminum, AISI 304 SS, Al-4% Cu (0.53 μ m), and 0.18% C steel (30% martensite) was attributed to the presence of finely spaced, strong, non-shearable second phases. Whereas, the non-Masing behavior was attributed to the largely spaced particles in copper, aluminum, Al-4% Cu (1.37 μ m), iron, and 0.18% C (hot rolled) steel. **Figure 1.13** shows the linear and nonlinear variations of the Bauschinger strain with plastic strain range for 2024-T6 aluminum, 1018 steel (30% martensite), A36 steel, and 1018 hot rolled steel for which the data were extracted from the article [47]. Plumtree and Abdel-Raouf [15] have established the relationship (**Equation 1.1**) among the measured β , the plastic strain range ($\Delta\epsilon_p$) and a cyclic strain hardening exponent dependent function $R = (0.875)^{-n'}$.

$$\beta = R \times \Delta\epsilon_p \quad 1.1$$

Over the years, other researchers [77,82] have also used the measure of Bauschinger strain to evaluate materials' Masing/non-Masing behavior. In austenitic stainless steel under IST, Ye et al. [52] observed the linear increase in β with cyclic plastic strain range, indicating the Masing behavior. However, for CST, the non-Masing behavior was associated with a parabolic increase in β with the plastic strain range. Goyal et al. [28] have found the nonlinear relationship between β and plastic strain range for 316LN SS at room and high temperatures. Mukherjee et al. [113] have investigated the effect of aging on Haynes 282 at elevated temperature and found that β does not follow a linear relationship due to non-Masing behavior. Similarly, for modified 9Cr–1Mo steel, Das and Singh [114] observed the nonlinear relationship between β and plastic strain range.

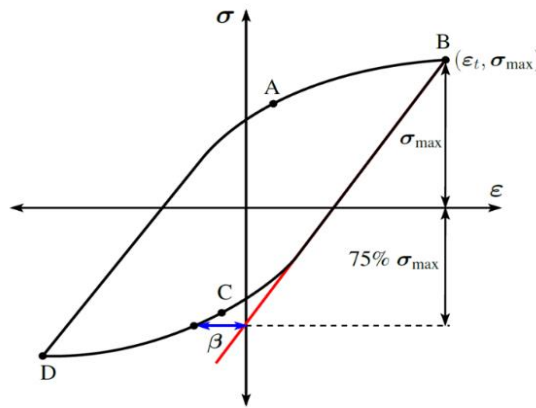


Figure 1.12 Schematic representation of the Bauschinger strain. (Note: σ_{\max} = peak tensile stress, ϵ_t = total strain amplitude, and β = Bauschinger strain).

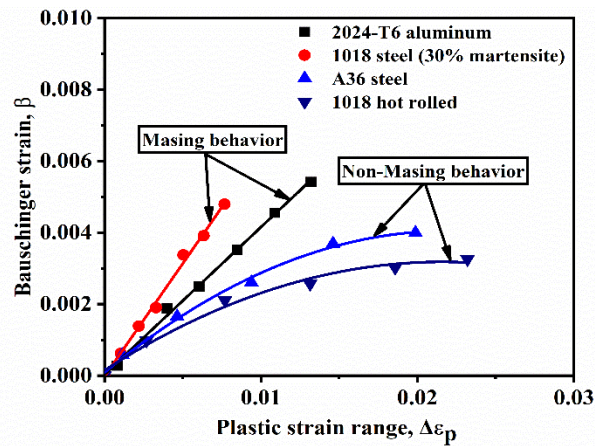


Figure 1.13 Variation of Bauschinger strain with plastic strain range for different materials [47]. The plots are generated by extracting the data for 2024-T6 aluminum, 1018 steel, A36 steel, and 1018 hot rolled steel from the article [47].

Bauschinger strain characterizes the extent of permanent softening due to the annihilation of dislocation in the reverse direction under cyclic loading. It is attributed to the long-range dislocation interactions with different barriers such as solute atoms, dislocations, precipitations,

or grain boundaries during deformation and strain incompatibility in the materials [40,115]. The long-range dislocation interactions increase with strain amplitude due to the inhomogeneous nature of plastic flow resulting in the development of back stresses, which lead to the nonlinear variation of the β with plastic strain range for non-Masing behavior of materials. Li et al. [50] have investigated the non-Masing behavior of Sanicro 25 austenitic alloy and found the nonlinear relationship (**Equation 1.2**) between the Bauschinger strain and the plastic strain amplitude.

$$\varepsilon_p = \left(\frac{\beta}{0.0042} \right)^{3.57} + 0.0011 \quad 1.2$$

The relationship (**Equation 1.2**) proposed by Li et al. [50] gives an estimate of non-zero Bauschinger strain at zero plastic strain. Although it is not fundamentally true, the value we get is very small and hence can be neglected.

1.4.2 Probability density function (PDF)

Masing [2] considered a material made up of 10 elastic-perfectly plastic elements with well-defined boundaries, and the yield stress of these elements increases gradually from element 1 to 10, as shown in **Figure 1.14**. Upon loading, once the load reaches the yield strength of the first element, it starts to deform plastically. However, the other elements continue to deform elastically until the load reaches their yield strengths. When the material's yield strength is mapped, ten discrete yield levels are obtained, representing the Masing behavior of the material. Real materials would have local regions of different hardness and yield strengths due to variations in microstructural variables like dislocation density, phase transformation, and dislocation cells.

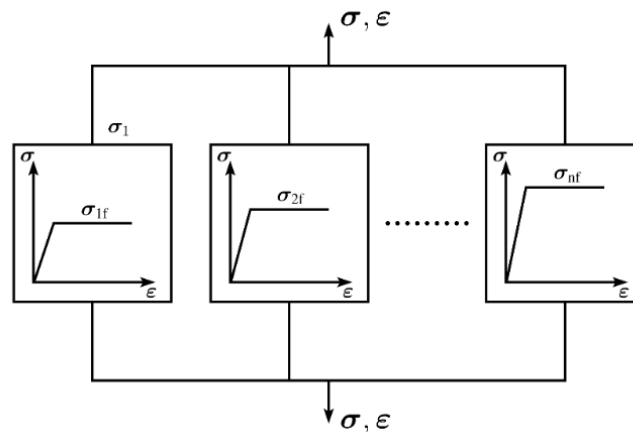


Figure 1.14 Schematic representation of the Masing model (elastic-perfectly plastic elements).

The walls of dislocation cells deform elastically as the edge dislocation cannot pass through the walls, while elastoplastic deformation occurs in the areas between walls. Materials with such

internal heterogeneities can be considered a multi-element model consisting of elastic and elasto-plastic elements with different yield stresses that are strained parallel to the loading direction, similar to Masing's model [116]. However, the local regions will never have definite boundaries, as assumed in the Masing model. Therefore, the yield strength of the material will be a continuous variable rather than discrete, which indicates non-Masing behavior.

It should be noted that the discrete and significantly less variation of the yield stress (or almost constant) with strain amplitude could be observed for materials exhibiting ideal Masing behaviors [117]. The variation of yield stress can be described by the probability density function (PDF) for characterizing the Masing/non-Masing behavior. The PDF is considered to be a mathematical representation of the microstructural evolution that occurs during cyclic deformation [112,116]. The full width at half maximum (FWHM) of PDF will be almost the same (non-variable PDF) at different strain amplitudes for Masing behavior, whereas it changes with strain amplitudes for non-Masing behavior [30] (**Figure 1.15**). Moreover, the PDF peak will be narrow for Masing. It will be wider (broadened peak) for non-Masing behavior due to the introduction of additional yield levels [117]. The main advantage of this approach is that it does not contain any parameter to be fitted, and the PDF can be calculated directly from an experimentally obtained stress-strain hysteresis loop as follows [112,117]:

$$f(\sigma_{yt}) = -\frac{2}{E^2} \left(\frac{d^2 \Delta \sigma}{d \Delta \epsilon^2} \right) \quad 1.3$$

Where E is the modulus of elasticity and the term $\left(\frac{d^2 \Delta \sigma}{d \Delta \epsilon^2} \right)$ is zero for elastic range but maximum at an intermediate part of the loading curve where the maximum number of elements (assuming the material is composed of several elements as in the case of Masing's model) is activated [117]. The multiplication of the second derivative of the loading or unloading branch of the hysteresis loop at a particular strain amplitude and the constant value of $-2/E^2$ represents the PDF. The second derivative of the hysteresis loop can be estimated by MATLAB, python code, etc.

Polák and Klesnil [112] analyzed the cyclic loading using PDF, which was proposed by Afanasjev [118], and concluded that the shape of PDF depends on the microstructural changes such as dislocation substructure, phase transformation, etc., that materials undergo during deformation [119]. Further, it was found that the continuous variation of the PDF is associated with the non-Masing behavior of the material [50,117]. Skelton et al. [120] also found a similar correlation between the non-Masing behavior and PDF. Sivaprasad et al. [30] analyzed the Masing/non-Masing behavior of 304LN SS using the PDF method. They found the phase transformation and non-uniform dislocation arrangement smear out the sharp peaks of PDF,

indicating the introduction of additional yield levels, which lead to shifted and broadened PDF peaks, exhibiting the non-Masing behavior of 304LN SS, as shown in **Figure 1.15**.

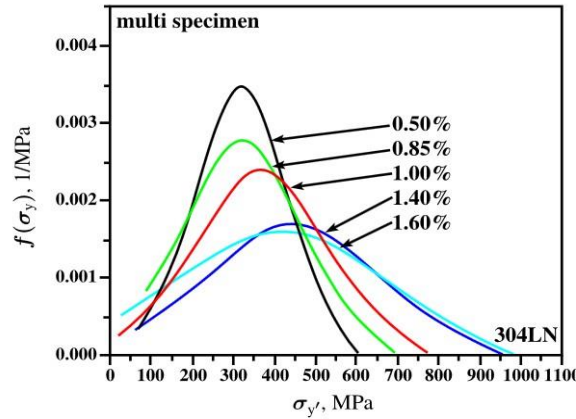


Figure 1.15 Probability density distribution for 304LN SS steel showing non-Masing behavior [30]. Reprinted from Sivaprasad et al. [30] and with permission from Elsevier.

1.4.3 Change in proportional stress limit ($\delta\sigma_0$)

This method is widely used for analyzing the non-Masing behavior observed in materials. This method uses the estimate of the change in the compressive or tensile yield strength of a material under fatigue loading, mainly during the stabilization period, where the nonlinear part of the hysteresis loops remains almost same [47]. The estimation is carried out by measuring the change in proportional stress limit ($\delta\sigma_0$) of the hysteresis loops at different strain amplitudes. **Figure 1.16** schematically shows the method of $\delta\sigma_0$ measurement, achieved by translating the hysteresis loops to match the upper loading branches, *i.e.*, by constructing the master curve (ABC). The change in proportional stress limit ($\delta\sigma_0$) can be analytically [3] defined by using **Equation 1.4**

$$\delta\sigma_0 = \Delta\sigma - 2K' \left(\frac{\Delta\varepsilon_p'}{2} \right)^{n'} \quad 1.4$$

Where, $\Delta\sigma$ represents the stress range of the hysteresis loop, $\Delta\varepsilon_p'$ represents the plastic strain range of the hysteresis loop on the master curve, and K' and n' are the strain hardening coefficient and exponent, respectively, of the master curve. Care should be taken while implementing **Equation 1.4** [3], especially for materials that show a sudden drop in stiffness, which can be visible in the hysteresis loop shape during the transition from elastic to the plastic domain. In those cases, the power-law equation may not be useful for defining the master curve. The value of $\delta\sigma_0$ becomes zero for Masing behavior, and it increases with strain amplitude for non-Masing behavior [121]. Thus, $\delta\sigma_0$ gives an estimate of the degree of non-Masing. The estimate of $\delta\sigma_0$ have been used by many researchers [3,17,27] to estimate the extra energy

absorbed by a material due to non-Masing behavior under fatigue. Many researchers have further used such estimates of plastic strain energy for fatigue life predictions [3,97]. To assess and quantify the Masing/non-Masing behavior, we have extracted the data (hysteresis loops at half-life) for seven different materials viz, 304LN SS [30], 316LN SS [94], SA333 Gr.6 [30], AA6063 [82], AISI 1018 HR steel [15], annealed Cu [122], and annealed Al [122].

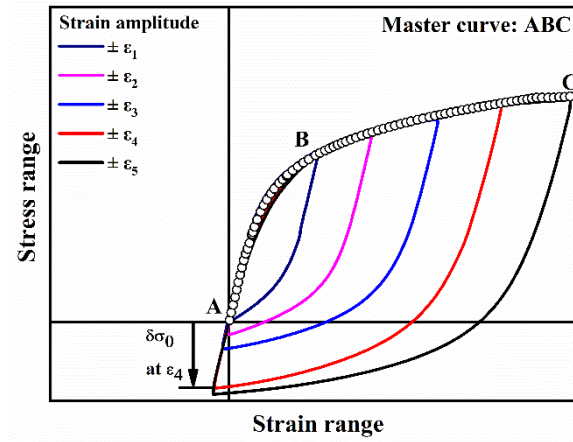


Figure 1.16 Schematic representation of the change in the proportional stress limit ($\delta\sigma_0$) with strain amplitude.

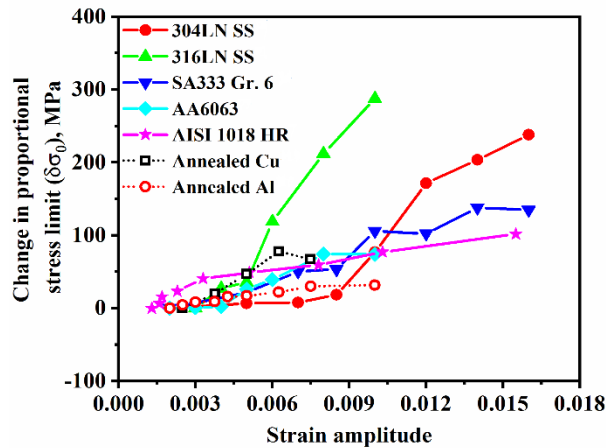


Figure 1.17 Variation of change in proportional stress limit ($\delta\sigma_0$) with strain amplitude for different materials.

The values of $\delta\sigma_0$ have been estimated for all the materials by constructing the master curves. It has been found that the deviation from Masing for annealed Al is less compared to the other materials, and the deviation is highest for 316LN, as shown in **Figure 1.17**. In the literature [15,27,30], many researchers have correlated the $\delta\sigma_0$ with the microstructural variables. Plumtree and Abdel-Raouf [15] have observed that the $\delta\sigma_0$ is related to dislocation density and cell size. Dey et al. [27] have observed temperature-dependent steep variation of $\delta\sigma_0$ with strain amplitude associated with dislocation motion and their interactions that cause the non-Masing

behavior in 304LN SS. Li et al. [50] have also observed an increasing $\delta\sigma_0$ due to the non-uniform dislocation structure in Sanicro 25 austenitic alloy.

Although the change in the proportional stress limit method has been used extensively in the literature [30,31,50], it has a drawback. It can only be used for the materials where construction of the master curve is possible [3]. However, there are materials [6,8,19] for which the construction of the master curve is not possible (**Figure 1.3(b)**). For such cases, Yadav et al. [7,19] have proposed a method based on a non-dimensional parameter known as normalized CPSED difference.

1.4.4 CPSED Method

This method is proposed by us in the article [7] and discussed in detail in **Chapter 2**. This method is based on a non-dimensional parameter known as normalized cyclic plastic strain energy density (CPSED) difference. The method has been validated with 13 different types of materials, including the Masing, Type-I, and Type-II non-Masing behavior (**Chapter 2** and **Chapter 3**). The proposed method can quantify the non-Masing behavior of materials without constructing a master curve. For Masing behavior, ‘normalized CPSED difference’ ≈ 0 , whereas, ‘normalized CPSED difference’ $\neq 0$ for non-Masing behavior (irrespective of Type-I and Type-II). This method is the most versatile, as it can be used for both Masing and non-Masing behavior (Type-I and Type-II).

1.5 Constitutive modeling

Finite element (FE) simulation has extensively been used in many industries (e.g., nuclear, aerospace, and automobile) for analysis of the components' behavior under realistic loading conditions [38]. Numerous constitutive models are available in the open literature for characterizing materials' fatigue behavior [123]. However, the models that are popularly known as Armstrong and Frederick [124], Chaboche [125], modified Chaboche [126], Ohno–Wang [23], modified Ohno–Wang [127], and Abdel Karim–Ohno [128] have gained significant popularity. Chellapandi et al. [123] have used the Chaboche model to design the Indian fast breeder reactor components operating at relatively high temperatures. Similarly, Hassan and Rahman [38] have investigated the elbow component's LCF and ratcheting behavior using the Chaboche model. The combined nonlinear isotropic-kinematic hardening Chaboche model has been the most widely used one for simulating the low cycle fatigue behavior of materials [38]. It is implemented in most of the commercially available software, e.g., ABAQUS and ANSYS. The model can be briefly described by **Equations 1.5 - 1.7** [125], where f , σ' , α' , $r(p)$, σ_y , ε_p , and p represent the yield function, deviatoric stress tensor, back stress tensor, isotropic

hardening function, yield stress, plastic strain tensor, and accumulated plastic strain, respectively. The parameters C and γ are related to the kinematic hardening, and Q and b are isotropic hardening parameters [125].

$$f = \sqrt{\frac{3}{2}(\boldsymbol{\sigma}' - \boldsymbol{\alpha}'):(\boldsymbol{\sigma}' - \boldsymbol{\alpha}') - r(p) - \sigma_y} \quad 1.5$$

$$r(p) = Q(1 - e^{-bp}) \quad 1.6$$

$$\boldsymbol{\alpha}' = \sum_{n=1}^{n=3} \frac{C_n}{\gamma_n} (1 - e^{-\gamma_n \varepsilon_p}) \quad 1.7$$

The material parameters C , γ , Q , and b are determined by performing an LCF test at a particular strain amplitude. Fatigue tests were performed on 304L SS at room temperature for strain amplitudes of $\pm 0.4\%$, $\pm 0.6\%$, $\pm 0.8\%$, and $\pm 1.0\%$ [7]. The material parameters ($C = 83634.08$ MPa, $\gamma = 768.68$, $Q = 63.02$ MPa, and $b = 14.35$) have been determined from the LCF data at $\pm 0.8\%$ strain amplitude. The detail of the material parameter determination can be found in the article [129,130]. Using the material parameters of $\pm 0.8\%$, the LCF simulations were performed for all strain amplitudes. The FE analysis was carried out using ABAQUS software with a 3D cubic model of C3D8R elements. The loading was applied on one face of the cube, and the opposite face was constrained for rotation and translation along the loading direction. The static implicit simulation was done using a triangular waveform similar to the strain-controlled fatigue test. The simulated hysteresis loops at different strain amplitudes for the first cycle (**Figure 1.18(a)**), 10th cycle (**Figure 1.18(b)**), and at the end of the initial cyclic hardening period (20th cycle, **Figure 1.18(c)**) have been plotted.

As can be seen (**Figure 1.18**), the Chaboche model inherently considers material behavior to be Masing. This model, and the others [22,39], cannot be used for materials that show non-Masing behavior, as the material parameters, in such a case, will vary with strain amplitude. Despite this fact, these models have been extensively used for the simulation of the LCF behavior of materials and structures [123,129]. The application of these models for the simulation of actual structures with complex geometries has never been free from shortfalls or errors. This is because the material parameters used in the simulation are generally determined from the fatigue test data of a particular strain amplitude only. However, the mechanical components in actual service conditions experience different levels of strain or stress at various locations. The range of variation in stress or strain level can be continuous or discrete with an infinitely large number of steps. Thus, there is a need to develop a constitute model that can take into account the variation of material parameters with strain amplitude, whereby the non-Masing behavior will also be taken into account.

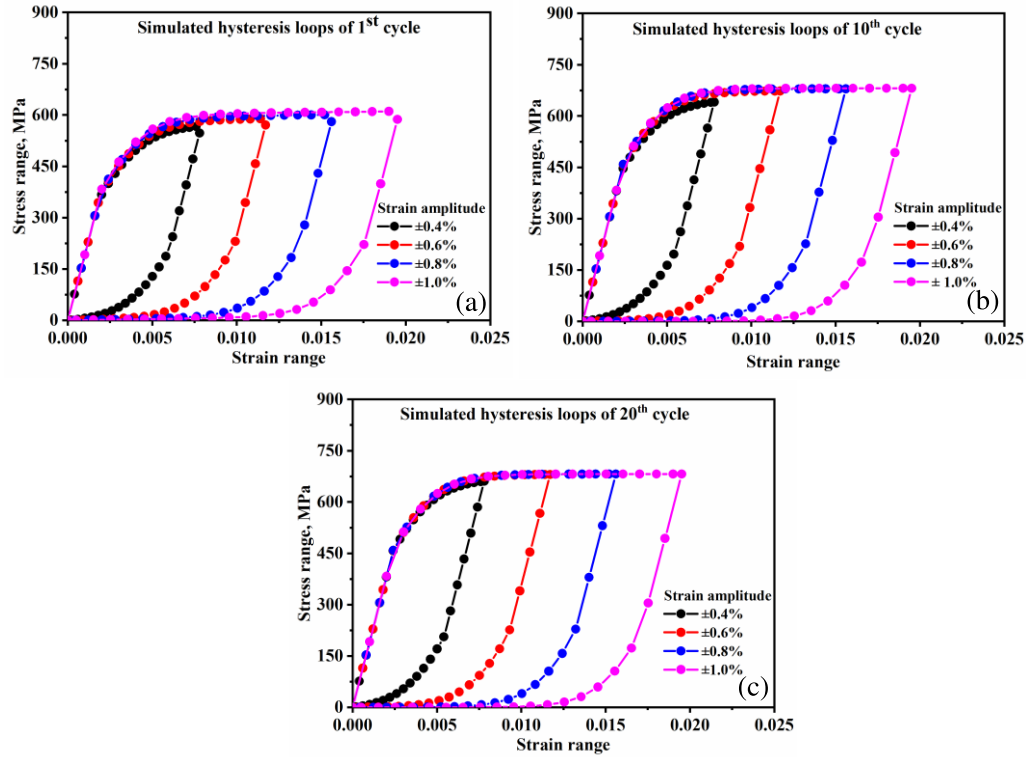


Figure 1.18 Simulated hysteresis loops of (a) 1st cycle, (b) 10th cycle, and (c) 20th cycle of initial cyclic hardening period at different strain amplitudes.

The constitutive models available in the literature are mostly either empirical or phenomenological. Numerous efforts have been made by various researchers for the constitutive modeling of cyclic plasticity. However, efforts towards constitutive modeling of non-Masing behavior are very scanty. Xu et al. [8] have pointed out the effect of hysteresis loop's shape change due to non-Masing behavior and tried to take it into account by modifying the kinematic/isotropic hardening equations. Zhou et al. [131] simulated the strain range memory effect by modifying the kinematic hardening parameters and predicted the hysteresis loop for relatively higher strain amplitude ($>\pm 0.3\%$). However, the deviation was observed for low strain amplitude ($\pm 0.3\%$). Xu et al. [8] have proposed a model based on the internal variables to characterize the cyclic hardening/softening behavior and predicted the hysteresis loop within 10 percent errors under different loading conditions. Kang et al. [132] also attempted to simulate the strain range-dependent cyclic hardening by extending the kinematic hardening model based on the critical state of dynamic recovery without considering the non-Masing behavior of materials. Khutia et al. [22] have made an attempt by incorporating a stress memory function term in the Ohno-Wang model [23] to simulate the non-Masing behavior. However, the model could not accurately reproduce the shape of hysteresis loop for different strain amplitudes.

As mentioned earlier, the microstructural variables such as phase transformation, dislocation cell formation, dislocation-dislocation interactions, dislocation-precipitate interactions, etc., can be the responsible factors for non-Masing behavior depending on temperature, strain amplitude, SFE, and loading conditions [27,40,133]. Therefore, it is essential to establish quantitative correlations between the factors mentioned above and the degree of non-Masing of materials. Such studies would help in proposing a robust microstructural-based constitutive model that may predict the non-Masing behavior under different conditions.

1.6 Fatigue life prediction of non-Masing behavior

Nuclear, aviation, and petro-chemical industries are typical examples where rigorous fatigue analysis is done for life prediction of components or structures [134]. The stress-life (S-N), strain-life (ϵ -N), Paris law, and plastic strain energy-based methods are very popular and commonly used for life prediction [33]. The Coffin-Manson relation, Basquin relation, and Paris law are empirical in nature; the accuracy of these methods depends on the fitting constants [135,136]. These methods do not take into account the variation of the hysteresis loop shape that occurs due to the non-Masing behavior of materials [122,137]. These methods are based on the assumption that the behavior of materials stabilizes (or saturates) at the initial stage of cycling, and the damage accumulated per cycle remains almost constant throughout the entire life [138]. The strain energy density-based methods, on the other hand, can inherently take into account the change in the loop shape. Therefore, these methods are used to predict the fatigue life of materials exhibiting non-Masing behavior. It should be noted that not all strain energy-based methods pay attention to the Masing/non-Masing behavior. Halford [45] had proposed a relationship to calculate the CPSED of Masing behavior as follows:

$$E_m = \frac{1-n}{1+n} \Delta\sigma\Delta\epsilon_p \quad 1.8$$

Where $\Delta\sigma$, $\Delta\epsilon_p$ and n are stress range, plastic strain range, and cyclic strain hardening exponent, respectively. The $\Delta\sigma$ and $\Delta\epsilon_p$ are obtained by merging the compressive tips of the hysteresis loops to get a common loading curve irrespective of strain amplitude.

Many researchers carried out the investigation of hysteresis loops of different materials showing non-Masing responses [3,7]. Jhansale and Topper (1971) [18] proposed the method of master curve construction by translating the hysteresis loops (**Figure 1.3(a)**). Ellyin and Kujawski [3] extended the master curve approach [18] and proposed a relationship [3] to calculate the CPSED for non-Masing (Type-I) behavior of the material as follows:

$$E_{nm(I)} = \frac{(1 - n')}{(1 + n')} (\Delta\sigma - \delta\sigma_0) \Delta\varepsilon_p + \delta\sigma_0 \Delta\varepsilon_p \quad 1.9$$

Where n' is the strain hardening exponent of the master curve, and $\delta\sigma_0$ is the change in proportional stress limit of stable hysteresis loops at half-life [139]. The change in loop shape or the non-Masing behavior is taken into account by measuring the extra energy absorbed by the material compared to its Masing behavior. Conventionally, the measurement of the extra energy is accomplished by measuring the change in the linear-elastic portion of the hysteresis loops with strain amplitude [94,140,141]. It can be understood from **Equation 1.9** [3] that it can be used for the estimation of $E_{nm(I)}$ but not for prediction, as $\delta\sigma_0$ can not be predicted for a given material for any strain amplitude. Researchers [117] have been trying to establish the correlation between the $\delta\sigma_0$ and strain amplitude; however, it could not be achieved. For a design engineer, the prediction of $E_{nm(I)}$ for any strain amplitude would be of prime importance for further prediction of fatigue life.

Equation 1.9 [3] has some drawbacks in estimating the CPSED and, thereby, the fatigue life of materials [5,97]. The main disadvantages are (1) the non-conservative estimation of CPSED and consequently fatigue life [5,97], (2) the necessity of master curve formation [142], and (3) it can be used for estimation only, not for prediction of CPSED [3]. Despite these limitations, this equation has extensively been used to estimate engineering materials' CPSED and fatigue life [5,143–145]. In order to avoid the necessity of master curve formation and be able to predict the CPSED and fatigue life, Yadav et al. [7] have proposed a new model. The proposed model will be discussed in the next chapter.

1.7 Summary and conclusions

This comprehensive review contributes to a better understanding of the inherent complexities involved in the analysis of the Masing/non-Masing behavior. Substantial research activities that were conducted in this field are highlighted and discussed. In this article, the factors that affect the Masing/non-Masing behavior, the assessment methods, and modeling aspects of non-Masing behavior are also discussed in detail. The significance of Masing/non-Masing behavior with regards to the design/development of fatigue-resistant materials for high temperatures and extreme environmental conditions, prediction of fatigue life, and the development of constitutive model have been discussed. **Figure 1.19** summarizes the importance of understanding the Masing/non-Masing analysis highlighting the internal material variables, external factors, and the assessment methods among which phenomenological

correlations are required to be developed. The following observations could be made based on the existing articles available in the open literature.

1. Bauschinger strain method, probability density function method, change in proportional stress limit method, and cyclic plastic strain energy density method are the most popular methods applicable to assess/evaluate the degree of non-Masing behavior. The first two give qualitative information, whereas the last two methods provide a quantitative estimation of the degree of non-Masing behavior.
2. The change in the proportional stress limit method has been used by various researchers for the analytical calculation of CPSED. Such analytical calculation has also been used for the estimation of fatigue life. However, the new CPSED method can be used for the prediction of CPSED and fatigue life. This method is very versatile as it can be used for all behaviors, such as Masing, non-Masing (Type-I), and non-Masing (Type-II).
3. The strain amplitude, temperature, stacking fault energy, and loading sequence are the important factors that influence materials' Masing/non-Masing behavior under fatigue owing to their influence on the microstructure in materials.

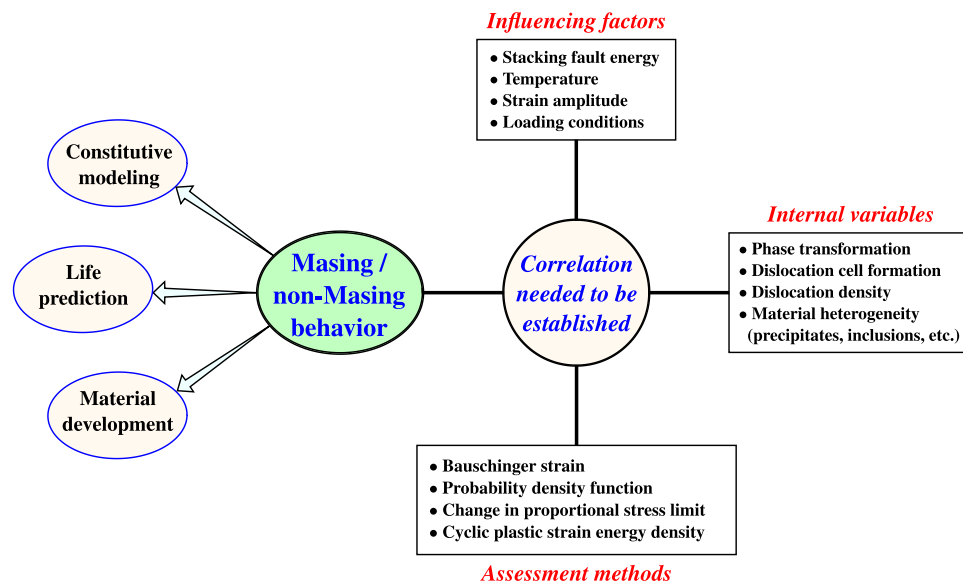


Figure 1.19 Highlights of different components associated with Masing/non-Masing behavior.

4. Low dislocation density and veins structures may lead to Masing behavior, whereas high dislocation density, phase transformation, dislocation cell formation, and material heterogeneity (presence of precipitates, inclusions, etc.) may lead to non-Masing behavior of materials under fatigue. Dislocation cell formation usually causes non-Masing behavior; however, occasionally, Masing behavior can also be observed.

5. Non-Masing behavior is undesirable as it reduces the fatigue resistance of a material. Proper understanding of the external factors and internal material changes would contribute to the development of new materials.

1.8 Research scope and objectives

In the last 50 years, numerous articles have been published in the field of fatigue, analyzing materials' Masing/non-Masing behavior. However, no dedicated thesis or article is found in the literature that comprehensively discusses the Masing/non-Masing behavior and summarizes the findings of various researchers. These facts motivate us to carry out a comprehensive investigation of the Masing/non-Masing behavior of material under strain-controlled fatigue. A comprehensive understanding of the Masing/non-Masing behavior is important for various reasons, like - as (i) the development of constitutive laws for the non-Masing behavior of materials, (ii) the design/development of advanced fatigue resistance structures/materials, and (iii) life prediction. Generally, a material may exhibit Masing or non-Masing behavior under actual loading conditions, and the behavior is influenced by various external factors (as mentioned in **Section 1.3**). The non-Masing behavior has been well known for many decades, but the degree of non-Masing is not well defined in the literature. The methods available for the estimation of CPSED and fatigue life prediction for non-Masing behavior of materials have been discussed in **Section 1.6**. The drawbacks or limitations of these methods have been discussed in detail. The literature review on Masing/non-Masing behavior indicates that no method is available to predict the cyclic plastic strain energy density (CPSED) of material under fatigue. The existing method (based on the master curve approach) can only estimate the CPSED. Moreover, strain energy-based life prediction methods have been gaining popularity over the years. Therefore, we propose using the estimate of CPSED to predict fatigue life. Thus, the prediction of CPSED is essential. Moreover, systematic and dedicated microstructural investigations of non-Masing are not available in the literature. Based on these research gaps, we have formulated the four objectives for this work. These are-

1. The first objective is to summarize the research findings of various researchers worldwide accomplished in the last 50 years. Thus, the focus is to make a comprehensive report on the Masing/non-Masing behavior of materials under fatigue. This state-of-the-art report will act as a single-point source for all information related to Masing/non-Masing behavior of materials.
 2. To develop a model for predicting the cyclic plastic strain energy density (CPSED) and fatigue life of non-Masing behavior materials without needing master curve formation.
-

The objective is also to provide a quantitative estimate of the degree of non-Masing behavior.

3. To investigate the underlying mechanism of non-Masing behavior (Type-I and Type-II) using various characterization techniques such as EBSD and TEM.
4. To investigate the effect of the martensite on the cyclic plastic deformation and non-Masing behavior of 304L SS by numerical simulation.

This investigation/study will contribute toward an in-depth understanding (Mechanistic and microstructural) of the Masing/non-Masing behavior of 304L SS. The knowledge gained from the present analysis would help a material engineer (or metallurgist) to select (or make) a better material to avoid non-Masing response under different loading conditions to achieve a higher fatigue life. The proposed model (discussed in **Chapter 2**) can be used to estimate the fatigue life of the different classes of materials under LCF. Moreover, the qualitative correlation (discussed in **Chapter 4**) between the non-Masing behavior and material internal state variables contributes toward developing the microstructural-based phenomenological model to predict the non-Masing behavior of materials under LCF.

1.9 Some highlights and remarks

Some highlights of the chapter:

- The various factors (like - strain amplitude, temperature, stacking fault energy, and loading sequence) that affect the Masing/non-Masing behavior have been discussed.
- The Masing/non-Masing assessment methods (like - Bauschinger strain, probability density function, and change in proportional stress limit) have also been discussed.
- The constitutive modeling aspect of the non-Masing behavior under low cycle fatigue loading conditions has also been presented and discussed.
- The problem associated with the existing methods for fatigue life prediction of the non-Masing behavior has been discussed and highlighted.
- A new model has been proposed to address the problem associated with the existing methods of the prediction of the CPSED and fatigue life of the non-Masing behavior of the materials under LCF. The proposed model will be discussed in the next chapter.

Remarks:

In this chapter (**Chapter-1**), a comprehensive literature review has been discussed to understand the Masing/non-Masing behavior, and some research gaps associated with it have been identified. Based on these research gaps, the four objectives have been formulated for this

investigation and analysis. The subsequent chapters deal with one of the objectives. The summary and conclusions have been mentioned separately in the end of each chapter.



Chapter – 2

2. Mechanistic Analysis

This chapter includes the results of a journal article [7] published in the Journal of Materials Engineering and Performance (volume: 30, issue: 3 and pages: 2102-2112). The details of the article are given below. Some additional contents are also included, which could not be presented in the article.

Quantitative assessment and analysis of non-Masing behavior of materials under fatigue

Sanjeev Singh Yadav^a, Samir Chandra Roy^{*a}, J. Veerababu^b and Sunil Goyal^c

^aDepartment of Mechanical Engineering, Indian Institute of Technology Ropar - 140001, India

^bMaterials Development and Technology Division, Indira Gandhi Centre for Atomic Research, Kalpakkam-603102, India

^cNuclear Fuel Complex, Kota Project, Rawatbhata- 323303, India

^{*}Corresponding Author, Email: scroy@iitrpr.ac.in (S. C. Roy)

Corresponding Author's Address: Department of Mechanical Engineering, Indian Institute of Technology Ropar, Rupnagar, Punjab-140001, India.

Abstract

Quantitative assessment of non-Masing behavior is studied and a new method is proposed for the estimation of cyclic plastic strain energy density and fatigue life. Low cycle fatigue tests were performed on 304L stainless steel employing strain amplitudes ranging from $\pm 0.25\%$ to $\pm 1.0\%$ at a strain rate of $1 \times 10^{-3} \text{ s}^{-1}$. The material exhibited Masing behavior at lower strain amplitudes and non-Masing behavior at higher strain amplitudes. Secondary hardening was observed at relatively higher strain amplitudes. Both the secondary hardening and non-Masing response were found to be associated with the deformation induced martensitic transformation. The master curve approach, which is generally used for the analysis of non-Masing response, could not be used as experimental data could not be represented in the form of master curve. The proposed method of quantification of non-Masing response could estimate the cyclic plastic strain energy density of 304L stainless steel well within a scatter band of 1.2. The fatigue life of 304L stainless steel could also be predicted within a scatter band of 2. The proposed approach could also estimate the cyclic plastic strain energy density and fatigue life of materials of different grades well within scatter factors of 1.2 and 2 respectively.

Keywords: Low cycle fatigue; Masing and non-Masing behavior; Life prediction; Strain energy density approach.

2.1 Introduction

The austenitic stainless steels (like 304L, 304LN, 316LN SS etc.) find their use in many critical applications such as nuclear power plant and satellite launch vehicles [146]. Low cycle fatigue (LCF) is a dominant failure mechanism in these applications due to repeated cyclic loading. Hence, it is an important consideration for the design and life assessment of stainless-steel components. The 304L SS is sensitive to martensitic transformation during deformation at relatively low temperatures. In low stacking fault energy materials, the deformation is greatly associated with the strain-induced martensite formation, as cross slip of dislocation is difficult to occur [56]. The critical plastic strain amplitude of cyclic straining at the initiation of deformation-induced martensite formation under fatigue is about 0.3% at room temperature [16,26] for this steel.

Material like 304L SS may exhibit Masing or non-Masing behavior under LCF cycling depending on the strain amplitude [28], strain rate [42], temperature [87], loading conditions [147], phase stability [16,27], etc. In the case of Masing behavior, loading branches of the hysteresis loops follow the same loading curve irrespective of strain amplitude [16]. The basic assumption in Masing behavior is that the deformation structure remains the same, or in other words, the effective obstacle distribution remains almost constant irrespective of the strain amplitude [15]. The study carried out on SS 316LN [94] showed Masing behavior at lower strain amplitudes ($<\pm 0.5\%$) and non-Masing behavior at higher strain amplitudes ($>\pm 0.5\%$). Polycrystal copper was found to exhibit Masing behavior during incremental step fatigue loading [83]; however, the single-crystal copper showed Masing behavior during fatigue under ramp loading condition [29]. As reported by Borrego et al. [81], the aluminium alloy (AA6060-T6) exhibited a nearly Masing behavior at all strain amplitudes from $\pm 0.42\%$ to $\pm 1.5\%$. However, the other aluminium alloy (AA6082-T6) showed a deviation from the Masing behavior at higher strain amplitudes ($>\pm 0.75\%$). Nandy et al. [82] reported Masing behavior for the aluminium alloy (AA6063) at under-aged (374 K, 8 h) condition and minor-deviation from it was observed at over-aged (523 K, 8 h) condition. The material exhibited complete non-Masing behavior at peak-aged (448 K, 8 h) condition. Thus, it is evident that material may respond differently under different loading and environmental conditions. Hence, understanding of the cyclic response of the material under fatigue loading condition is very important.

Among the various approaches available in open literature for fatigue life prediction, the strain energy based approach is widely used [148]. Since every material has a capacity to dissipate a certain amount of energy during cycling, the energy can be calculated by integrating the area inside the hysteresis loops. The strain energy based approach to fatigue life prediction

of materials with non-Masing behavior requires special attention, mainly because of the change in hysteresis loop shape with strain amplitude [3,149]. When the hysteresis loop shape changes continuously during fatigue, the half-life hysteresis loop is generally used for characterizing the fatigue properties and prediction of fatigue life of the material [3]. In case the material exhibits non-Masing response, the master curve approach is generally used. The master curve is constructed by matching the loading branches of the half-life hysteresis loops at different strain amplitudes [18]. It should be noted that it is not always possible to generate a master curve from the half-life hysteresis loops. When a material shows non-Masing behavior and the construction of a master curve is not possible, to the best of our knowledge no method exists in the open literature to estimate the cyclic plastic strain energy density, and thereby fatigue life.

This chapter presents a new method for predicting the cyclic plastic strain energy density and subsequently the fatigue life of materials, which show non-Masing behavior. The method uses the estimation of plastic strain energy density (*i.e.*, the hysteresis loop area) for the life prediction. The method does not require the construction of a master curve for the estimation of plastic strain energy density. Low cycle fatigue data have been generated for SS 304L, and the proposed method is implemented. The proposed method has been validated successfully with the LCF test data of other materials as well. The test data for these materials were obtained from different articles published by various authors.

2.2 Experimental details

Low cycle fatigue tests were performed on smooth specimens of 304L SS. The chemical composition (in % wt.) of the steel is C: 0.029, Si: 0.46, Mn: 1.74, Ni: 8.17, Cr: 18.16, N: 0.061, P: 0.033, S: 0.004 and balance Fe. The test specimens (**Figure 2.1**) were prepared as per ASTM E606 with gage diameter and length of 10 mm and 28 mm, respectively. The material was given solutionizing treatment at 1343 K for one hour, followed by air cooling. The tests were performed at room temperature at different strain amplitudes in the range of $\pm 0.25\%$ to $\pm 1.0\%$ at a constant strain rate of $1 \times 10^{-3} \text{ s}^{-1}$ under the fully reversed axial strain-controlled mode using symmetric triangular waveforms. The load drop of 20% was considered as a failure criterion for the fatigue life of the specimens. All the tests were performed on INSTRON 8862 servo-electric fatigue testing system.

A ferritescope (FERRITSCOPE FMP30, Fischer) was used to quantify the martensite transformed during the strain cycling. Measurements were acquired on the virgin and failed specimens at different locations within the gauge length. The ferritescope reading (*i.e.* ferrite number) was converted to the actual martensite content by using Talonen's correlation [150].

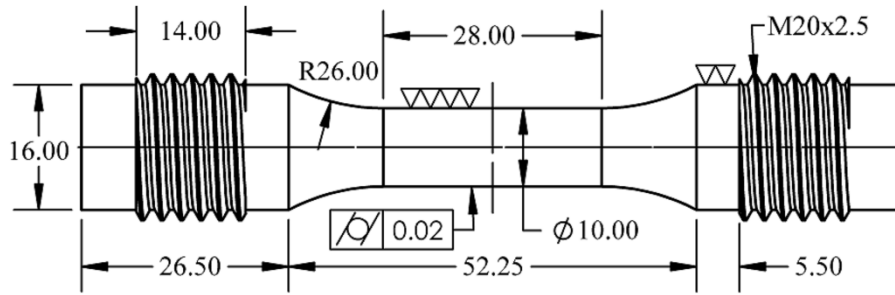


Figure 2.1 Low cycle fatigue testing specimen

2.3 Results

2.3.1 Cyclic stress response

The cyclic stress response of the material under strain-controlled fatigue at room temperature is shown in **Figure 2.2(a)**. At low strain amplitudes ($<\pm 0.4\%$), the material exhibited a relatively short period of cyclic hardening, followed by softening and saturation for a large number of cycles. The final failure took place after a significant decrease in peak stress. However, for high strain amplitude ($>\pm 0.4\%$) tests, significant secondary hardening prior to failure was observed. Since the extent of initial hardening, softening, and secondary hardening varied depending on the strain amplitude, a detailed investigation of cyclic stress response was carried out. The initial hardening (σ_1 to σ_2), softening (σ_2 to σ_3), and secondary hardening (σ_3 to σ_4) regions are highlighted for $\pm 1.0\%$ of strain amplitude in **Figure 2.2(a)**. The variation of Degree of Initial Hardening (DOIH), Degree of Softening (DOS) and Degree of Secondary Hardening (DOSH) as a function of strain amplitude are shown in **Figure 2.2(b)**. The DOIH, DOS and DOSH are defined as [151]; $\text{DOIH} = (\sigma_2 - \sigma_1)/\sigma_1$, $\text{DOS} = (\sigma_2 - \sigma_3)/\sigma_3$ and $\text{DOSH} = (\sigma_4 - \sigma_3)/\sigma_3$. The DOS decreased with an increase in strain amplitude, **Figure 2.2(b)**. However, DOIH and DOSH were found to increase with strain amplitude, **Figure 2.2(b)**.

It is well established that the dislocation-dislocation interactions, dislocation multiplication, the interaction of solute particles with dislocations are the factors responsible for initial hardening [12]. The dislocation cell structures which form due to the rearrangement of the dislocations during cyclic loading leads to subsequent cyclic softening as it provides a large mean free path to the dislocations [11]. The secondary hardening in this steel is associated with the deformation-induced martensite formation occurring during the strain cycling [42]. Das et al. [152] found that the cyclic softening decreases and secondary hardening increases as the amount of deformation-induced martensite increases. The formation of martensite depends on the volume fraction of annealing twins in the material and the applied strain amplitude [12]. It has been reported that several factors, such as material chemistry, stress/strain state, strain amplitude, strain rate, and temperature influence the formation of martensite during the LCF

[153]. The nucleation sites for the deformation-induced martensite formation are the annealing twins-shear bands intersection, grain boundary-shear band intersection, shear band-shear band intersection, etc. [154].

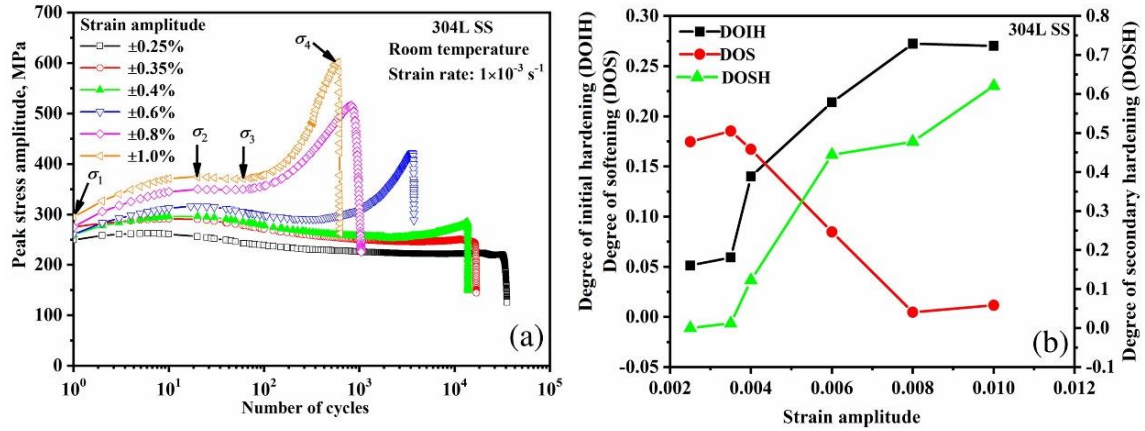


Figure 2.2 (a) The variation of peak tensile stress with cyclic loading at different strain amplitudes for 304L SS fatigue tested at room temperature. Initial hardening, softening and secondary hardening regions are marked by different σ -terms for $\pm 1.0\%$ of strain amplitude, (b) variation of degree of initial hardening (DOIH), degree of softening (DOS), and degree of secondary hardening (DOSH) of 304L SS with strain amplitude.

The variation of deformation induced martensite in the failed specimen with strain amplitude is shown in **Figure 2.3**. Measurements of martensite content were acquired at the fracture surface and two different locations, 2 mm and 10 mm away from the fracture surface. The ferritescope reading was converted to the actual martensite content by using Talonen's work [150]. According to which the amount of martensite content (mass %) = $1.7 \times$ ferrite number. The mass fraction of deformation induced martensite is found to increase with an increase in strain amplitude. Similar results were found by other researchers [30] as well. It is interesting to note that the martensite content increases toward the fracture surface and found to be maximum at the fracture surface. The high stress/strain concentration around the crack tip would have led to a higher amount of martensitic transformation on the fracture surface. As can be seen, the presence of martensite (around 5%) was observed even at very low strain amplitude tests ($\pm 0.25\%$). It should be noted that the martensite content in the untested specimen was almost zero. It indicates that the formation of martensite does not necessarily ensure the presence of secondary hardening in the cyclic stress response curve. Moreover, up to the strain amplitude of $\pm 0.35\%$, the cyclic hardening due to martensite formation is counterbalanced by the cyclic softening that occurs after initial hardening. As the strain amplitude increases, the rate of martensite formation increases and dominates over the cyclic softening. The similar observation has been reported by Raman and Padmanabhan [12]. Thus, the extent of cyclic

softening region decreases and the secondary hardening dominates most of the fatigue life at higher strain amplitudes. It can also be confirmed that martensitic transformation is one of the factors which is responsible for the non-Masing behavior of the material [30], which is evident from the significant amount of secondary hardening, especially at higher strain amplitudes.

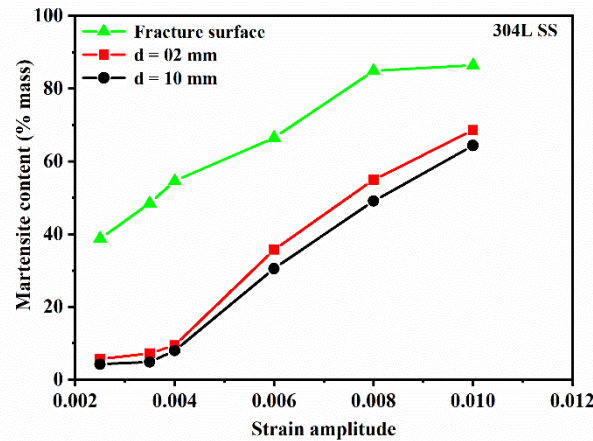


Figure 2.3 Variation of the martensite content with strain amplitude at the fracture surface and two different locations, 2 mm and 10 mm away from the fracture surface.

2.3.2 Assessment of non-Masing behavior

The fatigue behavior of a material is generally represented by the data obtained from the stabilized or half-life hysteresis loop. However, depending on the testing condition, the shape of the stabilized or half-life hysteresis loop might change with strain amplitude and thereby leading to Masing and non-Masing types of responses. In the present investigation, the hysteresis loops did not follow a common loading curve with a common origin, as shown in **Figure 2.4**, indicating that the material exhibited non-Masing behavior. The non-Masing behavior of the material has been investigated at 5%, 10%, 20%, 30%, 40% and 50% of fatigue life, where essentially the hysteresis loops were translated to merge the linear elastic portions to construct the master curves. It was observed that the master curve could be generated with the hysteresis loops for a lower fraction of fatigue life (up to 10% of fatigue life, **Figure 2.4(a)**). The common portion (OAB) of the loading branches of all the hysteresis loops is called the master curve. The master curve could not be constructed for life fractions higher than 10%. The data for 50 % life fraction is shown in **Figure 2.4(b)** as representation of non-Masing behavior observed for the material. It is straightforward to estimate the fatigue life when a material exhibits Masing behavior and non-Masing behavior (if the master curve can be constructed) [3]. However, if the material exhibits non-Masing behavior and the data cannot be represented in the form of a master curve, as shown in **Figure 2.4(b)**, no method is available in the open literature to estimate cyclic plastic strain energy density and thereby fatigue life. This is because the existing life prediction methods for non-Masing behavior, based on plastic strain energy

density calculation, takes into account the change in hysteresis loop shape with the help of a master curve. However, in many cases, the formation of a master curve is not possible, and there is a need for an alternative solution. To the authors' knowledge, no article in open literature has indicated this issue in the past. We propose a new method which does not require the generation of a master curve to estimate the cyclic plastic strain energy density and predict the fatigue life. This method can be used for both the Masing and non-Masing behaviors, irrespective of whether the master curve generation is possible or not.

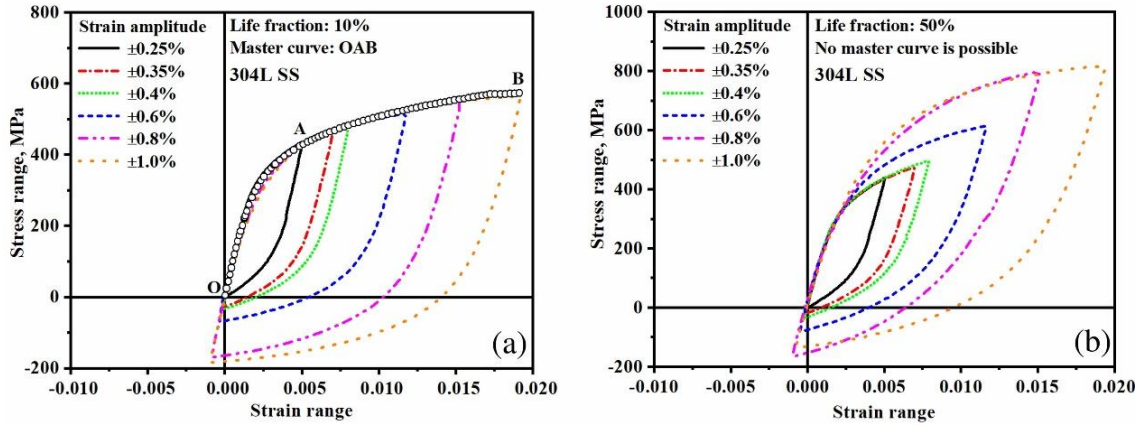


Figure 2.4 Hysteresis loops of 304L SS fatigue tested at different life fractions ((a) 10% and (b) 50%) translated to generate the master curves.

2.3.3 Proposed model for estimation of CPSED and fatigue life

The proposed model/method is based on the estimation of plastic strain energy density associated with hysteresis loop, *i.e.*, the area inside the stabilized hysteresis loop hereinafter referred to as cyclic plastic strain energy density (CPSED). The basic hypothesis of the proposed model is that when a material exhibits non-Masing behavior, the actual CPSED ($E_{nm,exp}$) is considered to be equal to the summation of the CPSED of its Masing behavior (E_m) and the additional CPSED (ΔE) term associated with the release of extra energy by the material due to non-Masing behavior, **Equation 2.1**.

$$E_{nm,exp} = E_m + \Delta E \quad 2.1$$

The basis of proposed approach considering stabilized/half-life hysteresis loops is shown in **Figure 2.5**. The hysteresis loop OABCO (in **Figure 2.5**) represents an experimental loop at half-life for relatively lower strain amplitude, considered to be a reference hysteresis loop. If the material shows Masing behavior, the half-life hysteresis loop at higher strain amplitude would be equivalent to OABDEO with respect to the reference loop OABCO. However, if the material exhibits non-Masing behavior, two different kinds of hysteresis loops can be formed, such as FOABIEF and FOAGHF, after translating the hysteresis loops. The loop FOABIEF represents non-Masing behavior in which the master curve can be generated by translating the

loop to merge the linear elastic portion with that of the reference loop OABCO. Whereas, the loop FOAGHF represents a situation in which the master curve cannot be generated.

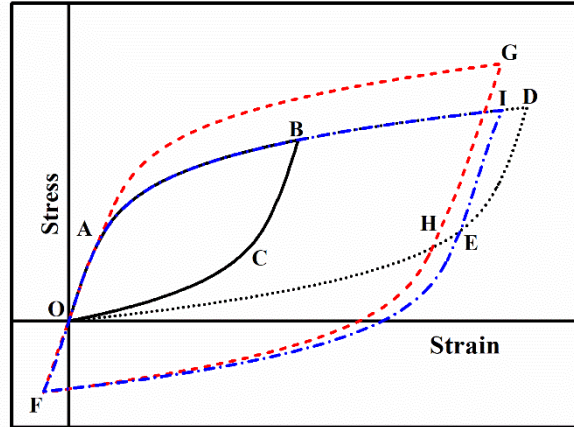


Figure 2.5 Schematic representation of different types of hysteresis loops for calculation of the plastic strain energy density for Masing and non-Masing behaviors.

Here, $E_{nm,exp}$ represents the CPSED of the loop FOABIEF or FOAGHF, *i.e.*, the experimental hysteresis loop area at half-life for a particular strain amplitude irrespective of whether the construction of master curve is possible or not. Whereas, E_m is the CPSED at half-life for the same strain amplitude, had the material behavior been Masing, *i.e.*, the area of the OABDEO loop in **Figure 2.5**. The hysteresis loop OABCO, obtained from fatigue test at a particular strain amplitude, can be used as the reference one to define the fatigue properties of the material. The loading part of stabilized hysteresis loops for other strain amplitudes, (say OABD of loop OABDEO), can be constructed assuming the Masing behavior and by extrapolating the loading part OAB to OABD. The CPSED (E_m) of the loop shape OABDEO generated by assuming Masing behavior can be estimated analytically as [45,94]:

$$E_m = \frac{1-n}{1+n} K (\Delta \varepsilon_p)^{n+1} \quad 2.2$$

Where, $\Delta \varepsilon_p$ is the plastic strain range and K and n are cyclic strength coefficient and cyclic strength exponent respectively obtained from the cyclic stress plastic strain range curve. This expression is very widely used in literature for the estimation of CPSED [45,94]. The parameters, K and n , can be obtained from the loading branch OAB of the hysteresis loop OABCO by fitting Ramberg-Osgood stress-strain relationship [155], as shown in **Equation 2.3**:

$$\Delta \varepsilon_t = \frac{\Delta \sigma}{E} + \left(\frac{\Delta \sigma}{K} \right)^{1/n} \quad 2.3$$

The half-life hysteresis loops for different strain amplitudes (as shown in **Figure 2.6(a)**) were constructed by extrapolating the loading branch of the experimental hysteresis loop at $\pm 0.25\%$ strain amplitude in **Figure 2.4(b)**. It may be noted that these hysteresis loops in **Figure 2.6(a)**

represent an ideal Masing behavior of the material. The relationship between the plastic strain range ($\Delta\varepsilon_p$) and total strain range ($\Delta\varepsilon_t$) was obtained and found to be linear, as shown in **Figure 2.6(b)** and expressed by **Equation 2.4**.

$$\Delta\varepsilon_p = S_1 \times \Delta\varepsilon_t + S_2 \quad 2.4$$

Where $S_1 = 0.9374$ and $S_2 = -0.002$ for 304L SS.

By replacing $\Delta\varepsilon_p$ (**Equation 2.4**) in **Equation 2.2**, the expression for E_m can be rewritten to calculate it for any strain amplitude, **Equation 2.5**.

$$E_m = \frac{1-n}{1+n} K (S_1 \times \Delta\varepsilon_t + S_2)^{n+1} \quad 2.5$$

In order to estimate the extra energy associated with non-Masing response, the **Equation 2.1** is rewritten as:

$$E_{nm,exp} = \frac{E_m}{1 - E_f} \quad 2.6$$

Where,

$$E_f = \frac{\Delta E}{E_{nm,exp}} = f(\varepsilon_t) \quad 2.7$$

The parameter E_f is a dimensionless quantity (normalized CPSED difference,) and depends on strain amplitude since the parameters ΔE and E_{nm} are strain dependent.

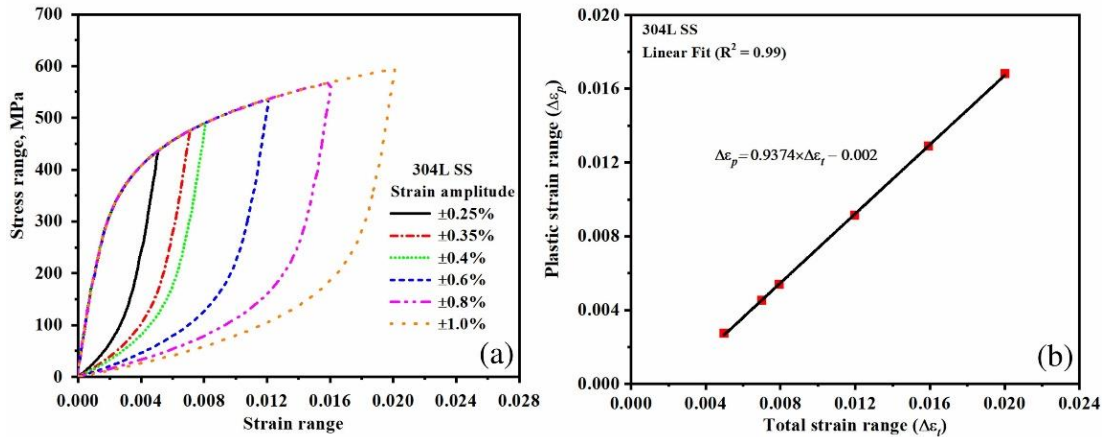


Figure 2.6 (a) Hysteresis loops constructed by extrapolation of the loading branch of the experimental hysteresis loop from $\pm 0.25\%$ strain amplitude represents an ideal Masing behavior and (b) variation of plastic strain range with total strain range.

In order to estimate E_f , the value of ΔE for a given strain amplitude is calculated as the difference between the CPSED of the experimental half-life hysteresis loop (**Figure 2.4(b)**) and the CPSED of the half-life hysteresis loop generated by considering Masing behavior (**Figure 2.6(a)**). The value of $E_{nm,exp}$ is calculated from the experimental half-life hysteresis loop (**Figure 2.4(b)**). As can be seen in **Equation 2.7**, if the normalized CPSED difference (E_f)

varies in a definitive manner with strain amplitude ε_t , *i.e.*, if there exists some kind of relationship between the parameter E_f and strain amplitude, which can be obtained from a limited number of experiments, such a relationship can be used for prediction of E_f at any strain amplitude.

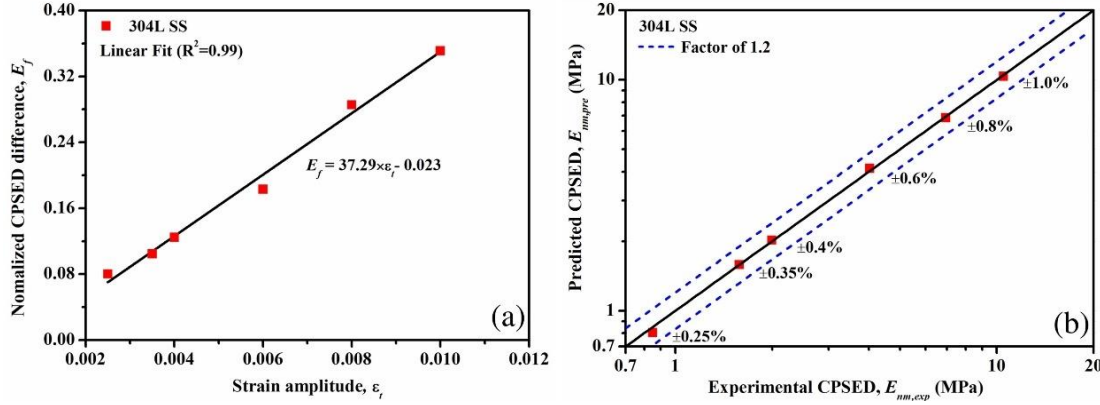


Figure 2.7 (a) The variation of normalized CPSED difference with strain amplitude for 304L SS, (b) comparison of the predicted and the experimental cyclic plastic strain energy densities for the 304L SS.

The E_f , predicted this way, can be used in **Equation 2.6** for the prediction of CPSED at any strain amplitude for a material showing non-Masing behavior. That means the **Equation 2.6** can be redefined as follows, **Equation 2.8**.

$$E_{nm,pre} = \frac{E_m}{1 - E_f} \quad 2.8$$

Effort is made to find out the definitive nature of the **Equation 2.7**, *i.e.*, the relationship between the E_f and ε_t . The estimated normalized CPSED difference (E_f) for the experimental hysteresis loops at half-life (**Figure 2.4(b)**) is plotted as a function of strain amplitude in **Figure 2.7(a)**. It is interesting to note that a linear behavior is observed for the 304L stainless steel. The linear relationship enables the prediction of E_f for any strain amplitude, **Equation 2.9**:

$$E_f = S_3 \times \varepsilon_t + S_4 \quad 2.9$$

Where $S_3 = 37.29$ and $S_4 = -0.023$ for 304L SS. The value of the normalized CPSED difference parameter (E_f) at a particular strain amplitude indicates the extent of non-Masing behavior. The value of E_f increases with strain amplitude due to increase in the martensite fraction and microstructural heterogeneities, indicating more deviation from the Masing behavior. The physical significance of the constants (S_3 & S_4) has been given in **Section 3.3.2**.

The value of E_m for each strain amplitude is calculated using **Equation 2.5**. The material constants (K and n) required for the estimation of E_m have been obtained from the experimental hysteresis loop at the lowest strain amplitude ($\pm 0.25\%$) in **Figure 2.4(b)**. The cyclic strength

coefficient (K) and cyclic strength exponent (n) were found to be 1237 MPa and 0.177 respectively. Following the estimation of E_m using **Equation 2.5**, and E_f using the **Equation 2.9**, the **Equation 2.8** can be rewritten as **Equation 2.10**.

$$E_{nm,pre} = \frac{E_m}{1 - E_f} = \frac{1 - n}{1 + n} K \frac{(S_1 \times \Delta \varepsilon_t + S_2)^{n+1}}{1 - (S_3 \times \varepsilon_t + S_4)} \quad 2.10$$

Thus, for 304L SS, the CPSED can be predicted for any strain amplitude using **Equation 2.10**. The comparison of the predicted CPSED ($E_{nm,pre}$) and the experimental CPSED ($E_{nm,exp}$) at half-life is shown in **Figure 2.7(b)**. The dash lines represent the boundaries of a scatter factor 1.2. It is evident from **Figure 2.7(b)** that the proposed method could accurately predict the cyclic plastic strain energy density of the half-life hysteresis loops at all the strain amplitudes.

The fatigue damage is associated with the accumulation of plastic strain during cyclic loading. Therefore, the estimation of cyclic plastic strain energy density plays an important role in the prediction of fatigue life. For the 304L SS material, a power law correlation (**Equation 2.11**) between the CPSED ($E_{nm,pre}$) predicted by using **Equation 2.10** and experimental fatigue life ($N_{f,exp}$) could be established, as shown in **Figure 2.8(a)**. Such a power law correlation had been used by other researchers as well for the prediction of fatigue life [3,156].

$$E_{nm,pre} = K_1 (N_{f,exp})^{n_1} \quad 2.11$$

Where $K_1 = 357.35$ MPa and $n_1 = -0.554$ for 304L SS.

Thus, one can predict the $E_{nm,pre}$ from **Equation 2.10** and use it in **Equation 2.11** to predict fatigue life for any strain amplitude. Combining **Equation 2.10** and **Equation 2.11**, the equation for prediction of fatigue life ($N_{f,pre}$) can be given as **Equation 2.12**.

$$N_{f,pre} = \left(\frac{E_m}{K_1 (1 - E_f)} \right)^{1/n_1} = \left(\frac{1 - n}{1 + n} K \frac{(S_1 \times \Delta \varepsilon_t + S_2)^{n+1}}{1 - (S_3 \times \varepsilon_t + S_4)} \right)^{1/n_1} \quad 2.12$$

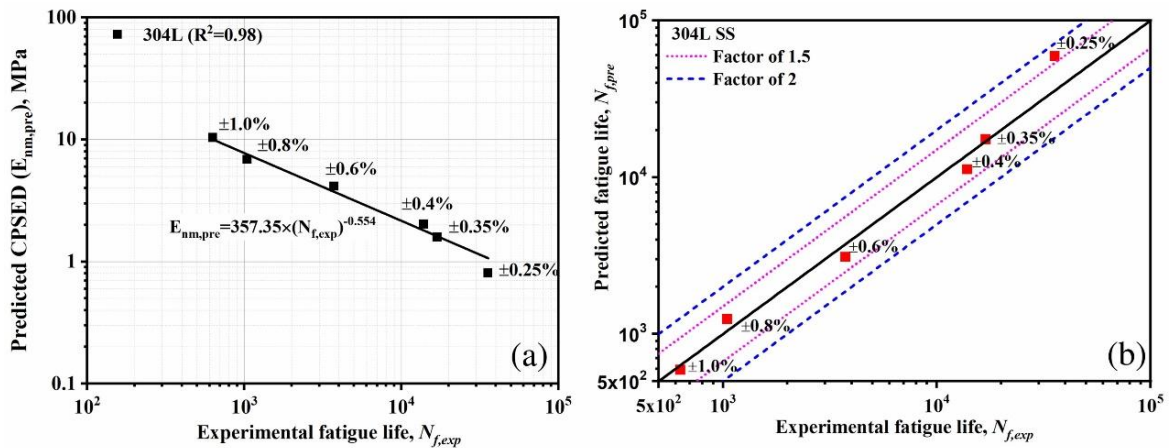


Figure 2.8 (a) Predicted cyclic plastic strain energy density vs. experimental fatigue life plots for 304L SS material, (b) comparison of the experimental and predicted fatigue lives.

The fatigue life predicted by using **Equation 2.12** is compared with the experimental data in **Figure 2.8(b)**. The dot and dash lines represent the boundaries of the scatter bands of factors 1.5 and 2, respectively.

As can be seen, most of the data points lie within the scatter band of 1.5. However, at low strain amplitude *i.e.*, when the strain amplitude approaches towards elastic limit or fatigue behavior approaches towards the high cycle fatigue regime, the scatter factor increases to almost 2. Similar scatter in fatigue life prediction (factor 2 or more) have been reported by other authors, especially when **Equation 2.11** type of power-law correlation is used [156]. The large scatter at lower strain amplitude or higher life ($>10^4$ cycles) might have occurred because of the bilinear behavior of the CPSED vs. fatigue life plot in log-log scale that could not be captured by the power law equation (**Equation 2.11**).

Table 2.1 The source of the extracted LCF data and the estimated values of the different constants associated with the proposed and existing methods.

Material	Reference	Constants of Eq. 2.3 [K, n]	Constants of Eq. 2.4 [S_1, S_2]	Constants of Eq. 2.9 [S_3, S_4]	Constants of Eq. 2.11 [K_1, n_1] (Proposed method)	Constants of Eq. 2.11 [K_1, n_1] (Existing method)
304LN SS	Sivaprasad et al. [30]	1338, 0.140	0.9652, -0.0032	25.168, -0.153	3740.45, -0.862	4448.06, -0.888
316LN SS	Roy et al. [94]	1267, 0.151	0.9527, -0.0023	43.091, -0.114	1317.94, -0.709	1088.08, -0.679
SA333 Gr. 6	Sivaprasad et al. [30]	1237, 0.116	0.9723, -0.0032	12.317, -0.047	1808.25, -0.804	1812.67, -0.813
AA6063	Nandy et al. [82]	302, 0.079	0.9615, -0.0028	32.839, -0.098	206.31, -0.722	205.03, -0.729
AISI 1018 HR Steel	Plumtree and Abdel-Raouf [15]	1012, 0.117	0.9683, -0.0024	12.861, -0.021	46.95, -0.227	43.39, -0.222
Annealed Cu	Mahato et al. [122]	886, 0.199	0.9291, -0.0019	37.273, -0.021	51.46, -0.456	34.78, -0.408
Annealed Al	Mahato et al. [122]	245, 0.133	0.9667, -0.0017	20.403, 0.037	141.42, -0.733	97.06, -0.686

2.3.4 Validation of proposed model

The proposed model/method has been further validated with different materials which show non-Masing behavior. The test data (*i.e.*, half-life/stabilized hysteresis loops and fatigue lives at different strain amplitudes) for the materials were extracted from published articles (as mentioned in **Table 2.1**) available in open literature. The proposed model, as explained in

Section 2.3.3, has been implemented for these materials. **Table 2.1** shows the estimated values of the different material parameters and constants associated with different equations of **Section 2.3.3**. At first, the constants K and n were estimated using **Equation 2.3**. Then, the linear relationships between $\Delta\varepsilon_p$ and $\Delta\varepsilon_t$ (i.e. similar to **Equation 2.4**) were determined by constructing the idealized Masing hysteresis loops; the constants of the equations (S_1 and S_2) are shown in **Table 2.1**. After that, using **Equation 2.5**, E_m has been estimated for all the materials. As $E_{nm,exp}$ is known (obtained from the extracted data), ΔE and then E_f could be estimated for all the materials using **Equation 2.1** and **Equation 2.7**, respectively.

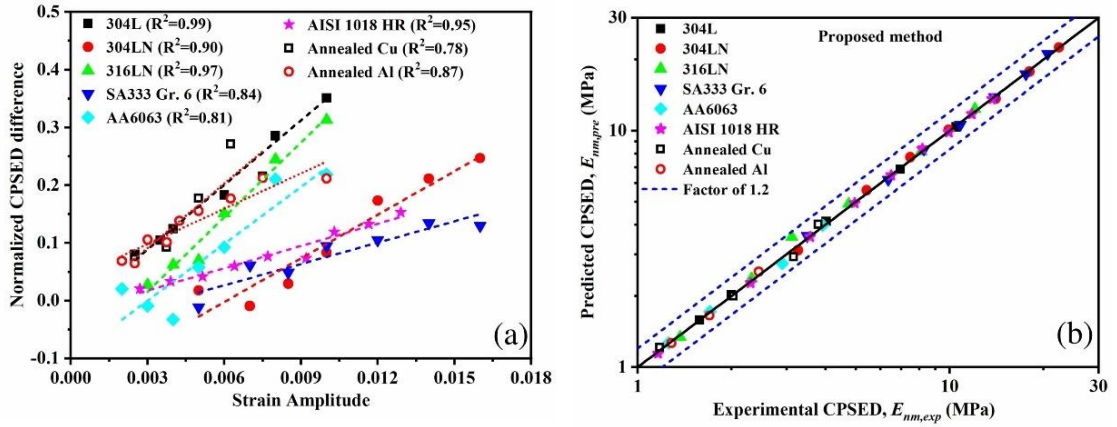


Figure 2.9 (a) Normalized CPSED difference vs. strain amplitude plots for all materials. Linear fit curves are also shown, (b) comparison of the predicted and the experimental cyclic plastic strain energy densities of the hysteresis loops for all materials.

It is interesting to note that for all the materials, the normalized CPSED difference (E_f) vs. strain amplitude (ε_t) plots show almost linear behavior, shown in **Figure 2.9(a)**. Therefore, linear equations similar to **Equation 2.9** could be developed for all the materials. The constants of the equations (S_3 and S_4) are shown in **Table 2.1**. The material parameters (K , n , S_1 , S_2 , S_3 and S_4) obtained for all the materials have been used in **Equation 2.10** for the prediction of CPSEDs, $E_{nm,pre}$. The comparison of the predicted CPSEDs ($E_{nm,pre}$) and the experimental CPSEDs ($E_{nm,exp}$) is shown in **Figure 2.9(b)**. It is interesting to note that the proposed method could predict the CPSEDs well within a scatter factor of 1.2.

The predicted CPSEDs ($E_{nm,pre}$) vs. experimental fatigue lives ($N_{f,exp}$) are plotted in **Figure 2.10(a)** and the material constants K_1 and n_1 have been determined (as shown in **Table 2.1**) for all the materials using the power-law relationship of **Equation 2.11**. Then, the fatigue lives are predicted for all materials using **Equation 2.12**. The predicted fatigue lives ($N_{f,pre}$) are compared with the experimental fatigue lives ($N_{f,exp}$) in **Figure 2.10(b)**. It is interesting to note that 84% of the predicted data lie well within a scatter factor of 1.5 for all the materials.

The remaining 16% of data points from the high cycle fatigue regime (*i.e.*, life $\geq 10^4$ cycles) lie within a scatter factor of almost 2. The high scatter at higher life can be correlated with the deviation of data points from power-law fitting at higher life in **Figure 2.10(a)**. Thus, it is evident that the power-law relationship can provide a better life prediction in the low cycle fatigue regime.

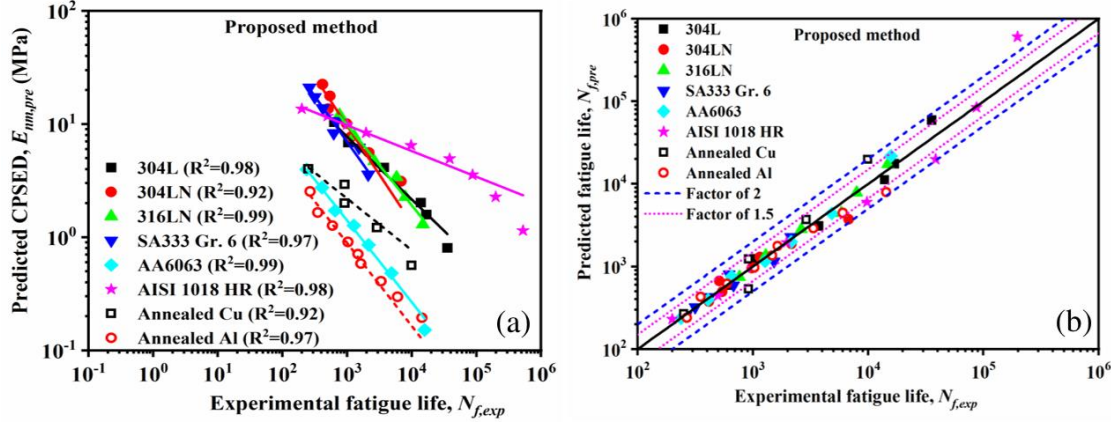


Figure 2.10 (a) Predicted cyclic plastic strain energy density vs. experimental fatigue life plots for all materials, (b) comparison of the experimental and predicted fatigue lives for all materials.

2.4 Discussion

For materials exhibiting Masing behavior, the prediction of CPSED, E_m (thereby fatigue life) is straight forward as material parameters do not vary with strain amplitude. In such cases, **Equation 2.2** (or a similar one) can be used to calculate the CPSED, followed by **Equation 2.11** (assuming $E_{nm,pre} = E_m$) or **Equation 2.12** (assuming $E_f = 0$) to predict fatigue life. The material constants K and n can be obtained from the common loading branch of the hysteresis loops. However, if a material exhibits non-Masing behavior, the material parameters change with strain amplitude owing to the change in hysteresis loop shape. The non-Masing behavior can be further classified into two categories; Category-I: in which a master curve can be constructed, and Category-II: in which a master curve cannot be constructed. For Category-I materials, a method is available in the literature [3] for the estimation of plastic strain energy density (as shown in **Equation 2.13**); and then prediction of fatigue life by using **Equation 2.11**.

$$E_{nm,pre} = \frac{1 - n'}{1 + n'} \Delta\sigma \Delta\varepsilon_p + \frac{2n'}{1 + n'} \delta\sigma_0 \Delta\varepsilon_p \quad 2.13$$

Here n' is the cyclic hardening exponent of the master curve and $\delta\sigma_0$ measures the change in proportional limit of the hysteresis loops with strain amplitudes caused by non-Masing behavior.

Our test data for 304L SS falls under Category-II; hence master curve could not be constructed (see **Figure 2.4(b)**), and in **Equation 2.13** could not be used for the estimation of CPSED. This highlights the limitation of the existing method (in **Equation 2.13**) for the estimation of the CPSED and prediction of fatigue life. To overcome these difficulties, we proposed the method explained in **Section 2.3.3**. The proposed method does not require the construction of a master curve. The parameter E_f (normalized CPSED difference) takes into account the non-Masing behavior irrespective of whether construction of master curve is possible or not. The observation in **Figure 2.9(a)** strongly suggests that the parameter E_f gives a more general and fundamental definition and quantification of non-Masing behavior of material. Moreover, if a material exhibits Masing response, the parameter E_f will be zero, and the **Equation 2.8** will become equivalent to **Equation 2.2**, and thus estimates the CPSED for Masing behavior. Therefore, the method can be applied to both Masing and non-Masing responses.

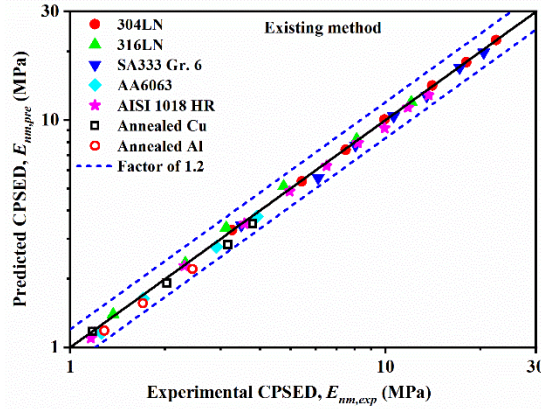


Figure 2.11 Comparison of experimental and predicted values of cyclic plastic strain energy densities. The prediction was made by using the existing method (master curve approach: **Equation 2.13**).

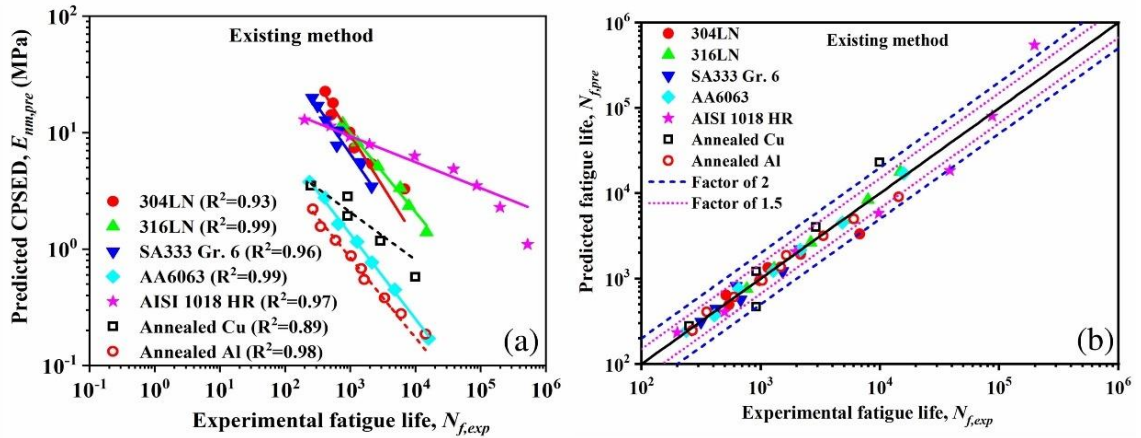


Figure 2.12 (a) Predicted cyclic plastic strain energy density vs. experimental fatigue life plots for all materials. The prediction of CPSED was made by using the existing method (master curve approach: **Equation 2.13**), (b) comparison of experimental and predicted fatigue lives. The prediction was made by using the existing method (master curve approach **Equation 2.13**).

As shown in **Section 2.3.4**, the proposed method is very general in nature as it could be used for our test material as well as for all the materials for which data were extracted from the literature. For the Category-I materials (*i.e.*, the extracted data), the CPSEDs were predicted by using the existing method (**Equation 2.13**), and then the fatigue lives were predicted using **Equation 2.11**. The detailed implementation of the method (**Equation 2.13**) is not explained here. It can be found in our earlier publication [94]. **Figure 2.11** shows the comparison of the predicted and experimental CPSEDs. The predicted CPSEDs ($E_{nm,pre}$ obtained from **Equation 2.13**) vs. experimental fatigue lives ($N_{f,exp}$) are plotted in **Figure 2.12(a)**, and the material constants K_1 and n_1 have been determined (as shown in **Table 2.1**) for all the materials using the power-law relationship of **Equation 2.11**. Then, the fatigue lives are predicted for all the materials using **Equation 2.11**. **Figure 2.12(b)** shows the comparison of predicted and experimental fatigue life.

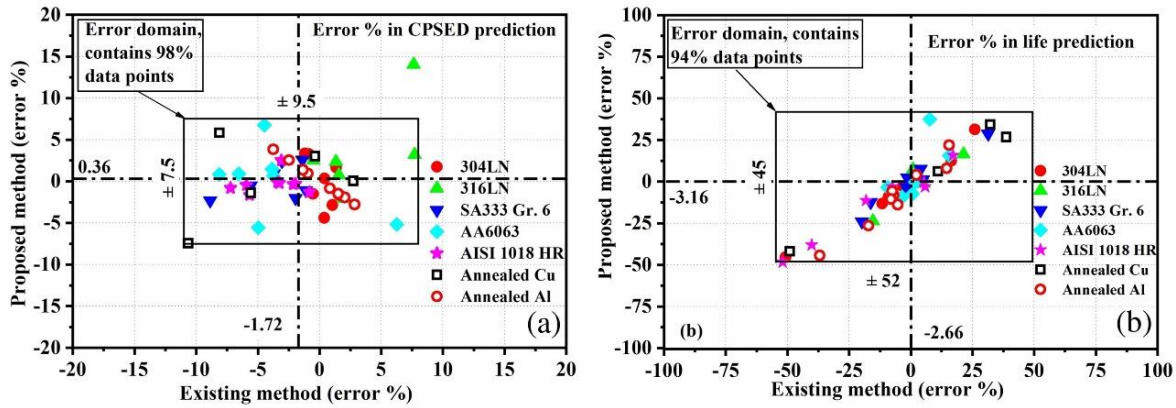


Figure 2.13 Comparison of error percentage in the prediction of (a) CPSED and (b) fatigue life obtained by the proposed new method and the existing method (master curve approach). Total number of data points is 50 in each plot.

As can be seen from **Figure 2.11**, the existing method also provides the prediction of CPSED within a scatter factor of 1.2. It should be noted that **Equation 2.13** can be used only when the estimate of $\delta\sigma_0$ is known, thus can not be used for prediction of CPSED for unknown strain amplitude. **Figure 2.12(b)** shows that the existing method predicts fatigue life within a scatter factor of 1.5 for almost 81% of the data points which lie in the low cycle fatigue region (*i.e.*, life $\leq 10^4$ cycles). The remaining 19% of the data points lie within a scatter factor of almost 2. However, when we compare the proposed new method with the existing method (master curve approach) in terms of the error percentage in the prediction of CPSED and fatigue life (as shown in **Figure 2.13**), we can highlight some advantages of the proposed method over the existing method. The error percentage is calculated as $100 \times (\text{predicted value} - \text{experimental value}) / \text{experimental value}$.

value)/experimental value. As can be seen in **Figure 2.13(a)**, the existing method gives a mean error value of -1.72% in CPSED prediction, whereas the proposed method gives a value of 0.36%. Moreover, from statistical analysis of the 50 data points, it is found that with the existing method, 98% of the data points could be predicted within an error limit of $\pm 9.5\%$ from the mean value. However, with the proposed method, the error limit is found to be $\pm 7.5\%$. Thus statistically, the proposed method gives a better prediction, whereas the existing methods mostly underestimated the CPSED with a relatively wide range of error. A similar statistical analysis of the error percentage in life prediction (**Figure 2.13(b)**) reveals a mean error value of -2.66% for the existing method compared to that of -3.16% obtained by the proposed new method. The error limit for the existing method is found to be $\pm 52\%$ compared to the error limit of $\pm 45\%$ obtained by the proposed new method. Thus, it is evident that the proposed method gives a better prediction of fatigue life.

2.5 Superiority of the proposed model

The proposed model (**Section 2.3.3**) has some advantages over the existing methods of fatigue life prediction,

1. The available methods, such as the Basquin relationship and Coffin-Manson relationship, are based on a single parameter, *i.e.*, stress or strain. However, the proposed model is based on the cyclic plastic strain energy density (CPSED), which takes into account the influence of stress and strain simultaneously. Therefore, the CPSED is a more fundamental quantity as far as the material behavior is concerned, and used in the proposed model to predict the fatigue life.
 2. Moreover, under complex loading condition, *e.g.*, under variable amplitude loading of mixed stress and strain control modes, the use of CPSED for life prediction would become easier than stress-based or strain-based life prediction methods.
 3. The model gives us an estimation of the energy (a scalar quantity) absorbed by materials exhibiting the Masing/non-Masing behavior. The “normalized CPSED difference,” a quantity used in the proposed model, can also be used to quantify the degree of non-Masing behavior of materials.
 4. The model could predict the CPSED and the fatigue life within the scatter bands of 1.2 and 2.0, respectively, for 13 different materials irrespective of Masing, Type-I non-Masing, and Type-II non-Masing behaviors, indicating the universal nature of the model. Refer to **Chapter 3** for the model validation with the different materials.
 5. It is a simple and handy relationship that requires a few LCF tests (at least three) to estimate the material constants, and then it can be used to predict the CPSED and fatigue
-

life for any unknown amplitude. No need to construct the master curve, and predication can be done for any unknown strain amplitude.

2.6 Summary and conclusions

Low cycle fatigue tests were conducted on 304L stainless steel at room temperature. The material exhibited Masing behavior at lower strain amplitudes and non-Masing behavior at higher strain amplitudes. The change from Masing to non-Masing behavior after $\pm 0.4\%$ of strain amplitude seems to correlate very well with the significant change in martensite content after the same level of strain amplitude. Thus, non-Masing behavior is considered to be caused by the strain induced martensitic transformation. The following conclusions can also be drawn from the investigation.

1. In the literature, material behavior is classified into two categories: Masing and non-Masing. We discovered a new kind of non-Masing behavior, termed the Type-II non-Masing behavior. Thus, the non-Masing behavior of materials has been classified into two categories, viz. (i) Type-I non-Masing behavior (i.e., when construction of the master curve is possible) and (ii) Type-II non-Masing behavior (i.e., when construction of the master curve is not possible).
 2. The existing method available in the literature for the estimation of cyclic plastic strain energy density requires the construction of a master curve in case of non-Masing behavior. The master curve could not be constructed for 304L SS with the hysteresis loops obtained at the life fractions beyond 10%. Thus, the fatigue life could not be predicted with the existing method available in the literature.
 3. A new method is proposed for the estimation of cyclic plastic strain energy density and prediction of fatigue life for the 304L SS and further validated with seven different materials. The method is found to give a very good prediction of the cyclic plastic strain energy density. The fatigue life of all the materials could also be predicted within a scatter factor of 1.5 in the low cycle fatigue regime (life $\leq 10^4$ cycles) and within a scatter factor of 2 beyond the low cycle fatigue regime. The method proposed is very general in nature and can be used for any material irrespective of Masing or non-Masing behavior.
 4. The proposed method quantifies the non-Masing behavior in terms of a strain energy density based non-dimensional parameter, termed as “normalized cyclic plastic strain energy density difference.” This non-dimensional parameter is found to vary almost linearly with strain amplitude for all the materials. Thus, this parameter provides a more
-

general and fundamental definition and quantification of non-Masing behavior of material compared to those available in the literature.

2.7 Some highlights and remarks

Some highlights of the chapter:

- A model has been proposed to predict CPSED and hereby fatigue life of different classes of materials, including Masing, Type-I, and Type-II non-Masing behavior, without constructing the master curve, which indicates the universal nature of the proposed method.
- It can predict the CPSED and the fatigue life within the scatter bands of 1.2 and 2.0, respectively, and it has been validated with eight different classes of materials.
- The model is simple and uses some handy relationships that require a few LCF tests (at least three) to estimate the material constants; then, it can be used to predict the CPSED and fatigue life for any unknown amplitude.
- Based on the extensive analysis, the non-Masing behavior has been classified into two categories, viz., (i) Type-I (construction of master curve is possible), and (ii) Type-II (construction of master curve is possible) non-Masing behavior.

Remarks:

This chapter discusses a model/method that could predict CPSED and fatigue life of eight materials within a scatter band of 1.2 and 1.5, respectively. In the next chapter, the model has been validated with six more materials, out of which three show Type-I and the other three show Type-II non-Masing behavior. The five materials exhibiting the Type-I and Type-II non-Masing have been identified from the literature through an extensive process of data extraction and analysis.



Chapter – 3

3. Validation of Proposed Model

This chapter includes the results of a journal article [19] published in the Transactions of the Indian National Academy of Engineering (volume: 7, issue: 2 and pages: 411-416). The details of the article are given below. Some additional contents are also included, which could not be presented in the article.

Prediction of Cyclic Plastic Strain Energy Density and Fatigue Life of Non-Masing Behavior Materials without Master Curve

Sanjeev Singh Yadav^{*a}, Samir Chandra Roy^a, J. Veerababu^b and Sunil Goyal^c

^aDepartment of Mechanical Engineering, Indian Institute of Technology Ropar, Rupnagar, Punjab, 140001, India

^bMaterials Development and Technology Division, Indira Gandhi Centre for Atomic Research, Kalpakkam, Tamil Nadu, 603102, India

^cNuclear Fuel Complex, Kota Project, Rawatbhata, Rajasthan, 323303, India

*Corresponding author e-mail: 2018mez0004@iitrpr.ac.in

Abstract

Masing/non-Masing behavior of material plays an important role in the strain energy-based methods of fatigue life prediction. Materials under fatigue are found to show three distinct categories of behavior viz. Masing, non-Masing (Type-I: when master curve can be constructed) and non-Masing (Type-II: when master curve cannot be constructed). The master curve method available in the literature for the estimation of cyclic plastic strain energy density (CPSED) can be used only for Type-I non-Masing and Masing behaviors of materials. Moreover, it could be used for estimation only, not for prediction of CPSED. Very recently (in 2021), a new method, as summarized in this article, was proposed for the prediction of CPSED and fatigue life of material irrespective of Masing or non-Masing (Type-I and Type-II) behavior. Although the method was developed, the validation of the proposed method with different Type-II non-Masing behavior materials remained a matter of further investigation. As Type-II non-Masing behavior was not highlighted earlier in the literature, such data is not readily available. In this article, we conducted low cycle fatigue tests on SS 304L material, and after an extensive literature review and analysis, three materials' data for each of Type-I and Type-II non-Masing behaviors could be collected. The method of prediction of CPSED and fatigue life is summarized and implemented on the six different materials. The CPSED and fatigue life could be predicted within a scatter band of 1.2 and 2, respectively. This article confirms the universal nature of the new method of CPSED and fatigue life prediction.

Keywords: Masing/non-Masing; Plastic strain energy density; Fatigue life assessment; Master curve

3.1 Introduction

In the case of Masing behavior, loading branches of the hysteresis loops follow the same loading curve irrespective of strain amplitude; however, it is not the case for non-Masing behavior [16]. Stable microstructural [16] response is found to be exhibited by materials showing Masing behavior under low cycle fatigue. However, materials undergoing various substructural and microstructural changes exhibit non-Masing behavior. Nellessen et al. [51] observed an increase in dislocation density and cell formation with strain amplitude in austenitic stainless steel. Such dislocation cell formation is reported to be responsible for the non-Masing behavior of materials [15,52]. Sivaprasad et al. [30] have reported martensitic transformation and unstable dislocation substructure associated with non-Masing behavior of 304LN SS. Thus, understanding Masing/non-Masing behavior has a great significance in material development and life prediction.

The non-Masing behavior of materials can be classified further into two categories based on the possibility of master curve formation viz. Type-I non-Masing behavior (i.e., when construction of the master curve is possible) and Type-II non-Masing behavior (i.e., when construction of the master curve is not possible). The model of prediction of the cyclic plastic strain energy density [3] and thereby fatigue life is available in the literature for Type-I non-Masing behavior. However, there are materials that fall under the Type-II non-Masing behavior [6,8] category. Authors in article [7] have highlighted this point and proposed a model to estimate the CPSED and fatigue life for Type-II non-Masing behavior of materials.

The main advantage of the proposed model is that it can also be used for materials exhibiting Type-I non-Masing behavior and Masing behavior. The proposed model was verified with different grades of materials showing Masing behavior and Type-I non-Masing behavior in article [7]. However, due to the unavailability of data for Type-II non-Masing behavior, the versatility of the proposed model could not be verified with different materials. Therefore, in the present article, the validation of the proposed model has been done for three of each of Type-I and Type-II non-Masing behavior materials. The proposed model was validated with 304L SS for which data were generated through LCF tests conducted at room temperature, and data (hysteresis loops and fatigue life) for other materials had been extracted from published articles available in the open literature. The material data were extracted for BLY160 steel from [8], AISI 321 SS from [6], LY225 steel from [5], HSS Q960E from [91], and AL6XN steel from [157]. It was found that the proposed model could estimate the CPSED and fatigue life within a scatter band of 1.5 and 2, respectively. The data for Type-II non-Masing behavior was not readily available in the literature as this kind of behavior of material was not highlighted by

others in the literature, and it is difficult to predict that material would exhibit such behavior under fatigue.

3.2 Test data

Low cycle fatigue tests were performed on 304L SS. The experimental details are given in **Section 2.2**.

3.3 Results and discussion

3.3.1 Analysis of non-Masing behavior

The non-Masing behavior of materials is characterized by the hysteresis loops not following a common loading curve irrespective of the strain amplitude. When materials show the non-Masing behavior, the construction of the master curve (**Figure 3.1(a)**) is a primary requirement to estimate the CPSED and thereby fatigue life [18]. An effort was made to obtain the master curve for 304L SS from different hysteresis loops at half-life, and it was found that master curve construction is not possible, as shown in **Figure 3.1(b)**. To verify the master curve formation at half-life for other materials, the literature data were analyzed and a similar trend was also found to be associated with BLY160 steel and AISI 321 SS, as shown in **Figure 3.2**. This is called Type-II non-Masing behavior. Authors in article [7] have proposed a model to predict CPSED and subsequently fatigue life of materials that exhibit Type-II non-Masing behavior. The proposed model is simple and versatile because it can be used for all types of behavior, such as Type-I, Type-II non-Masing, and Masing behavior. In this chapter, the proposed model has been validated with six different materials of non-Masing behavior.

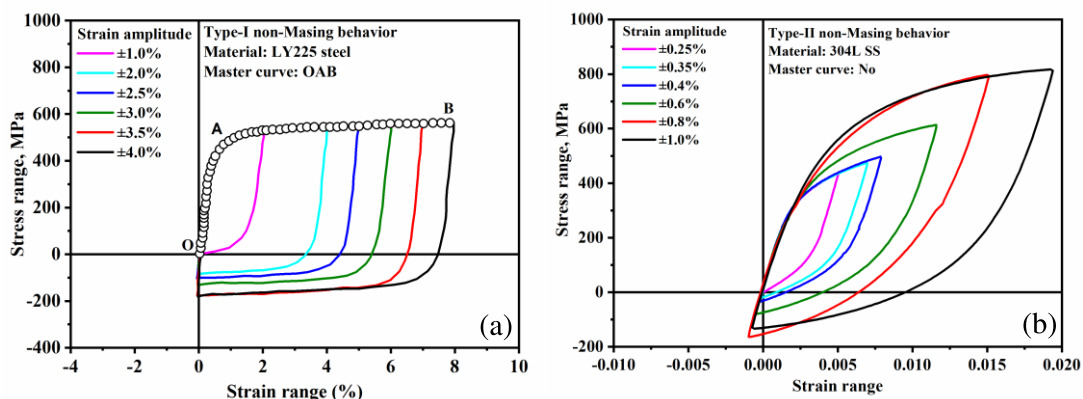


Figure 3.1 Representation of (a) Type-I and (b) Type-II non-Masing behavior for LY225 steel [5] and 304L SS [7], respectively.

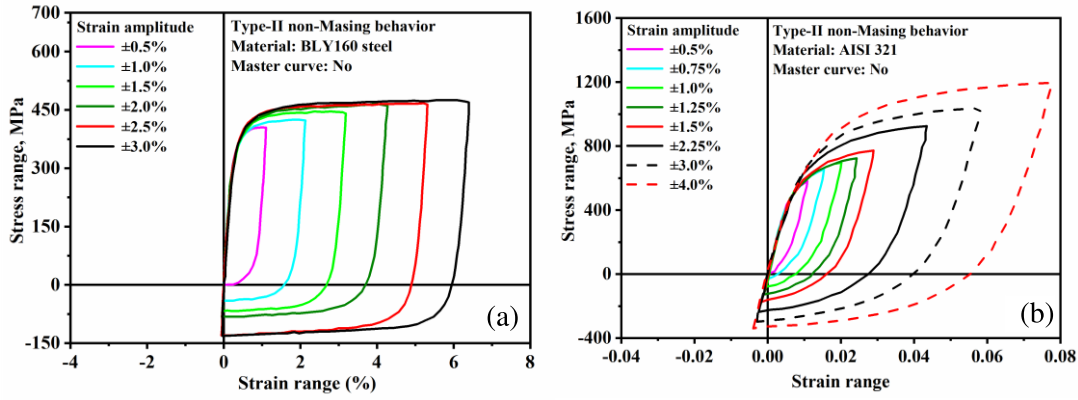


Figure 3.2 Construction of master curve at half-life for two different materials (a) BLY160 steel [8] and (b) AISI 321 SS [6].

3.3.2 Validation of the proposed model

A parameter (**Equation 2.7**), “normalized CPSED difference,” E_f , is defined as a ratio of the change in CPSED (ΔE) due to non-Masing behavior to the overall or actual CPSED ($E_{nm,exp}$) at a particular strain amplitude [7]. Normalized CPSED difference was calculated for all six materials, and the variation of normalized CPSED difference is plotted with the strain amplitude (**Figure 3.3**). It is interesting to note that the normalized CPSED difference varies almost linearly for all materials. Therefore, the normalized CPSED difference can be expressed (similar to **Equation 2.9**) as mentioned in **Chapter 2** [7]. The material constants (S_3 and S_4) are given in **Table 3.1**. The level of the non-Masing response is estimated by the normalized CPSED difference parameter (E_f), which increases with an increase in strain amplitude depending on the slope (S_3) and intercept (S_4). The parameter S_3 represents the rate at which material deviates from Masing behavior, and S_4 gives an estimate of E_f for strain amplitude close to zero. Ideally, the value of E_f should be zero at zero strain amplitude. Nevertheless, as shown in **Table 3.1**, the values of S_4 for different materials are close to zero.

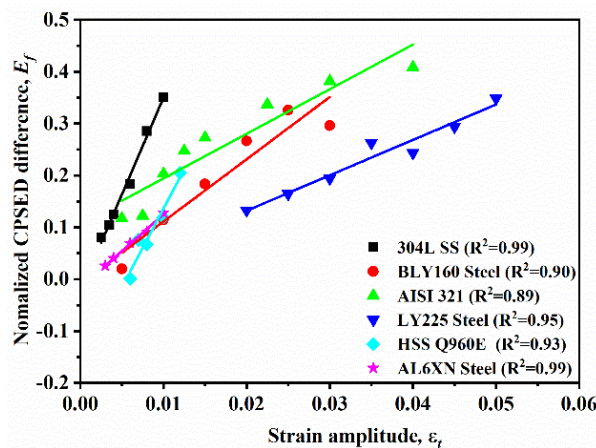


Figure 3.3 Variation of E_f with strain amplitude for different materials.

The relationship (**Equation 2.8**) can be used to estimate the CPSED of non-Masing behavior by calculating E_m (**Equation 2.5**) and E_f (**Equation 2.7**) [7]. The CPSED for Masing behavior (E_m) can be obtained by using the **Equation 2.2** [45]: The K and n are cyclic strength coefficient and exponent respectively, which can be obtained by Ramberg-Osgood (RO) stress-strain relationship (**Equation 2.3**) [155]. The estimated value of K and n for different materials are given in **Table 3.1**. As E_f (**Equation 2.7**) is a function of total strain amplitude (ε_t) and, to make **Equation 2.2** a function of the same, a relationship between the plastic strain range ($\Delta\varepsilon_p$) and total strain range ($\Delta\varepsilon_t$) was established for different materials (**Figure 3.4(a)**) and was found to be linear (similar to **Equation 2.4**) as well. Where S_1 and S_2 are the material constants and are given in **Table 3.1**. When $\Delta\varepsilon_p = 0$, $-S_2/S_1$ gives an estimate of the elastic strain corresponding to the linear portion of the hysteresis loops. The normalized CPSED difference (E_f) and CPSED for Masing behavior (E_m) depend only on the strain amplitude which can be obtained from the limited number of tests. Once we get the value of E_f and E_m , CPSED can be estimated from **Equation 2.8** for any strain amplitude.

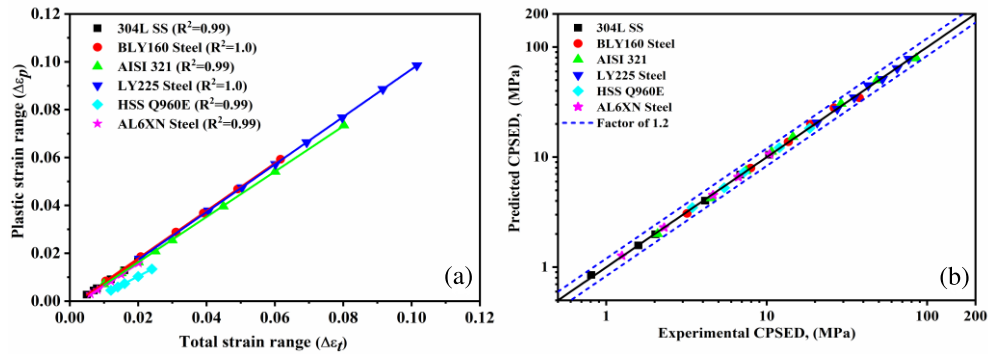


Figure 3.4 (a) Variation of plastic strain range with total strain range (b) comparison of predicted and experimental CPSED for six different materials.

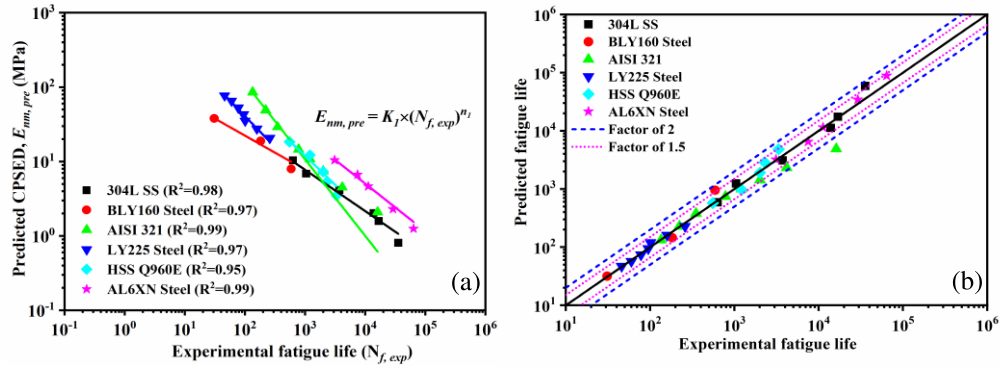


Figure 3.5 (a) Variation of predicted CPSED with number of cycles to failure (b) comparison of the experimental and predicted fatigue life for different materials.

The CPSED was predicted for all materials and was found to be within a scatter band of 1.2 as shown in **Figure 3.4(b)**. After estimation of CPSED, a power-law relationship [3] between the predicted CPSED and experimental fatigue life was established as shown in **Figure 3.5(a)**. The power-law relation can be expressed (**Equation 2.11**) as mentioned in **Chapter 2**. Where K_1 and n_1 are power-law constants and are given in **Table 3.1**. The parameters n_1 and K_1 represent the slope and intercept, respectively, of the predicted CPSED ($E_{nm,pre}$) and experimental fatigue life ($N_{f,exp}$) plot on a log-log scale. The accuracy of the fatigue life prediction depends on these parameters. Fatigue lives were estimated by using **Equation 2.12**, and it is found that the proposed model could predict the fatigue life within a scatter band of 2 as shown in **Figure 3.5(b)**.

Table 3.1 The various constants estimated for the different materials

Material	Reference	Constants of Equation 2.9 [S_3, S_4]	Constants of Equation 2.3 [K, n]	Constants of Equation 2.4 [S_1, S_2]	Constants of Equation 2.11 [K_1, n_1]
304L SS	Tested material	37.29, -0.023	1238.0, 0.177	0.9374, -0.0020	357.35, -0.554
BLY160 Steel	Xu et al. [8]	12.00, -0.009	581.09, 0.072	0.9943, -0.0020	183.63, -0.458
AISI 321 SS	Fumfera et al. [6]	5.60, -0.108	3679.4, 0.37	0.9469, -0.0027	13065, -1.028
LY225 Steel	Shi et al. [5]	6.83, -0.004	766.46, 0.092	0.9948, -0.0026	1895.9, -0.833
HSS Q960E	Bai et al. [91]	30.20, -0.166	8601.6, 0.322	0.7435, -0.0045	2577.5, -0.778
AL6XN Steel	Kalhaus and Jiang [157]	14.19, -0.017	1759.0, 0.181	0.9226, -0.0027	1830.8, -0.639

3.4 Summary and conclusions

In the present study, the new model of CPSED and fatigue life prediction has been validated with different materials of Type-I and Type-II non-Masing behavior. Type-I represents the behavior when the master curve can be constructed, and Type-II is when the master curve cannot be constructed by translating the hysteresis loops of the materials. Further, the following conclusions can be drawn based on the current investigation.

1. The model can also be used for the estimation of CPSED for the Masing behavior of materials, as the normalized CPSED difference parameter, which estimates the degree of non-Masing response, will be zero in that case. Thus, the proposed model is universally applicable to both Masing and non-Masing types of material behavior.
2. The model could successfully estimate the CPSED and fatigue life of all materials within a scatter band of 1.2 and 2, respectively.

3.5 Some highlights and remarks

Some highlights of the chapter:

- The proposed model of CPSED and fatigue life prediction has been validated with six more materials consisting of Type-I and Type-II non-Masing behavior. It could predict CPSED and fatigue life within the scatter bands of 1.5 and 2, respectively.
- Normalized CPSED difference indicates the extent of non-Masing, and it varies linearly with strain amplitude for different materials. Thus, it can be used to quantify the non-Masing behavior of materials irrespective of the construction of the master curve.

Remarks:

In this chapter, the proposed model of CPSED and fatigue life prediction has been validated with six materials consisting of Type-I and Type-II non-Masing behavior. The microstructural aspects of Type-I and Type-II non-Masing behavior will be investigated in the next chapter.



Chapter – 4

4. Microstructural Investigation

This chapter includes the results of a journal article [158] published in the International Journal of Fatigue (volume: 175 and pages: 107789). The details of the article are given below. Some additional contents are also included, which could not be presented in the article.

Type-I to Type-II non-Masing behavior of 304L SS under low cycle fatigue: material's internal changes

Sanjeev Singh Yadav^{*a}, Samir Chandra Roy^{*a}, J. Veerababu^b and Sunil Goyal^c

^aDepartment of Mechanical Engineering, Indian Institute of Technology Ropar, Rupnagar, Punjab 140001, India

^bMechanical Metallurgy Division, Indira Gandhi Centre for Atomic Research, Kalpakkam, Tamil Nadu 603102, India

^cNuclear Fuel Complex, Kota Project, Rawatbhata, Rajasthan 323303, India

*Corresponding authors' email ids: 2018mez0004@iitrpr.ac.in (S. S. Yadav), scroy@iitrpr.ac.in (S. C. Roy)

Corresponding authors' address: Material Behavior Research Laboratory, Department of Mechanical Engineering, Indian Institute of Technology Ropar, Rupnagar, Punjab 140001, India

Abstract

This study investigates the Type-I and Type-II non-Masing behavior of 304L austenitic stainless-steel fatigue tested at room temperature for strain amplitudes ranging from $\pm 0.25\%$ to $\pm 1.0\%$ at a strain rate of $1 \times 10^{-3} \text{ s}^{-1}$. The material exhibited Type-I non-Masing behavior at lower life fractions ($\leq 10\%$) and Type-II non-Masing behavior at higher life fractions ($> 10\%$). Type-I indicates that the master curve construction is possible, but in Type-II, the master curve can not be constructed. Further, low cycle fatigue tests conducted at $\pm 0.25\%$, $\pm 0.6\%$, and $\pm 1.0\%$ of strain amplitude were interrupted at life fractions of 8%, 30%, and 50% to investigate the internal material changes. At $\pm 0.6\%$ and $\pm 1.0\%$ of strain amplitude, the martensite content, dislocation density, and local misorientation increased with increasing life fraction, whereas the twins fraction decreased. Low martensite content and internal defects observed at low life fraction (8%) cause a minimal change in the strain-hardening rate behavior at different strain amplitudes, thereby, the Type-I non-Masing behavior. However, at higher life fractions (30% and 50%), high martensite content, high dislocation density, stacking faults, deformation twins, shear bands, dislocation walls, and cells have caused a significant change in the strain-hardening rate behavior, and thus, the Type-II non-Masing behavior.

Keywords: Low cycle fatigue; Masing/non-Masing behavior; Material characterization; Martensite; Strain hardening.

4.1 Introduction

Materials exhibit Masing/non-Masing behavior under fatigue loading depending upon the initial microstructural state, loading condition, strain amplitude, and stacking fault energy [16,29]. For Masing behavior, the loading branches of the hysteresis loops follow the same path irrespective of strain amplitude; however, it is not the case for non-Masing behavior [16]. Further, Yadav et al. [7,19] have classified the non-Masing behavior into two categories based on the possibility of master curve construction; in Type-I, the master curve can be constructed, while in Type-II, the master curve can not be constructed. The method of construction of the master curve has been explained in the review article [4]. Although the classification of non-Masing behavior into Type-I and Type-II is done based on the possibility of master curve construction, the internal structure of the material may exhibit some characteristic differences.

Numerous studies have been conducted to understand the microstructural characteristics of non-Masing behavior. Plumtree and Abdel-Raouf [15] have correlated the non-Masing behavior of materials with high dislocation density and cellular structure. In the case of 304LN SS, Sivaprasad et al. [30] observed that non-Masing behavior is related to martensite formation and unstable dislocation substructure. In 316L SS, Pham et al. [14] have found that the microstructure evolves from a planar dislocation structure into a lamella-like structure and finally forms the cellular structures during strain-controlled cyclic loading at room temperature. Such cellular structures presumably lead to the non-Masing behavior [15]. In Sanicro 25 alloy at 700°C, Li et al. [50] observed a nonuniform dislocation structure, causing the deviation from the Masing behavior. All the microstructural investigations reported in the literature are primarily related to the Type-I non-Masing behavior. As the Type-II non-Masing behavior has not been reported earlier, until by Yadav et al. [7] in 2021, no data or information related to the internal material/microstructural changes is available in the open literature.

Although other researchers have not identified the Type-II non-Masing behavior, the analysis of the published data in the open literature suggests that several materials like- 304L SS [19], BLY160 steel [8], and 321 SS [6] exhibit Type-II non-Masing behavior, as reported in [19]. Thus, it is important to investigate the internal/microstructural changes a material may undergo while exhibiting Type-II non-Masing behavior. As reported in [4], a material that exhibits Masing behavior under a specific testing condition can also exhibit non-Masing if the testing condition or parameters are varied. For example, 316LN SS, used as a structural material in nuclear power plants, exhibits the Masing behavior at room temperature, whereas the behavior is non-Masing at 600°C [28]. Literature also suggests that many materials change their behavior between Masing and non-Masing depending upon the strain amplitude [94,95]. The current investigation shows that a material can also change its behavior from Type-I to Type-II

non-Masing with varying life fractions, as will be discussed in **Section 4.3.2**. The microstructural changes expected during fatigue loading are studied by conducting interrupted LCF tests.

4.2 Experimental details

4.2.1 Material and specimen

The details of material and specimen are given in **Section 2.2**.

4.2.2 LCF testing

The fully-reversed LCF tests at room temperature were conducted at various strain amplitudes ranging from $\pm 0.25\%$ to $\pm 1.0\%$ at a strain rate of $1 \times 10^{-3} \text{ s}^{-1}$ on 304L SS under strain-controlled mode using a triangular waveform. Initially, the tests were continued until the specimens failed (data are shown in **Figure 4.1(a)**). Further, to understand the material's internal/microstructural changes, additional LCF tests conducted at $\pm 0.25\%$, $\pm 0.6\%$, and $\pm 1.0\%$ of strain amplitudes were interrupted at 8%, 30%, and 50% of life fractions.

4.2.3 Microstructural characterization

Transmission electron microscopic investigations were carried out using a 300 kV FEI Tecnai TEM, and a 200 kV Philips CM200 TEM. After the interrupted test, the TEM sample slices of 0.5 mm thickness were extracted from the center of the gage section using a low-speed precision diamond cutter. The mechanical thinning at low revolutions per minute (RPM) was done using the standard metallography technique up to a thickness of 100 μm . The rule of thumb for mechanical thinning is that the abrasive particle produces damage to the surface region of three times the grit size. Hence, for the thinning, the samples were polished with 3M emery paper of grit size number ranging from 220 to 2500. After that, the samples of 0.3 mm diameter were punched out, and the slow-speed dimpling process was carried out to reduce the thickness of the sample from 100 μm to a few microns. This follows ion milling with a 3 keV energy Ar⁺ beam at a 5° incident angle until electron transparency (50 nm or less) is obtained. After ion milling, the samples were cleaned using plasma cleaner and dried carefully before examination in the TEM. The electron backscatter diffraction (EBSD) investigation has also been performed to measure local misorientation that occurs due to cyclic plastic deformation. For EBSD analysis, the area (830×620 μm^2) in the uniform deformation zone of each specimen was analyzed.

The ZEISS, Germany (model: Carl Sigma 500) scanning electron microscope was used for EBSD characterization, and the acquired data were evaluated by orientation imaging

microscopy (OIM) software. The EBSD maps were collected using a step size of 0.5 μm at an operating voltage of 20 kV. The low-angle grain boundaries (LAGBs) are indicated by two different colors, green (1° to 5°) and blue ($>5^\circ$ to 15°). However, the high-angle grain boundaries (HAGBs) are indicated by red color ($>15^\circ$). The kernel average misorientation (KAM) is measured to evaluate the local misorientations ($<5^\circ$). The EBSD samples were extracted from the center of the gage section using a precision diamond cutter. The samples were prepared using the standard metallography techniques for obtaining a high-quality Kikuchi pattern. The image quality (IQ) map is a quantitative indicator of the presence of defects, and inverse pole figures (IPF) represent the grain orientation with respect to the crystal axis.

A ferritescope (FERITSCOPE FMP30, Fischer) was used to quantify the deformation-induced martensite formed during LCF tests. The ferrite number readings were taken at the midpoint and 10 mm from the midpoint. After that, the ferrite number was converted to the martensite content (% mass) by Talonen's correlation [150], which states that the amount of martensite content (% mass) is $= 1.7 \times \text{ferrite number}$.

4.3 Results

4.3.1 Cyclic stress response (CSR)

All the cyclic stress response (CSR) curves obtained from the full-life (solid lines) and interrupted (lines with symbols) tests have been plotted together in **Figure 4.1(a)**, which highlights excellent repeatability and consistent material response with cycling. The CSR curves show the material's hardening, softening, saturation, and secondary hardening behavior depending on the strain amplitudes, as shown in **Figure 4.1(a)**. In 304L SS, the initial hardening is associated with interactions of dislocation with other dislocations/defects, and softening is associated with cell/channel structures and annihilation of the dislocations [12]. It is observed that the secondary hardening at high strain amplitude occurs due to martensitic transformation.

Figure 4.1(b) shows the mass fraction of the deformation-induced martensite (DIM) formed in the interrupted test specimen, measured using the ferritescope, as mentioned in **Section 4.2.3**. The martensitic transformation of austenite requires a critical activation energy. In the absence of the necessary thermal activation, during fatigue of 304L SS at room temperature, the activation energy needed for the phase transformation would come from the strain energy supplied to the material [159]. It is interesting to note that at the lower life fraction (8%), the fraction of deformation-induced martensite (DIM) does not change with strain amplitude; however, it increases with strain amplitude at the other two life fractions (30% and 50%). Moreover, at the lowest strain amplitude ($\pm 0.25\%$), there is a very less amount of

martensite formation throughout the fatigue life. The ferritescope investigation of the undeformed or untested specimens did not show the presence of any martensite content. As martensitic transformation does not occur at the low life fraction (8%), less microstructural heterogeneity is believed to occur. This has contributed to the Type-I non-Masing behavior of the material at life fractions below 10%. The increased amount of martensite formation at higher life fractions and high strain amplitudes causes significant microstructural heterogeneities, thereby, the Type-II non-Masing behavior. Although the above results highlight the role of deformation-induced martensitic transformation on the non-Masing behavior, a detailed investigation of the material's internal change was conducted to get a clear picture, as explained in Sections 4.3.3 and 4.3.4.

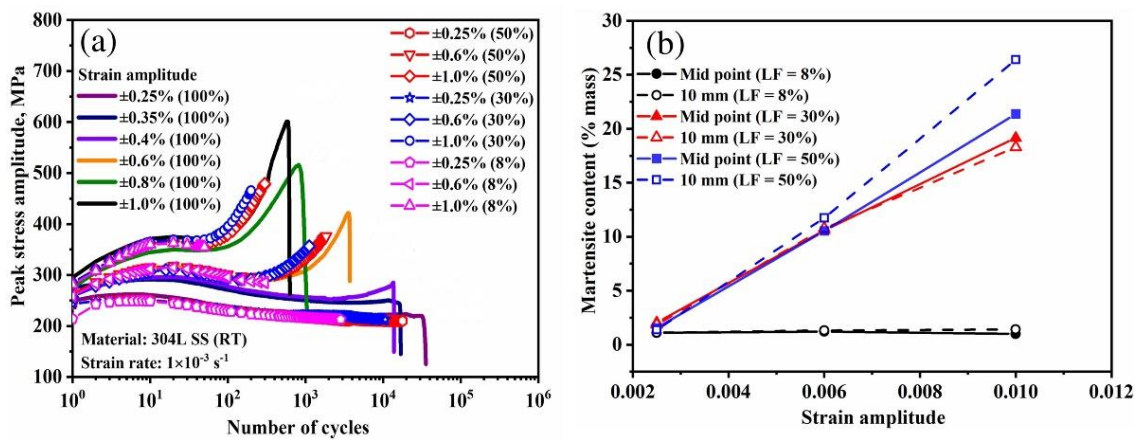


Figure 4.1 (a) Peak stress variation with the number of cycles obtained from the full-life (100%) and interrupted (8%, 30%, and 50% of life fractions) LCF tests. The solid lines indicate the full-life tests performed until specimen failure, and the lines with symbols indicate the interrupted LCF tests. (b) variation of martensite content with strain amplitudes at different locations (midpoint and 10 mm away from midpoint) of the specimens for different life fractions. Note: LF = life fraction.

4.3.2 Analysis of non-Masing behavior

The Masing/non-Masing behavior of a material is analyzed by plotting together the stabilized (or half-life) hysteresis loops obtained from fatigue tests conducted at different strain amplitudes. For Masing behavior, the hysteresis loops follow the same loading path when plotted with a common compressive tip by translating them without any rotation. While for non-Masing behavior, the hysteresis loops do not follow the same loading path. The state-of-the-art techniques/methods available for the analysis of Masing/non-Masing behavior are discussed in detail in the article [4]. In the literature, the Masing/non-Masing behavior is mostly investigated by analyzing the stabilized or half-life hysteresis loops. To the best of our

knowledge, no article has investigated the evolution of material's Masing/non-Masing behavior with cycling or different life fractions. Hence, an effort is made to analyze the Masing/non-Masing behavior of the material with varying life fractions. The 304L SS material is found to exhibit only non-Masing behavior at different life fractions. In **Figure 4.2**, an effort was made to analyze the non-Masing behavior by constructing the master curve by translating the hysteresis loops to match the loading branches along with their linear elastic portions.

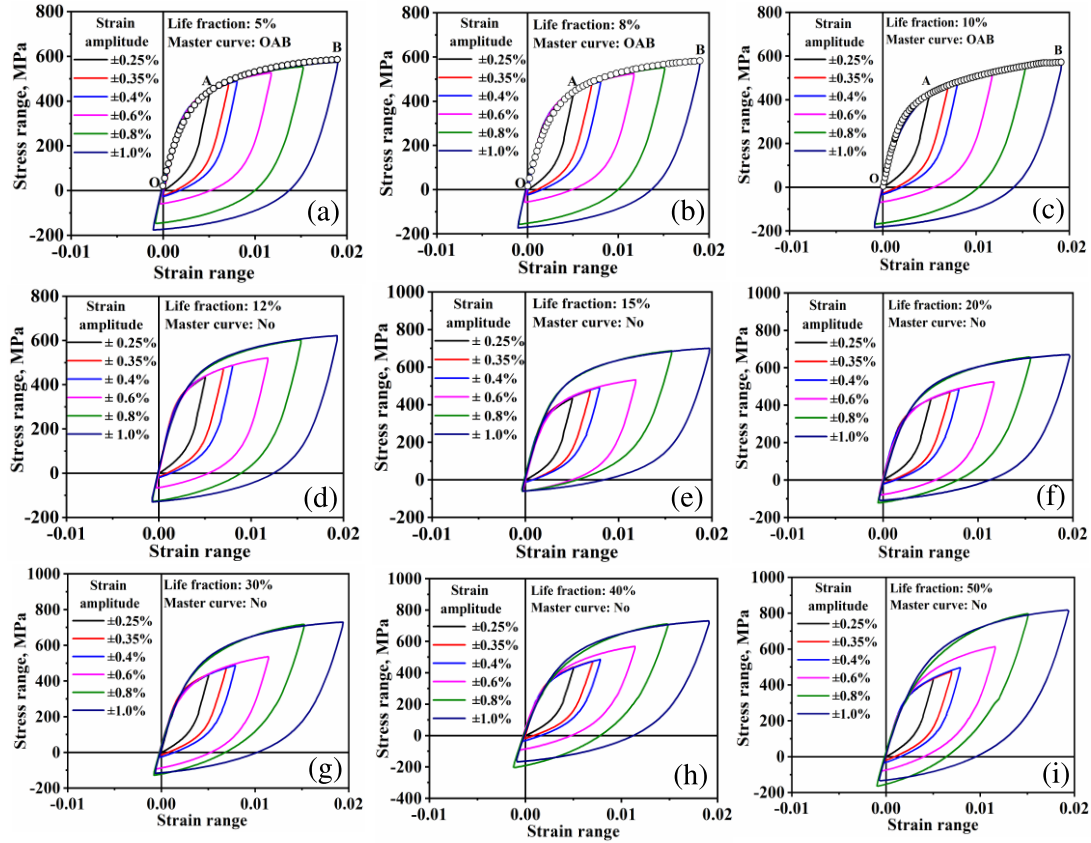


Figure 4.2 Construction of master curve for different life fractions (a) 5%, (b) 8%, (c) 10%, (d) 12%, (e) 15%, (f) 20%, (g) 30%, (h) 40%, and (i) 50%.

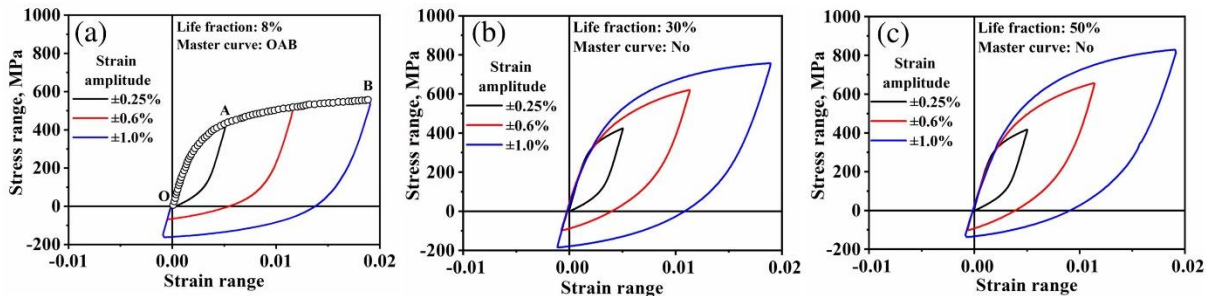


Figure 4.3 Construction of master curve from the interrupted test data. Tests were conducted for life fractions of (a) 8% (Type-I), (b) 30% (Type-II), and (c) 50% (Type-II).

As can be seen in **Figure 4.2(a-c)**, the construction of a master curve was possible at life fractions of 5%, 8%, and 10%, while the master curve could not be constructed (**Figure 4.2(d-i)**) for 12%, 15%, 20%, 30%, 40% and 50% of life fractions. Thus, according to the classification of non-Masing behavior proposed by Yadav et al. [7], the material 304L SS can be said to have exhibited non-Masing behavior of Type-I up to 10% (approximately) of fatigue life, whereas Type-II non-Masing behavior beyond the 10% of fatigue life. Such a change in the material behavior from Type-I to Type-II non-Masing indicates that there can be some characteristic variation in the material's internal state or response with cycling. Hence, interrupted LCF tests were performed at $\pm 0.25\%$, $\pm 0.6\%$, and $\pm 1.0\%$ of strain amplitudes for 8%, 30%, and 50% of life fractions, and detailed microstructural investigations were done, as discussed in **Sections 4.3.3** and **4.3.4**. It should be noted that the analysis of the hysteresis loops of the interrupted tests also shows a similar variation of the non-Masing behavior from Type-I to Type-II, as shown in **Figure 4.3**. Thus, it can be concluded that a material can change its Masing/non-Masing behavior with cycling or life fraction.

4.3.3 Localized deformation analysis

Figure 4.4 shows the image quality (IQ) map, kernel average misorientation (KAM) map, and inverse pole figure (IPF) obtained from the untested specimen using the EBSD technique. A large fraction of annealing twins is observed in **Figure 4.4(a)**. The KAM map (**Figure 4.4(b)**) highlights no local deformation in the untested sample, and the IPF map (**Figure 4.4(c)**) shows a random grain orientation.

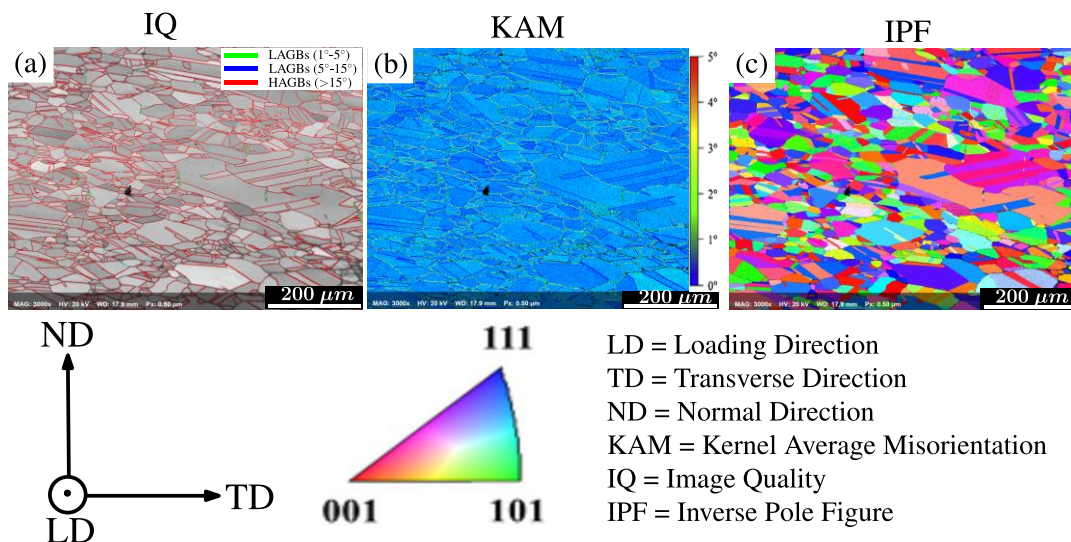


Figure 4.4 Representation of the (a) image quality (IQ) map, (b) kernel average misorientation (KAM) map, and (c) inverse pole figure (IPF) of the untested sample.

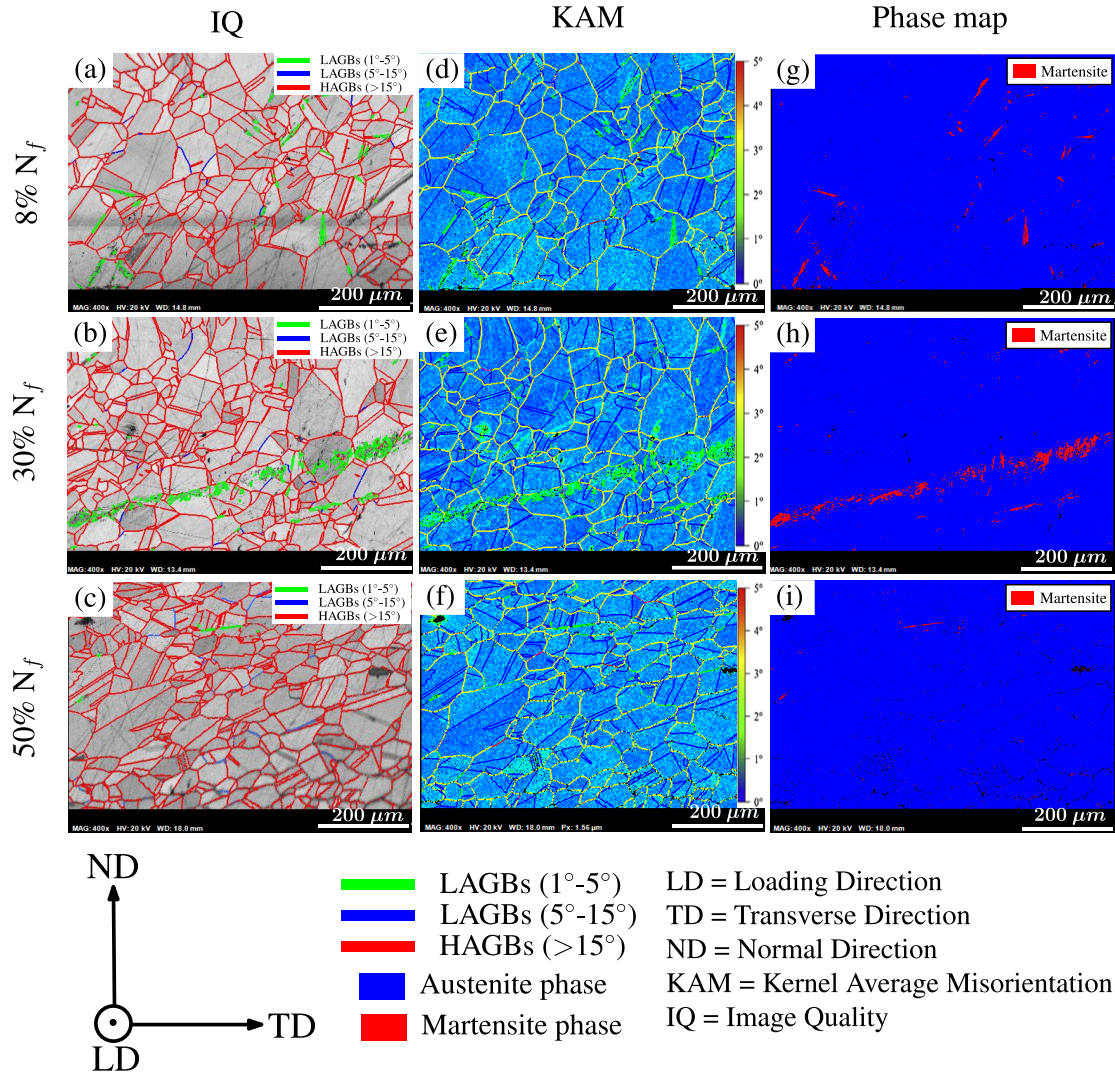


Figure 4.5 Representation of (a-c) image quality maps, (d-f) kernel average misorientation maps, and (g-i) phase maps at different life fractions at the strain amplitude of $\pm 0.25\%$.

The variation of the fraction of LAGBs, twin fraction, martensite fraction, and KAM for various life fractions at different strain amplitudes are given in **Table 4.1**. At a relatively lower strain amplitude ($\pm 0.25\%$), the number of LAGBs does not change (**Table 4.1**) with life fraction because of the less generation of dislocation in various grains (**Figure 4.5(a-c)**). The local deformation (KAM value) increases slightly with life fractions at the strain amplitude of $\pm 0.25\%$, as given in **Table 4.1**. In KAM maps, a few green regions around the grain boundaries (GBs) are attributed to the pile-up of dislocations near the GBs, **Figure 4.5(d-f)**. The amount of martensite does not change significantly with life fractions, **Figure 4.5(g-i)**. Low martensite content ($<2.5\%$) has been observed for different life fractions due to less plastic strain than the critical plastic strain amplitude (0.3%) required for martensitic transformation. The quantitative values of martensite content (obtained by EBSD) at different life fractions for different strain amplitudes are given in **Table 4.1**. There is very minimal change in the microstructural features

such as dislocation density, the fraction of LAGBs, and martensite content with life fraction at $\pm 0.25\%$ of strain amplitude.

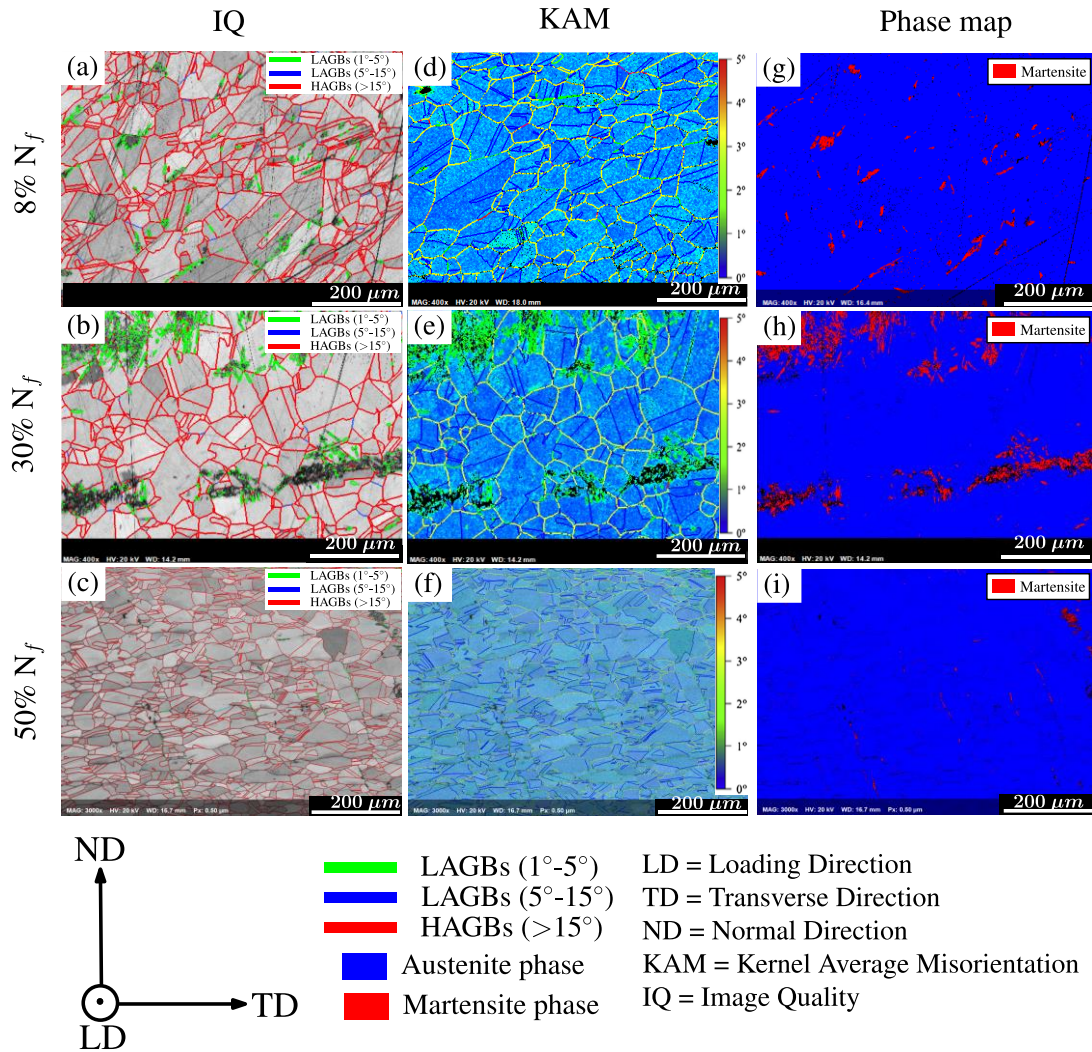


Figure 4.6 Representation of (a-c) image quality maps, (d-f) kernel average misorientation maps, and (g-i) phase maps at different life fractions at the strain amplitude of $\pm 0.6\%$.

For strain amplitude of $\pm 0.6\%$, the black color in the IQ micrographs indicates the high deformation regions due to plastic strain accumulation [27], which is also visible at the same location in the KAM and phase maps (Figure 4.6). Also, the LAGBs do not change significantly with life fractions (Table 4.1), as shown in IQ maps (Figure 4.6(a-c)). It is well established that the GBs act as a sink for the accumulation of defects, mainly dislocations. The area of the green region in the KAM maps (Figure 4.6(d-f)) increases with life fractions, indicating increased local deformation with life fractions (Table 4.1) than the former one ($\pm 0.25\%$). The martensite content increases with life fractions up to 30% (Figure 4.6(g, h)); however, the martensite formation detected by EBSD for 50% of life fraction (Figure 4.6(i)) has been less, which could be due to the localized nature of EBSD investigation. A higher amount of

martensite formation at 50% of life fraction can be assured from the ferritescope measurement shown in **Figure 4.1(b)**.

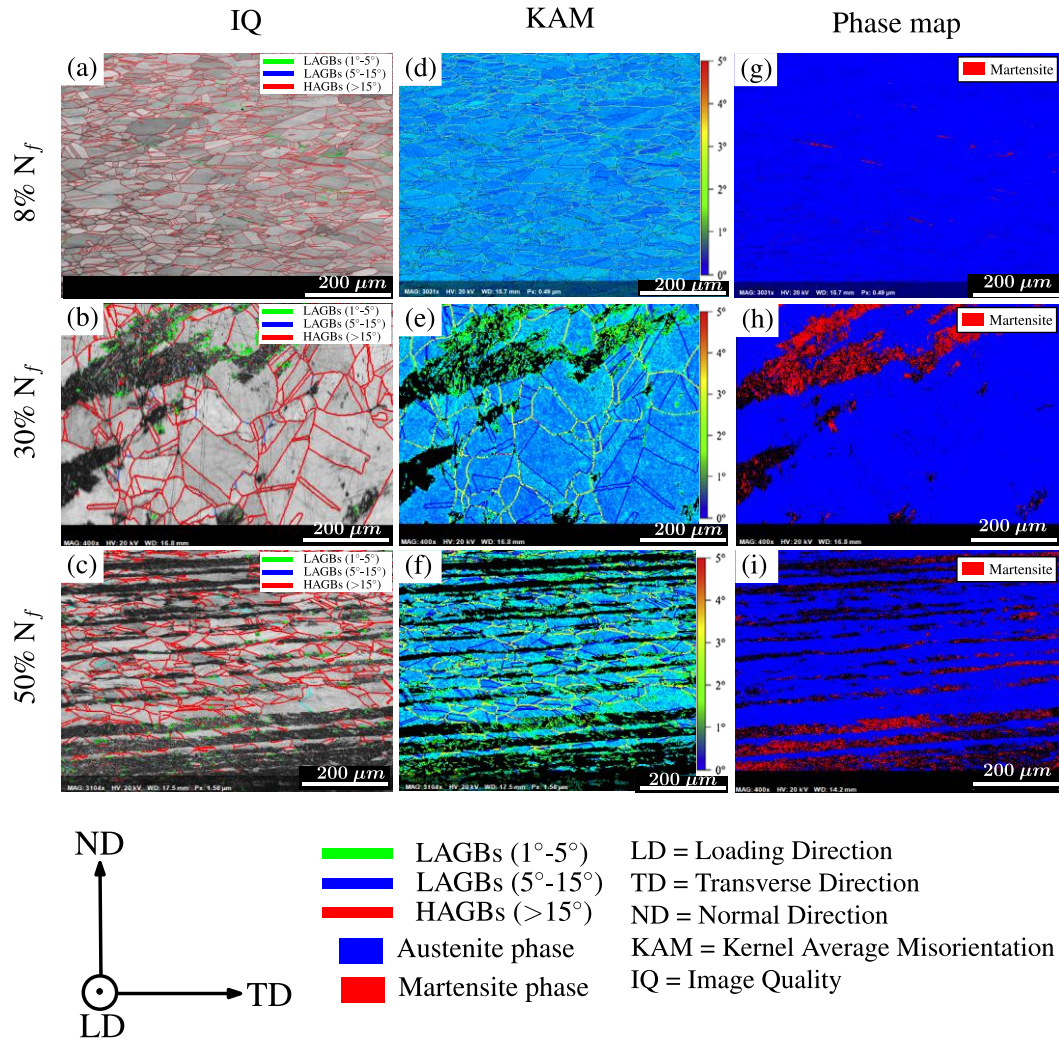


Figure 4.7 Representation of (a-c) image quality maps, (d-f) kernel average misorientation maps, and (g-i) phase maps at different life fractions at the strain amplitude of $\pm 1.0\%$.

For strain amplitude of $\pm 1.0\%$, the black color in the IQ maps (**Figure 4.7(a-c)**), especially at high life fraction, indicates the very high local heterogeneity (**Table 4.1**) during the deformation. The KAM maps (**Figure 4.7(d-f)**) show that the green region increases significantly, and the yellow region also occurs at some places at high life fraction (50%), indicating a remarkably high dislocation density compared to lower life fractions. Further, the deformation heterogeneity also exists within the individual grain at high life fraction of 50%. Similar to previous observations, the local misorientation increases with life fractions (**Table 4.1**), and the maximum value of local misorientation is found near the GBs for all samples owing to the dislocation pile-up (**Figure 4.7(d-f)**). The higher value of KAM indicates the development of local strain attributed to the accumulation of dislocations, the presence of

martensite, and high dislocation density [160]. The amount of martensite increases with life fraction (**Figure 4.7(g-i)** and **Table 4.1**) due to the high probability of nucleation sites, i.e., intersections between the defects like shear bands, twins, and GBs, for martensitic transformations at high life fraction. The quantitative values of the fraction of LAGBs, KAM, twin fraction, and martensite content for different strain amplitudes at different life fractions are given in **Table 4.1**.

Table 4.1 Variation of the fraction of LAGBs, twin fraction, martensite fraction, and average KAM for various life fractions at different strain amplitudes.

Sample description		Fraction of LAGBs	Twin fraction	Martensite phase fraction	Average KAM value
Life fraction	Strain amplitude				
8%	$\pm 0.25\%$	0.02123	0.319	1.04	0.70
	$\pm 0.6\%$	0.03272	0.337	1.88	0.774
	$\pm 1.0\%$	0.02617	0.209	0.556	0.796
30%	$\pm 0.25\%$	0.02131	0.317	2.21	0.718
	$\pm 0.6\%$	0.03405	0.178	7.07	0.780
	$\pm 1.0\%$	0.05036	0.179	8.63	0.928
50%	$\pm 0.25\%$	0.03256	0.331	0.31	0.774
	$\pm 0.6\%$	0.02589	0.206	0.85	0.784
	$\pm 1.0\%$	0.03083	0.106	13.1	1.227

4.3.4 Substructural analysis

The TEM investigations have been carried out at different life fractions and strain amplitudes to identify the material's internal state variables, such as dislocation tangles, stacking faults, deformation twins, dislocation cells, shear bands, martensite, etc., responsible for Type-I and Type-II non-Masing behavior. The TEM investigation reveals interesting information about the deformation behavior of 304L SS under LCF. Several TEM micrographs for a specimen have been obtained and analyzed before and after the interrupted tests. **Figure 4.8(a, b)** show the significantly low dislocation density at different regions of the base (untested) samples that were solution annealed.

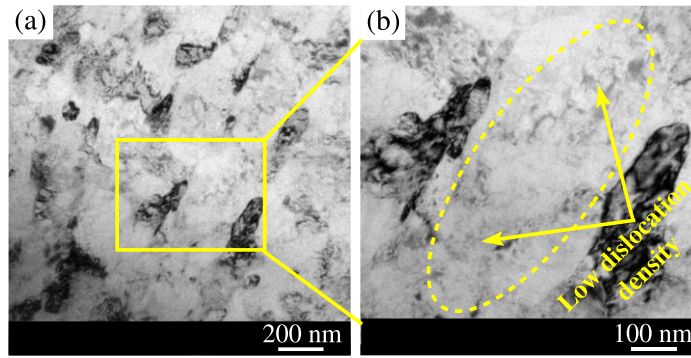


Figure 4.8 TEM images of an untested sample of 304L SS showing the (a) low dislocation density, (b) magnified view of the highlighted region in image (a).

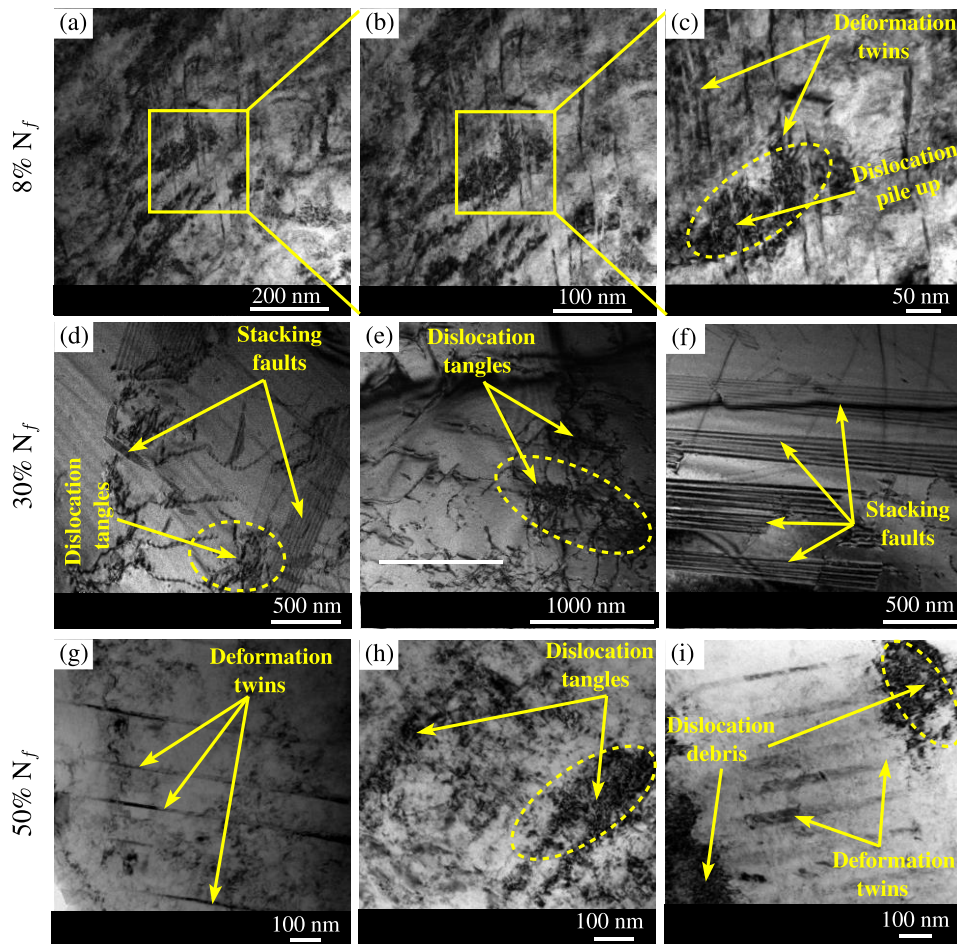


Figure 4.9 TEM images showing the internal state of 304L SS at life fractions of (a-c) 8%, (d-f) 30%, and (g-i) 50%, fatigue tested at the strain amplitude of $\pm 0.25\%$.

For low strain amplitude of $\pm 0.25\%$, the generation of dislocations, dislocation pile up, formation of some dislocations tangles, and the interaction of dislocations with twin boundaries (TBs) have been observed at the life fraction of 8%, **Figure 4.9(a-c)**. The TBs provide barriers to the dislocation motion, leading to dislocations piling up near the TBs and subsequent formation of dislocation tangles, **Figure 4.9(c)**. The stacking faults (SFs) and dislocation

tangles dominate the deformation behavior at 30% life fraction, **Figure 4.9(d-f)**. However, as the number of cycles increases, these SFs may transform into DTs when the SFs overlap on successive (111) planes [161]. Therefore, a large number of DTs have been observed in addition to dislocation tangles and dislocation debris at the life fraction of 50%, **Figure 4.9(g-i)**.

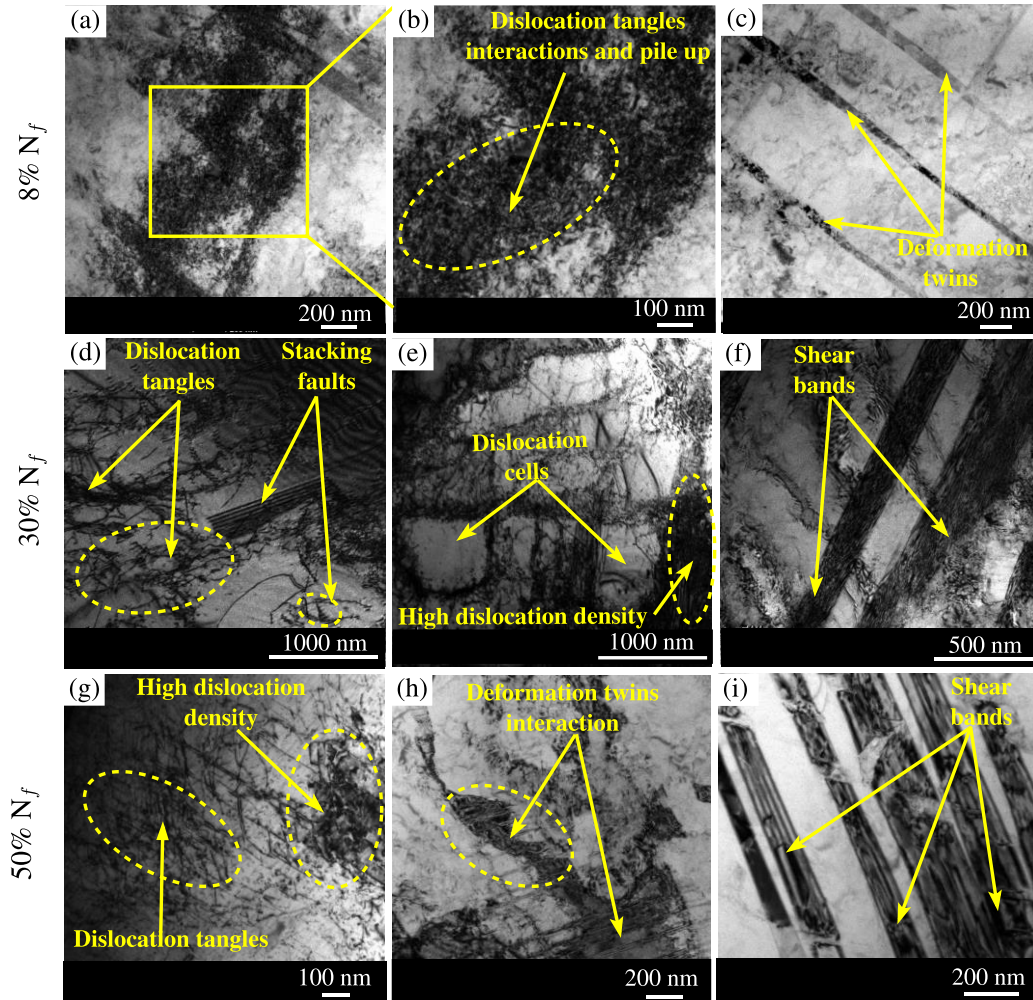


Figure 4.10 TEM images showing the internal state of 304L SS at life fractions of (a-c) 8%, (d-f) 30%, and (g-i) 50%, fatigue tested at the strain amplitude of $\pm 0.6\%$.

At $\pm 0.6\%$ of strain amplitude (**Figure 4.10**), the dislocation tangles, SFs, and shear bands dominate the deformation behavior at the life fraction of 30%; however, some dislocation cell formation has also been observed. A similar kind of cell formation has been observed by Das et al. [152] in 304LN SS. No cell formation is observed at the lower life fraction (8%); however, the formation of dislocation tangles is observed, as shown in **Figure 4.10(a-c)**, which is in line with the observation of Wang et al. [162] for the same material (304L SS) after the interrupted testing. The formation of dislocation cells is related to the rearrangement of dislocations into low-energy configurations with cycling. The dislocation cell walls and interior regions are of high and low dislocation densities, respectively, **Figure 4.10(e)**. Some shear bands have also

been observed at the life fraction of the 30%, as shown in **Figure 4.10(f)**. At the high life fraction of 50%, a large number of dislocations (**Figure 4.10(g)**), interactions between the dislocations and DTs (**Figure 4.10(h)**), and shear bands (**Figure 4.10(i)**) have been observed. Shear bands may consist of twins (SFs overlap on successive (111) planes), hcp-martensite (SFs overlap on alternate (111) planes), bundles of stacking faults (irregular overlapping of SFs), and slip bands [161].

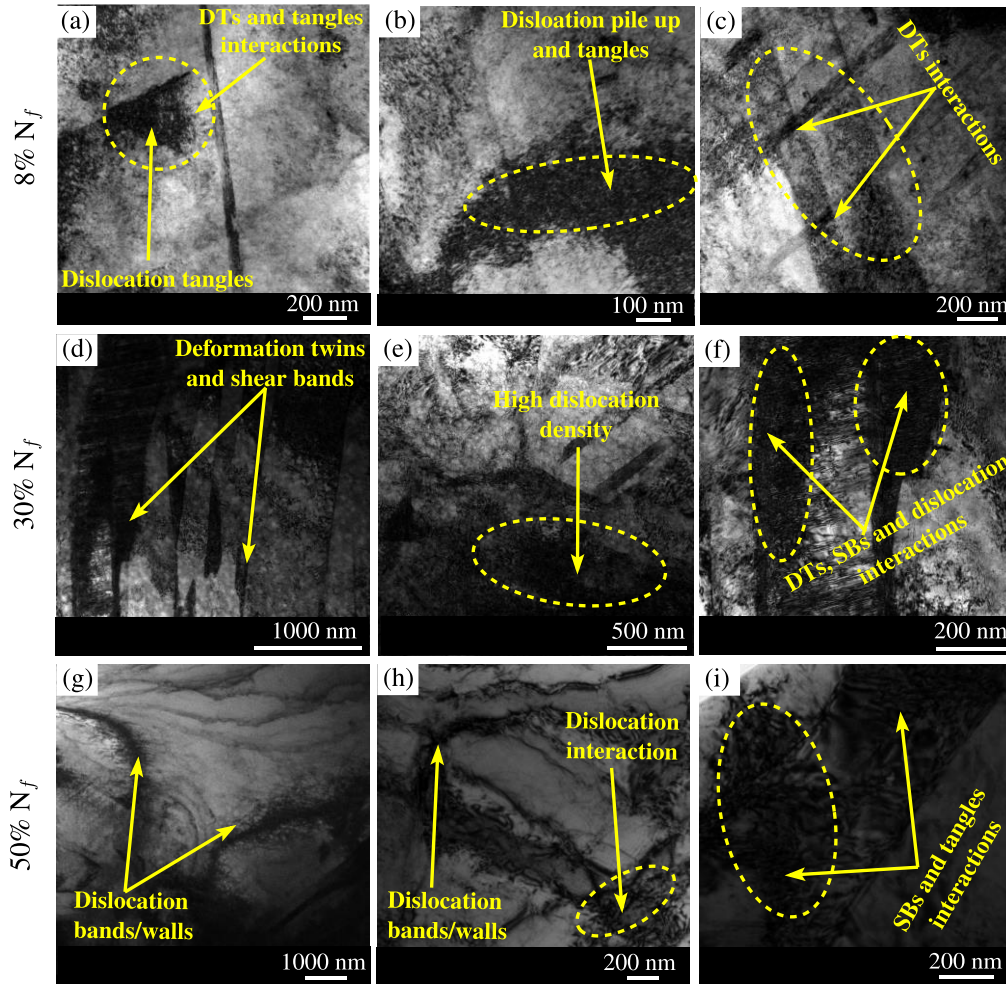


Figure 4.11 TEM images showing the internal state of 304L SS at life fractions of (a-c) 8%, (d-f) 30%, and (g-i) 50%, fatigue tested at the strain amplitude of $\pm 0.1\%$. Note: DT = deformation twins, SBs = shear bands.

At $\pm 1.0\%$ of strain amplitude, dislocation tangles, and DTs have been observed at 8% life fraction, **Figure 4.11(a-c)**. A large number of the shear bands (SBs), interactions among DTs, SBs, and dislocations have been observed at the life fraction of 30%, **Figure 4.11(d-f)**. The formation of the dislocation walls, interaction of dislocation with dislocations and shear bands have been observed at 50% of life fraction, as shown in **Figure 4.11(g-i)**. As the life fraction increases, the probability of interaction between the various defects, such as DTs and shear

bands increase, **Figure 4.11(f)**. Such interaction would cause the martensitic transformation, thereby reducing the population of DTs and shear bands. Interestingly, in the TEM investigation **Figure 4.11(g-i)**, significantly low DTs and shear bands have been observed at 50% of the life fraction compared to the lower life fraction.

Based on the TEM analysis, it can be concluded that the dislocations, dislocation tangles, and deformation twins have been observed at 8% of life fraction at all strain amplitudes. High fractions of SFs, DTs, SBs, and some dislocation cell formations have been observed at 30% of life fraction. As the life fraction increases to 50%, a high fraction of dislocation tangles, dislocation walls, high dislocation density, and some shear bands have been observed. The interaction between the different types of defects also increases with an increase in strain amplitude and life fraction. Hence, significant internal changes were observed at 30% and 50% of life fractions. Minimal change in the material's internal state at 8% life fraction might have led to Type-I non-Masing behavior, whereas significant heterogeneity in the material's internal state at higher life fractions (30% and 50%) might have led to Type-II non-Masing behavior.

4.4 Discussion

4.4.1 Influence of secondary hardening

The shape of the hysteresis loops and, subsequently, the Masing/non-Masing response is influenced by the initial hardening, softening, and secondary hardening behavior of 304L SS. Secondary hardening in 304L SS has been observed due to martensitic transformation at higher strain amplitudes ($>\pm 0.35\%$). The extent of secondary hardening increases with an increase in strain amplitude, as shown in **Figure 4.12(a)**. The dotted line in **Figure 4.12(a)** connects the data points at 10% of fatigue life for different strain amplitudes. Interestingly, the 10% of fatigue life indicates the onset of the secondary hardening region at different strain amplitudes (except $\pm 0.25\%$) and the transition of the non-Masing behavior from Type-I to Type-II as well. It is also evident from **Figure 4.1(b)**, as martensitic transformation does not occur at the low life fraction (8%), less microstructural heterogeneity and, subsequently, lesser secondary hardening behavior (**Figure 4.12(a)**) is believed to occur. This has contributed to the Type-I non-Masing behavior of the material at life fractions below 10%. The increased amount of martensite formation at higher life fractions and high strain amplitudes causes significant microstructural heterogeneities and, subsequently, higher secondary hardening behavior (**Figure 4.12(a)**), thereby, the Type-II non-Masing behavior.

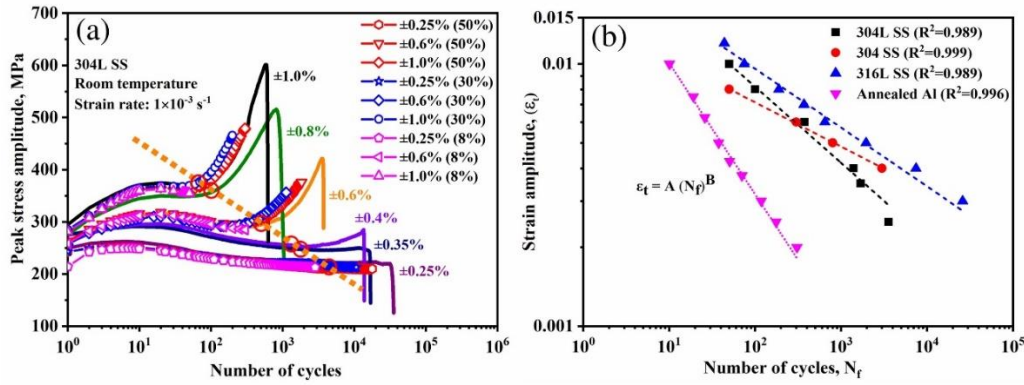


Figure 4.12 (a) Variation of peak stress with the number of cycles. The dotted line connects the data points at 10% of fatigue life for different strain amplitudes. (b) variation of the number of cycles at the onset of secondary hardening with strain amplitude.

In **Figure 4.12(b)**, the number of cycles at the onset of secondary hardening for 304L SS is plotted as a function of strain amplitude. This plot shows a linear behavior on a log-log scale. **Figure 4.12(b)** shows similar plots for three other materials for which the data were extracted from the published articles in the open platforms; 304 SS [163], 316L SS [164], and annealed Al [122]. For these three materials, the number of cycles at the onset of secondary hardening is considered for the plots, as the information regarding the transition from Type-I to Type-II non-Masing behavior is not known. It is interesting to note that the other three materials also exhibit a linear behavior on a log-log scale. Thus, a power law equation ($\epsilon_t = A(N_f)^B$) of Coffin-Manson [34,35] type seems to describe the behavior very well. The constants (A, B) of the proposed equation are (0.031, -0.29) for 304L SS, (0.016, -0.17) for 304 SS, (0.027, -0.22) for 316L SS and (0.032, -0.5) for annealed Al. From the plot in **Figure 4.12(b)**, the approximate number of cycles at which the transition from Type-I to Type-II non-Masing behavior would happen for 304L SS at other strain amplitude appears to be identifiable. For the other materials, the same would predict the onset of secondary hardening.

At lower strain amplitudes, close to the conventional elastic limit (*i.e.*, 0.2% plastic strain), the transition life can not be determined from **Figure 4.12(b)**, as secondary hardening is not observed due to an insufficient amount of martensitic transformation, shown in **Figure 4.12(a)**. It can also be observed that the onset of secondary hardening, associated with martensitic transformation, requires a large number of cycles at lower strain amplitude, whereas it requires less number of cycles at high strain amplitude, **Figure 4.12(b)**. Although **Figure 4.12(b)** shows a linear behavior on a log-log plot for the selected materials, further investigation with different materials would help in making a generalized conclusion.

4.4.2 Influence of martensite fraction

The influence of twinning on the martensitic transformation and the Masing/non-Masing behavior of 304L SS has been investigated and analyzed. Several annealing twins were observed in the untested sample (**Figure 4.4(a)**). At $\pm 0.25\%$ of strain amplitude (**Figure 4.13(a)**), initially up to 8% of the life fraction, the twin fraction increases due to the formation of the deformation twins during cycling. After that, the twin fraction does not change with cycling (**Figure 4.13(a)**) due to stabilized behavior of 304L SS (**Figure 4.1(a)**) and no martensitic transformation. Researchers [102,165] have found that the twins-twins intersection, twins-shear intersection, and the intersection of twins with other defects act as nucleation sites for martensitic transformation. Therefore, the twin fraction reduces as martensite transformation increases during the deformation at a particular strain amplitude. At $\pm 0.6\%$ and $\pm 1.0\%$ of strain amplitude (**Figure 4.13(a)**), the twin fraction decreases with cycling due to the interaction of the twins with other defects such as GBs, and deformation twins, ultimately leading to martensitic transformation [165]. Therefore, the martensite amount increases with life fractions, especially at the strain amplitudes of ± 0.6 and $\pm 1.0\%$, **Figure 4.13(b)**.

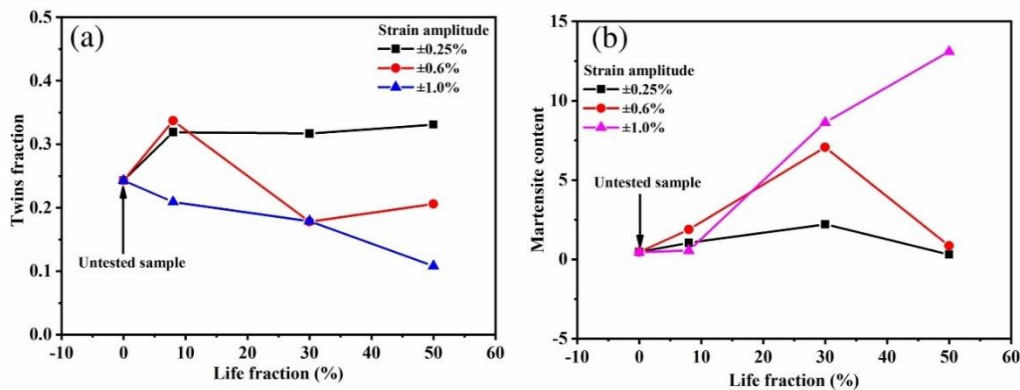


Figure 4.13 Variation of the (a) twin fraction and (b) martensite content (phase fraction) with life fraction at different strain amplitudes.

As can be seen in **Figure 4.13(b)**, the martensite content (measured by EBSD) does not change significantly with life fraction at the strain amplitude $\pm 0.25\%$. The martensite content is very low ($<2.0\%$) at the low life fraction of 8%, irrespective of strain amplitudes, **Figure 4.13(b)** and **Table 4.1**. Conversely, martensite content increases with life fraction at the strain amplitudes of $\pm 0.6\%$ and $\pm 1.0\%$, and it is in line with the ferritoscope results (**Figure 4.1(b)**). The high rate of martensitic transformation at high strain amplitude and life fraction leads to the creation/generation of additional dislocations and, subsequently, more heterogeneity in the material [54]. For 304L SS under cycling, the extent of microstructural heterogeneity is directly related to the amount of martensite fraction and other defects that form. Therefore, it can be

concluded that the low fraction of martensite leading to minimal microstructural instabilities/heterogeneities has contributed to the Type-I non-Masing behavior at life fractions below 10%. The high fraction of martensite formation at higher life fractions (beyond 10%) causes significant microstructural instabilities/heterogeneities, thereby, Type-II non-Masing behavior.

4.4.3 Influence of misorientation distribution

The distribution of KAM angle for the interrupted fatigue tests is shown in **Figure 4.14**. As seen in **Figure 4.14(a)**, the maximum occurred misorientation angle is almost the same at 8% life fraction for all strain amplitudes. The average KAM angle also does not change significantly with strain amplitude, given in **Table 4.1**. At higher life fractions (30% and 50%), the variation of the maximum occurred misorientation angle (**Figure 4.14(a)**), and the average KAM angle (**Table 4.1**) with strain amplitude is relatively high. This highlights the development of heterogeneities in the deformation behavior at higher life fractions, contributing to the non-Masing behavior. As the life fraction increases to 30% and 50%, the local deformation increases due to the generation of the various defects and the interaction between them.

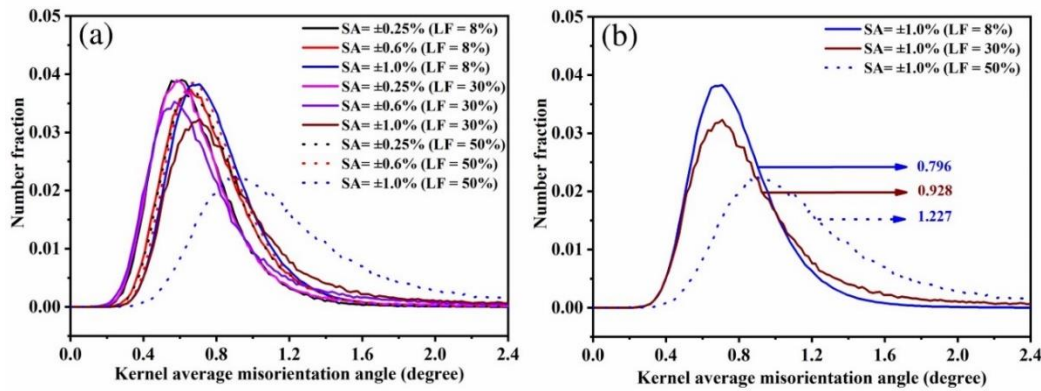


Figure 4.14 (a) KAM profile for different life fractions at various strain amplitudes (b) The average KAM value with life fraction at $\pm 1.0\%$ strain amplitude. Note: LF = life fraction, SA = strain amplitude.

At $\pm 1.0\%$ strain amplitude, the average KAM angle increases with life fraction due to an increase in local deformation at high life fraction, **Figure 4.14(b)**. The peak broadening at high strain amplitude ($\pm 1.0\%$) indicates that the local deformation is spread over a range with comparatively higher misorientation angle compared to lower life fractions at a particular strain amplitude, **Figure 4.14(b)**. At life fraction $> 10\%$, the material exhibiting the Type-II non-Masing behavior is attributed to the significant change in the internal state of the material and

onset of secondary hardening due to phase transformation and high local heterogeneity [10,42], especially at high strain amplitudes. It should be noted that the martensitic transformation in austenitic stainless steel has been reported to be associated with Type-I non-Masing behavior as well [16,30]. Thus, the martensitic transformation alone may not necessarily cause Type-II non-Masing behavior of materials under fatigue.

4.4.4 Influence of strain hardening rate behavior

As shown in **Figure 4.2(a-c)**, when a material exhibits non-Masing behavior of Type-I, only the proportional stress limit ($\delta\sigma_o$) varies with strain amplitude, whereas the nonlinear part of the hysteresis loops remains almost the same, representable by the master curve (OAB). On the contrary, for the non-Masing behavior of Type-II, as shown in **Figure 4.2(d-i)**, the nonlinear part of the hysteresis loops changes significantly with strain amplitude in addition to $\delta\sigma_o$, due to a significant change in the strain hardening rate behavior at higher strain amplitude. Hence, all the hysteresis loops could not be merged to form the master curve despite all efforts, as shown in **Figure 4.2(d-i)**. The strain hardening rate behavior estimated from the hysteresis loops at 10% and 50% of life fraction has been plotted in **Figure 4.15(a)** and **Figure 4.15(b)**, respectively.

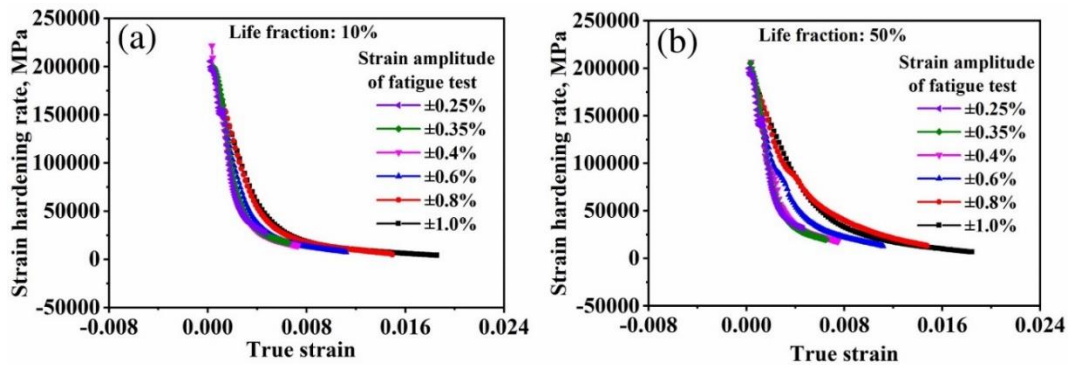


Figure 4.15 Variation of the strain hardening rate behavior with true strain for different strain amplitudes at life fractions of (a) 10% and (b) 50%.

As can be seen in **Figure 4.15**, at the 50% life fraction, the strain hardening rate behavior varies significantly with the different strain amplitudes of the fatigue test. It further appears from **Figure 4.15** that the strain hardening rate behavior remains almost the same at $\pm 0.25\%$, $\pm 0.35\%$, and $\pm 0.4\%$ of strain amplitude; the variation mainly occurs at $\pm 0.6\%$, $\pm 0.8\%$, and $\pm 1.0\%$ of strain amplitude. The strain hardening rate behavior depends on the amount of the martensite, dislocation density, the fraction of SFs, DTs, and interaction between them [166–168]. From **Figure 4.9**, **Figure 4.10**, and **Figure 4.11**, it can be seen that at 8% life fraction, the internal structure of the material mainly consists of dislocations and deformation twins, whereas at 30%

and 50% life fractions, there exist a large number of other defects like dislocation tangles, SFs, SBs, dislocation walls, and some dislocation cell. This high concentration of defects of various kinds (**Figure 4.10(d-i)** and **Figure 4.11(d-i)**) and the high amount of martensite (**Figure 4.1(b)** and **Figure 4.13(b)**) have probably caused the high strain hardening rate behavior, especially at high strain amplitude and high life fraction, causing the non-Masing behavior of Type-II.

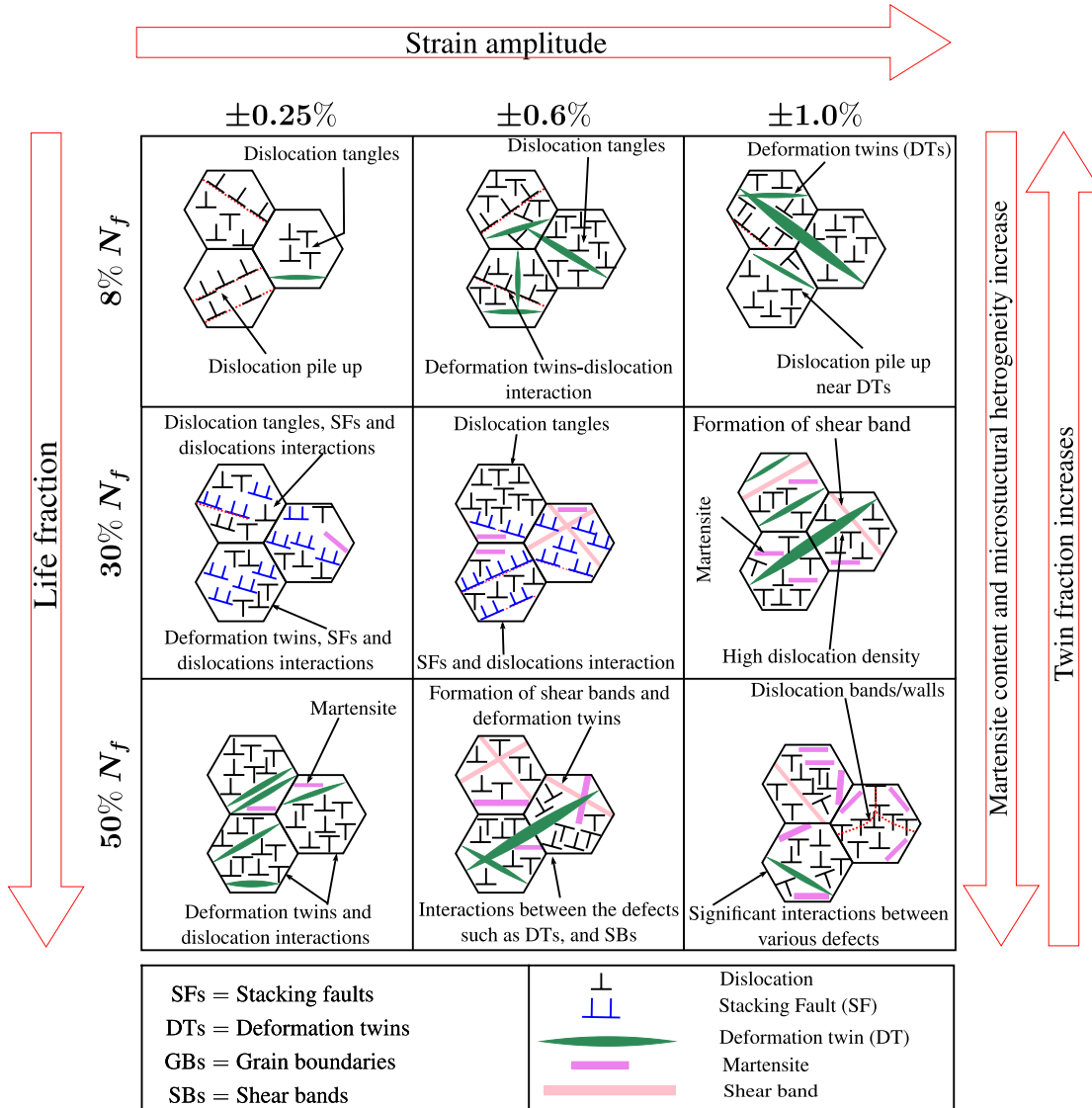


Figure 4.16 Schematic illustration of life fraction and strain amplitude effect on internal state variables of 304L SS fatigue tested at room temperature.

4.5 Qualitative correlation

The observations from the EBSD and TEM analysis, as discussed in **Sections 4.4.3** and **4.4.4**, are summarized in **Figure 4.16**. During the cyclic loading, the generation of the various defects and the possibility of interaction between them depends on the plastic strain (*i.e.* strain amplitude) and the number of cycles (*i.e.* life fraction), thereby leading to Masing or different

types of non-Masing behavior. It is well known that during Masing behavior, the upper loading branches of the hysteresis loops at different strain amplitudes follow the same loading path. Thus, Masing behavior indicates that the material's proportional stress limit and the strain hardening rate behavior do not change with the strain amplitude of the fatigue testing.

Literature [16,25] suggests that the materials that exhibit Masing do not undergo phase transformation, and the internal structure remains almost similar. The findings of the current study on 304L SS, fatigue tested at room temperature, as discussed in **Section 4.4**, are summarized in **Figure 4.17**. In the non-Masing behavior of Type-I, only the proportional stress limit changes, whereas for the non-Masing behavior of Type-II, both the proportional stress limit and the strain hardening rate behavior change with strain amplitude. The differences observed in the internal state of the material have also been highlighted in **Figure 4.17**.

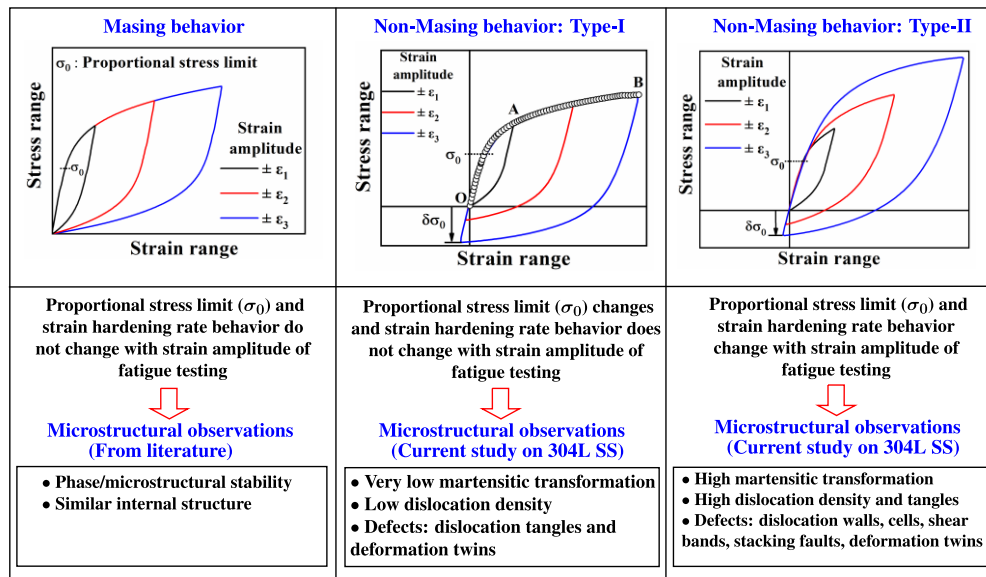


Figure 4.17 Qualitative correlation between the internal state variables and Masing/non-Masing behavior of materials under fatigue loading. Note: ϵ = strain amplitude, $\delta\sigma_0$ = change in proportional stress limit.

In this work, interrupted tests were performed for three life fractions, *i.e.*, 8%, 30%, and 50%, at three different strain amplitudes, *i.e.*, $\pm 0.25\%$, $\pm 0.6\%$, and $\pm 1.0\%$. The qualitative correlation between the material internal state variables and non-Masing behavior has been obtained and presented. As we can not predict the Masing/non-Masing behavior of a material in advance, this article aims to bring the novel findings and observations of the current study to the notice of the researchers. More studies and microstructural investigations on Masing/non-Masing behavior of different materials would be required to better understand the underlying causes

responsible for the transition from Masing to non-Masing or Type-I to Type-II non-Masing behavior.

4.6 Summary and conclusions

Low cycle fatigue test was conducted on AISI 304L SS at room temperature, and analysis of Type-I and Type-II non-Masing behavior and microstructural investigation have been carried out. The following conclusions can be made from the current investigation.

1. A material under low cycle fatigue can exhibit Masing or non-Masing behavior (Type-I or Type-II). Analysis of hysteresis loops reveals that for Masing behavior, the proportional stress limit and strain hardening rate behavior do not change with strain amplitude. However, for the non-Masing behavior of Type-I, only the proportional stress limit changes with strain amplitude, not the strain hardening rate behavior. For the non-Masing behavior of Type-II, both the proportional stress limit and strain hardening rate behavior change with strain amplitude.
 2. The low cycle fatigue testing of 304L SS shows that the material exhibits the Type-I non-Masing behavior up to a life fraction of 10% and Type-II non-Masing behavior beyond the 10% of life fraction.
 3. At 8% of life fraction, the dislocation tangles, deformation twins, and very low (phase fraction <2.5%) amount of martensite have been observed. At higher life fractions (30% and 50%), high dislocation density, stacking faults, deformation twins, shear bands, dislocation walls, dislocation cells, and a high amount of martensite have been observed.
 4. At high life fractions (30% and 50%), the generation of the various type of defects and interaction between them and a high amount of martensitic transformation caused a significant difference in the strain hardening rate behavior at different strain amplitudes and, thereby, non-Masing behavior of Type-II. However, at a low life fraction (8%), the differences in the strain hardening rate behavior are low due to the low fraction of martensite and the absence of various types of defects, except for the deformation twins and dislocation tangles.
 5. The local deformation increased with increasing life fraction due to the high strains developed by martensite transformation at high strain amplitude.
 6. The martensite content (phase fraction) increased, and the twin fraction decreased with life fraction (or fatigue cycling) as twins get consumed during the martensitic transformation, especially at high strain amplitudes of $\pm 0.6\%$ and $\pm 1.0\%$. However, the martensite content and twins fraction did not change significantly at the lower strain amplitude of $\pm 0.25\%$ due to minimal martensitic transformation.
-

7. Although further experimental validation is required, a power-law relationship (of the Coffin-Manson type) seems to exist between the strain amplitude and the number of cycles at the onset of secondary hardening in materials that undergo phase transformation under fatigue.

4.7 Some highlights and remarks

Some highlights of the chapter:

- The non-Masing behavior of 304L SS has been analyzed at different life fractions.
- Change in proportional stress limit only leads to Type-I non-Masing behavior.
- A significant change in strain hardening rate behavior leads to Type-II non-Masing.
- Minimal microstructural heterogeneities were noticed for Type-I non-Masing behavior.
- Severe microstructural heterogeneities were noticed for Type-II non-Masing behavior.

Remarks:

In this chapter, a detailed microstructural investigation of the Type-I and Type-II non-Masing behavior of 304L SS has been carried out. The subsequent chapter deals with the numerical simulation analysis of cyclic plastic deformation and non-Masing behavior of 304L SS.



Chapter – 5

5. Numerical Simulation

5.1 Purpose of investigation

The microstructural investigation of the Masing/non-Masing behavior of 304L SS was conducted at 8%, 30%, and 50% life fractions of fatigue tests conducted at strain amplitudes of $\pm 0.25\%$, $\pm 0.6\%$, and $\pm 1.0\%$, as discussed in the previous **Chapter 4**. It was found that the material internal state variables, such as dislocations, stacking faults, deformation twins, shear bands, dislocation cells, martensite, and local heterogeneity, influence the non-Masing behavior. However, the martensite content (or fraction) was the dominating internal state variable as most of the aforementioned internal state variables transform into martensite at high life fractions and strain amplitudes under LCF [102,165]. Thus, martensite mainly governs/defines the cyclic plastic deformation behavior and, finally, the Type-I and Type-II non-Masing behavior of 304L SS under LCF.

It should be noted that the martensite in austenite can be beneficial or detrimental depending on the phase fraction, martensite morphology (shape and size), and the orientation of martensite with respect to the loading direction. It can so happen that the bulk material deforms elastically; however, local stress goes beyond the material's yield strength owing to the morphology and fraction of the martensite phase in the austenite. The fatigue cracks can nucleate at those high local stress concentration regions. Thus, understanding the role of martensite could help to improve the mechanical properties of the 304L SS under LCF.

Many researchers [169,170] have made efforts to investigate the influence of martensite on cyclic plastic deformation under different loading conditions for different classes of materials using experimental and numerical techniques. Ismail et al. [171] have concluded that the morphology, orientation, and volume fraction of martensite largely influence the material's internal state, leading to significant stress and strain inhomogeneities, which control the damage process in dual-phase (DP) steels. Paul et al. [172] investigated the effect of morphology and phase fraction of martensite on DP steel under LCF and found that the morphology does not significantly influence cyclic hardening/softening deformation, but the martensite fraction does.

However, DP steel's fatigue life decreases as the martensite particle's size increases at different martensite fractions.

For DP steels, Al-Abbasi and Nemes [173] have experimentally investigated the effect of martensite fraction on materials' mechanical properties and also predicted the material behavior by finite element simulation. However, they have not studied the influence of martensite morphology and orientation on the cyclic plastic deformation of DP steel and Masing/non-Masing behavior. Based on an extensive literature review, it can be concluded that the influence of martensite morphology and phase fraction on cyclic plastic deformation has been analyzed for different classes of DP steels. However, to the best of our knowledge, the influence of martensite's phase fraction and morphology on the cyclic plastic deformation behavior of 304L SS has not been analyzed yet. Such a study would provide some characteristic information about the role played by deformation-induced martensite that forms in 304L SS under cyclic loading.

Therefore, an effort has been made to investigate the effect of martensite on the cyclic plastic deformation and, thereby, the Masing/non-Masing behavior of 304L SS under LCF. For this purpose, numerical simulations of the LCF behavior of 304L SS have been performed (will be discussed in **Section 5.3.1**) with different martensite fractions. The results provide a good description/explanation of the cyclic plastic deformation behavior of 304L SS, giving insight into the cyclic stress-strain evolution and distribution of stress, plastic strain, and equivalent plastic strain (PEEQ) inside and between the phases. This study introduces some basic concepts regarding the role played by the hard martensite phase in the cyclic plastic deformation and Masing/non-Masing behaviors of 304L SS.

5.2 Introduction to constitutive modeling

It is a numerical technique to describe the behavior of materials through mathematical models or empirical relationships. The constitutive models have been widely used to predict various materials' behavior under different loading conditions. The unified and non-unified are two kinds of constitutive models available in the literature to simulate the fatigue behavior of materials. The unified constitutive models have recently received much attention due to their capacity to model a wide range of inelastic materials. Armstrong and Frederick [124] have modified Prager's law [174] by using the dynamic recovery term to model the non-linear behavior of materials. Although the Armstrong-Frederick model can predict materials' non-linear response and strain-hardening behavior, it could not accurately capture the cyclic stress-strain response. Later, Chaboche [175,176] proposed a concept of several back stresses by setting its threshold value to predict the non-linear behavior more precisely. Further, Ohno and

Wang [23] have decomposed the back stress into several components, and each component of back stress has a critical state for dynamic recovery to be fully activated. Many other researchers have also developed constitutive models with some modifications to the existing models to account for the complex material behavior [177,178]. As mentioned, there are numerous constitutive models available for simulating the fatigue of materials; however, the Chaboche model has been extensively used by researchers [179,180] to analyze cyclic plastic deformation. Therefore, the Chaboche model (discussed in **Chapter 1**) has been used to investigate the role of martensite on the cyclic plastic deformation behavior of 304L SS under cyclic loading.

5.3 Simulation methodology

5.3.1 2D numerical simulation

The martensite content was measured using the ferritescope at the midpoint of the fatigue tested samples interrupted at the life fractions of 8%, 30%, and 50% at strain amplitudes of $\pm 0.25\%$, $\pm 0.6\%$, and $\pm 1.0\%$, as discussed in **Chapter 4** and shown in **Figure 4.1(b)**. The measured ferrite number (FN) is then converted into the volume fraction of the martensite by using the empirical relationship (martensite fraction (% Vol) = $0.7 \times \text{FN}$) mentioned in the user manual of the ferritescope [181]. The variation of the martensite content with strain amplitude for different life fractions is given in **Table 5.1**. As can be seen, the martensite fraction at 8% life fraction remains almost the same ($\sim 0.45\%$) irrespective of strain amplitude. The two-dimensional (2D) numerical simulation [182] under strain-controlled fatigue was performed at $\pm 0.6\%$ of strain amplitude for 0.45% and 4.34% of martensite fraction, approximately corresponding to 8% and 30% life fractions, respectively. It should be noted that the martensite fraction did not change much from 30% to 50% at $\pm 0.6\%$ of strain amplitude (**Table 5.1**); therefore, no additional simulation was required for 50%. Further, the simulations were performed at $\pm 1.0\%$ of strain amplitude for martensite fractions of 0.45%, 7.84%, and 8.75%, approximately corresponding to 8%, 30%, and 50% of life fraction, respectively. As can be seen in **Table 5.1**, the martensite fraction did not change much with life fractions at the strain amplitude of $\pm 0.25\%$. Thus, we have not considered this strain amplitude for the numerical simulation analysis. The assumptions considered for numerical simulation are as follows.

1. The shape of the martensite phase is assumed to be circular (in 2D) to avoid the stress concentration associated with the other relevant geometries like square, rectangular, or elliptical.
2. The material parameters for the austenite phase have been determined from the initial 50 cycles' test data of 304L SS fatigue tested at room temperature. Thus, the material

parameters can not simulate the significant secondary hardening behavior associated with martensitic transformation at higher life fractions ($>10\%$).

3. The intersection between the martensite phases, defects, the influence of phase boundaries (insignificant compared to the model's size), and the evolution of martensite fraction with cycles have not been considered.
4. The influence of martensite (only the single internal state variable) has been analyzed. The effect of other material internal state variables has not been considered.
5. The influence of morphology (different shapes and sizes) of the martensite and the orientation of different shapes have not been considered.

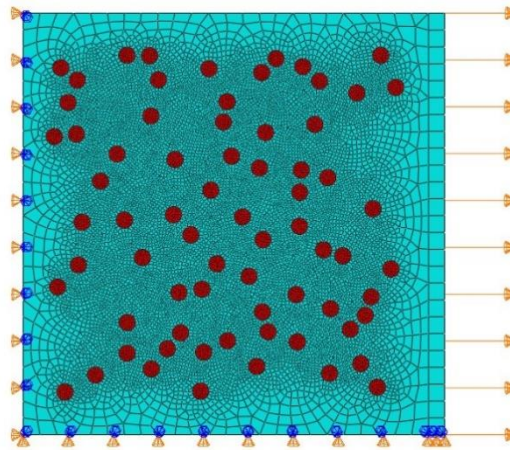


Figure 5.1 Schematic representation of the 2D model and boundary conditions used for numerical simulation of LCF of 304L SS. The circles indicate the martensite phase.

The finite element simulations were performed in ABAQUS using a 2D model with a four-node bilinear, plane strain quadrilateral with reduced integration (CPE4R) elements [183,184]. The 2D model of $5\text{ mm} \times 5\text{ mm}$ dimensions (**Figure 5.1**) with variable mesh size (minimum size: $\sim 0.02\text{ mm}$) has been considered for the analysis. It is sufficiently large to include both the austenite and martensite phases in the model for the simulation. The constitutive behavior of the material is defined by considering the combined non-linear isotropic and kinematic hardening model (popularly known as Chaboche model) [125]. The static implicit simulation was performed with different martensite fractions, where the strain-controlled cyclic loading (for $\pm 0.6\%$ and $\pm 1.0\%$ of strain amplitudes) was employed using a triangular amplitude curve in ABAQUS. All boundary conditions applied for this investigation are schematically shown in **Figure 5.1**. The loading was applied on the right face of the model (**Figure 5.1**), and the opposite face (left) was restricted from rotation and translation along the loading direction, but it can move in the vertical direction. The bottom face was restricted from rotation and translation along the vertical direction, whereas it can move in the loading direction [185,186].

The numerical simulation was performed for the 100 cycles. The stress and plastic strain after the 5th cycle at maximum tensile loading and equivalent plastic strain after the 100th cycle was extracted and analyzed. The stress and strain values were estimated for the austenite phase, martensite phase, and the whole composite model. For the entire model, the strain was calculated by dividing the displacement of the nodes at the loading face by the original length of the model (**Figure 5.1**), and the stress in the loading direction was obtained from the estimates of total force acting on the loading face divided by the total area of the loading face. For the austenite phase (*i.e.*, matrix), the stress and strain were estimated from the element with maximum von Mises stress. Similarly, the stress and strain were obtained from the element with maximum von Mises stress for the martensite phase.

Table 5.1 Martensite fraction (% Vol.) at different fatigue life at different strain amplitudes, measured at the midpoint of gage length of the fatigue tested sample.

Strain amplitude (%)	%Vol. of martensite at 8% life fraction	%Vol. of martensite at 30% life fraction	%Vol. of martensite at 50% life fraction
± 0.25	0.45	0.84	0.64
± 0.6	0.5	4.34	4.31
± 1.0	0.41	7.84	8.75

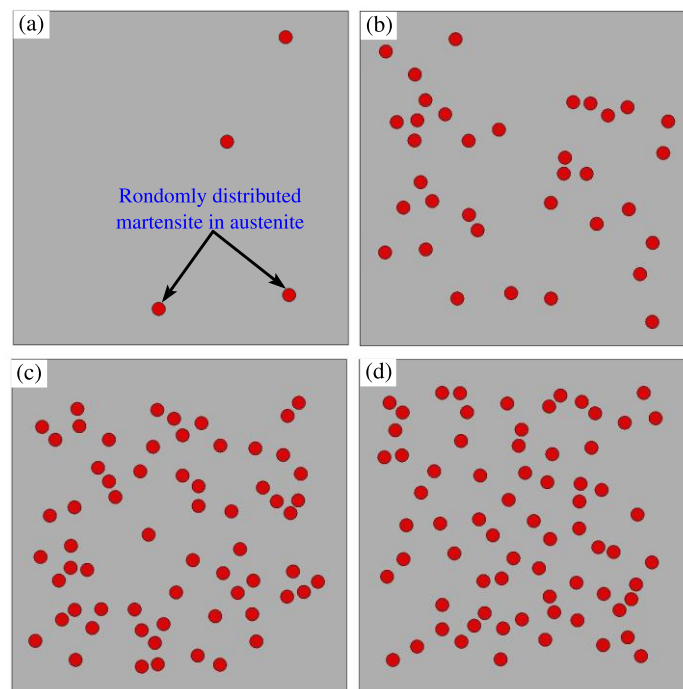


Figure 5.2 Schematic representation of various models considered for the numerical simulation of 304L SS with varying percentages of austenite (A) and martensite (M); (a) 0.45% M + 99.55% A, (b) 4.34% M + 95.66% A, (c) 7.84% M + 92.16% A, and (d) 8.75% M + 91.25% A.

Martensite is commonly found in materials in needle-like and lath structure morphologies [187]. Considering the needle-like shape, the cross-section can be represented by a circle or ellipse on a 2D plane. For simplicity and to avoid the stress concentration expected to be associated with an elliptic geometry, the martensite phase is considered to be of circle shape for the 2D numerical investigation. Sun et al. [188] and Du et al. [189] also used similar morphology of martensite in their numerical study. We used Python code to generate the randomly distributed and required number of martensite particles of 0.1 mm radius in the austenite phase. The size of the martensite has been selected based on the literature observations and the martensite fraction measured experimentally [190]. The number of particles corresponds to the estimated martensite fraction (**Table 5.1**) at the specified strain amplitudes and the life fractions, as shown in **Figure 5.2**. In this investigation, the effect of the interface (*i.e.*, the boundary) between the austenite and martensite phases has not been considered [191].

5.3.2 Combined isotropic and kinematic hardening

Numerous constitutive models are available in the open literature for characterizing material cyclic plastic behavior [123]. However, the Chaboche model [125] has been used widely. Thus, to investigate the influence of martensite on the cyclic plastic deformation response of 304L SS, the combined hardening rule proposed by Chaboche has been used. The Chaboche model can be briefly described by **Equations 1.5 - 1.7** (as described in **Chapter 1**). The expansion and contraction of the yield surface, due to hardening or softening behavior, are modeled through isotropic hardening, whereas the translation of the yield surface due to the evolution of back stress is reflected in the kinematic hardening.

5.3.3 Determination of material parameters

The determination of the material parameters for the Chaboche model is the most critical task for performing the numerical simulation. As mentioned earlier (**Section 5.3.1**), under LCF of 304L SS, a negligible amount of martensite formation has been observed up to the life fraction of ~10%, irrespective of strain amplitude. Thus, the material parameters for the austenite phase have been determined from the first 50 cycle's LCF test data of 304L SS. Specifically, the hysteresis loops at $\pm 1.0\%$ of strain amplitude have been considered. The isotropic hardening parameters (Q and b in **Equation 1.6**) have been determined by determining the increment in yield surface size with the accumulated plastic strain. The kinematic hardening parameters (C and γ in **Equation 1.7**) have been estimated from the stress-strain hysteresis loop data of the first cycle at the strain amplitude of $\pm 1.0\%$. The method of estimating the material

parameters can be found in the articles [130,192]. It should be noted that the material parameters for the martensite phase are taken from the published article [193] available in the literature. The material parameters for austenite and martensite phases are given in **Table 5.2**. The material parameters have been assumed to be the same for all other strain amplitudes considered for the numerical simulation.

Table 5.2 Material parameters of austenite and martensite phases used for the numerical simulation

Material	E (GPa)	ν	σ_y (MPa)	Q (MPa)	b	C (MPa)	γ
Austenite	188.9	0.3	171	76.05	9.69	138710	2134
Martensite [193]	217	0.28	1460	1005	10.22	11680.5	450

5.4 Results and discussion

5.4.1 Hysteresis loop analysis

The material parameters for austenite have been validated by comparing the simulated and experimental hysteresis loops at the strain amplitude of $\pm 1.0\%$, as shown in **Figure 5.3**. The first simulated hysteresis loop slightly deviates from the experimental one, and similar observation can be made for the first ten cycles. It is noted that the hysteresis loop areas are overpredicted by simulation due to deviations in the elastic-to-plastic transition regions of experimental and simulated hysteresis loops. Other researchers have reported similar observations [131] for different materials under strain-controlled fatigue cycling. Such deviations in numerical simulations are often minimized by considering multiple sets of material parameters for the kinematic hardening [194,195]. This is achieved by splitting the highly non-linear behavior of the hysteresis loops into multiple segments. Moreover, the material parameters thus determined can further be optimized by various optimization methods [196,197]. However, as the objective of the current investigation is to understand the role of martensite fraction in the deformation behavior of 304L SS, the material parameters determined directly from the hysteresis loop data have been used without considering multiple segments and optimization.

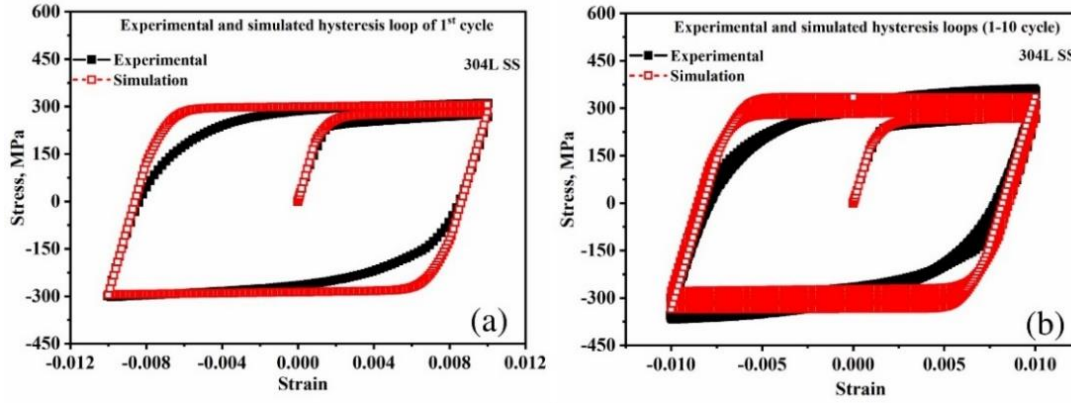


Figure 5.3 Comparison of the simulated and experimental hysteresis loops of 304L SS at $\pm 1.0\%$ of strain amplitude, (a) first hysteresis loop and (b) first ten hysteresis loops.

The hysteresis loops of the austenite and martensite phases have been obtained and analyzed at $\pm 0.6\%$ and $\pm 1.0\%$ of strain amplitudes for different martensite fractions, **Figure 5.4**. Although $\pm 0.6\%$ or $\pm 1.0\%$ strain has been applied to the bulk model, the strain experienced by the martensite phase is significantly low (elastic only) compared to that of the austenite phase, which has undergone elastoplastic deformation, as shown in **Figure 5.4(a)**. Such a massive difference in the deformation behavior of the two phases is the source of local discontinuity in the deformation behavior of 304L SS on a bulk scale. The stress range and strain range experienced by the martensite phase increase significantly with increased martensite content, as shown in **Figure 5.4(b)**. However, the increment in the stress range and strain range experienced by the austenite phase with increased martensite content is very less. Moreover, **Figure 5.4** indicates that the stress range is significantly high in martensite than in austenite. In contrast, the strain accumulation is significantly high in the austenite than in martensite.

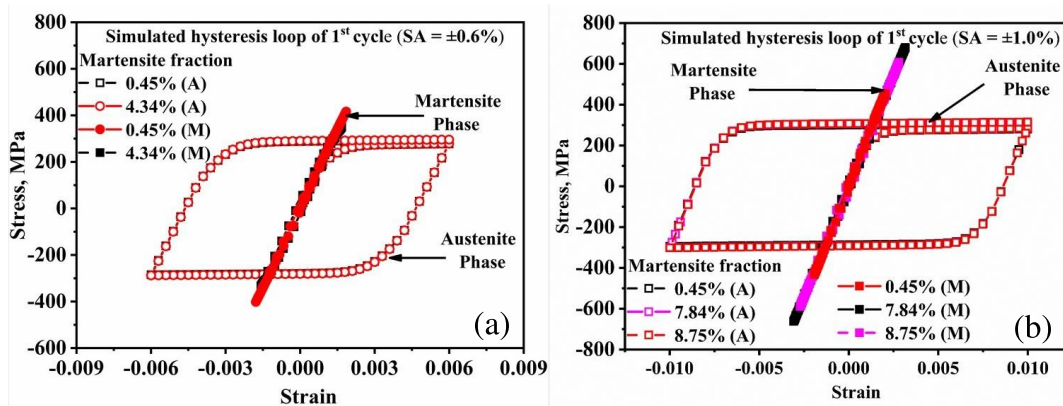


Figure 5.4 Comparison of the simulated hysteresis loop of 1st cycle at (a) $\pm 0.6\%$ and (b) $\pm 1.0\%$ of strain amplitudes for different martensite fractions. Note: Hysteresis loops of austenite (A) and martensite (M) phase are shown.

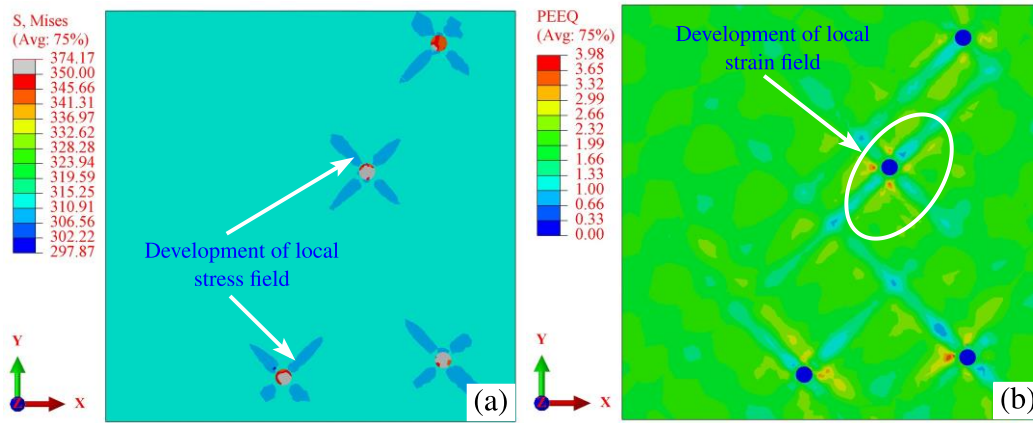


Figure 5.5 The stress/strain fields developed around the martensite phase at $\pm 0.6\%$ of strain amplitude in 304L SS; (a) von Mises stress (MPa) and (b) equivalent plastic strain (PEEQ). Note: X is the loading direction, and the plastic strain is PE11 *i.e.* along X-direction and on a plane normal to X.

The austenite phase surrounding the martensite phase tries to deform plastically; however, as the martensite deforms elastically only, it provides resistance to the deformation of the austenite matrix, and local stress/strain fields are developed around the martensite particles, **Figure 5.5**. The formation of local stress/strain fields increases with increasing the martensite fraction, influencing cyclic plastic deformation behavior and, subsequently, the Masing/non-Masing behavior of 304L SS. The local stress/strain field development and its consequences are discussed in detail in **Section 5.4.4**.

5.4.2 Strain hardening rate

The 1st quarter parts of the simulated hysteresis loops at $\pm 0.6\%$ and $\pm 1.0\%$ of strain amplitude have been analyzed for different martensite fractions, as shown in **Figure 5.6(a)**. **Figure 5.6(b)** shows the magnified view of the plastic region highlighting the strain-hardening behavior. The strain hardening rate increases with an increased martensite fraction irrespective of strain amplitude, **Figure 5.6(b)**. If the martensite fraction remains constant with the given special distribution, the strain hardening rate does not change with strain amplitude, **Figure 5.6(b)**. Researchers [166–168] observed that the strain hardening rate of materials depends on the amount of the martensite, dislocation density, the fraction of SFs, DTs, and interaction between them. In 304L SS, it is observed that the deformation mainly occurs in the austenite phase owing to the low yield strength and high ductility compared to the martensite phase. On contrary, no plastic deformation and high-stress development in the martensite phase are attributed to the high yield strength and extremely low ductility of martensite. Thus, when martensite content increases, a lower volume fraction of austenite must accommodate the

applied strain; thereby, high strain accumulation will occur in austenite. As a result, the material around the martensite particles will get excessively strain-hardened with cycling. Hence the strain hardening rate of the bulk material composed of austenite and martensite phases will also increase with martensite content, as can be seen in **Figure 5.6(b)**

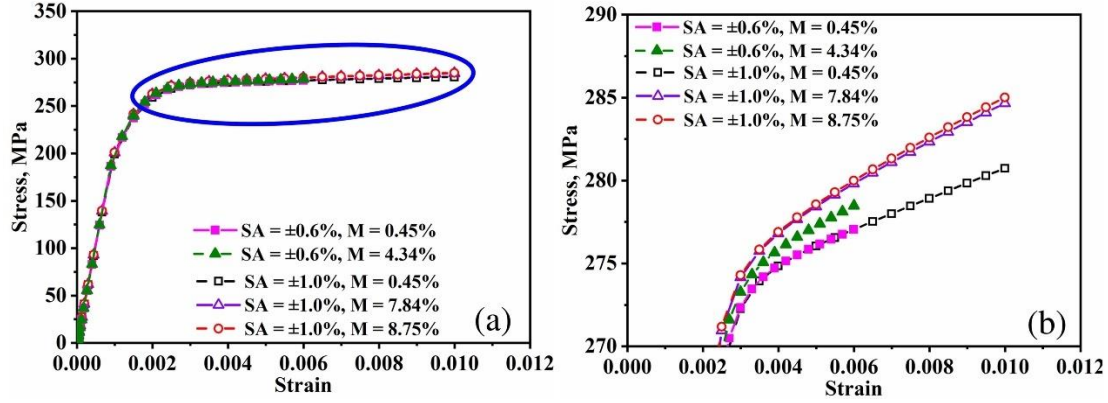


Figure 5.6 (a) First quarter parts of the simulated hysteresis loops at $\pm 0.6\%$ and $\pm 1.0\%$ of strain amplitudes for different martensite fractions (b) magnified view of the plastic region in (a)

5.4.3 Influence of strain amplitude

The variation of plastic strain, stress (von Mises), and equivalent plastic strain distribution with strain amplitude for the same martensite content (0.45%) have been observed in **Figure 5.7**. The plastic strain, stress (von Mises), and equivalent plastic strain increase with increased strain amplitude, **Figure 5.7(a-f)**. The elastic deformation of martensite and elasto-plastic deformation of austenite cause strain incompatibility between the phases. This strain incompatibility causes the development of a high stress/strain field in austenite around the martensite particle, **Figure 5.7(d-e)**. When sufficient numbers of closely spaced particles are present, the heterogeneous distribution of strain/stress in the material leads to the formation of deformation band-like structures in the austenite phase, **Figure 5.7(f)**. These band-like structures represent the regions with excessive strain accumulation due to cyclic loading. Such excessive strain accumulation may lead to the generation of various kinds of defects and can also be potential sites for martensitic transformation [102,165]. Thus, the deformation band-like structure formation may influence the martensitic transformation and, thereby, the non-Masing behavior.

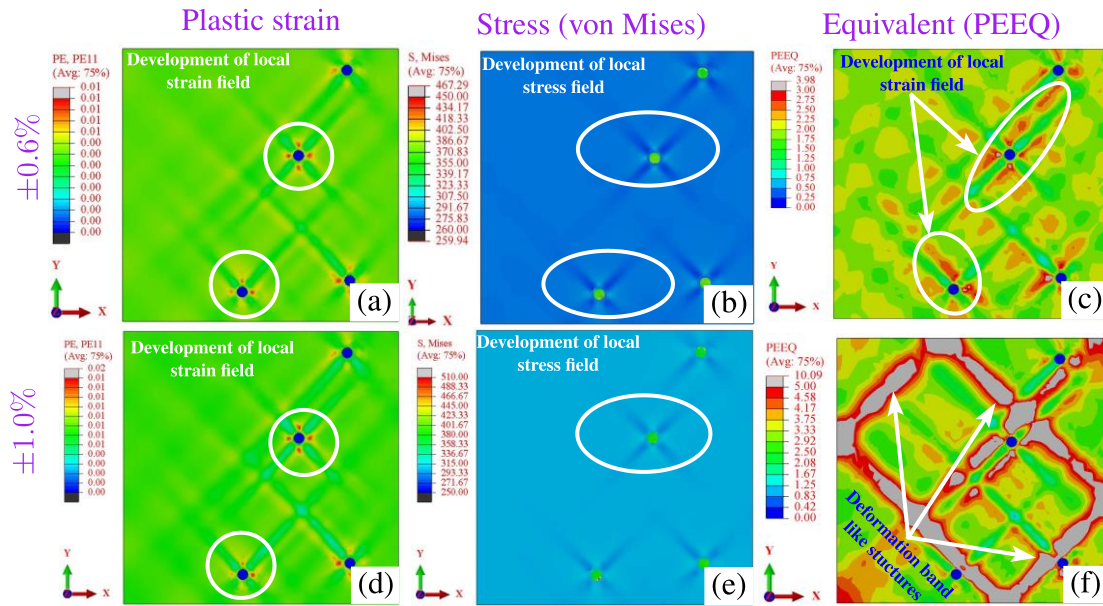


Figure 5.7 Variation of the plastic strain, von Mises stress (MPa), and equivalent plastic strain (PEEQ) distribution for 0.45% martensite fraction at the strain amplitudes of (a-c) $\pm 0.6\%$ and (d-f) $\pm 1.0\%$. Note: X is the loading direction, and the plastic strain is PE11 *i.e.* along X-direction and on a plane normal to X.

5.4.4 Influence of martensite

The influence of martensite on the cyclic plastic deformation and, consequently, the non-Masing behavior of 304L SS has been analyzed at $\pm 0.6\%$ and $\pm 1.0\%$ of strain amplitudes. The plastic strain, stress (von Mises), and equivalent plastic strain increase with increased martensite fraction, **Figure 5.8** and **Figure 5.9**. It is observed that the development of localized stress/strain fields around the martensite phase depends on the distance between two particles, martensite fraction, and applied strain amplitude, as shown in **Figure 5.8** and **Figure 5.9**. Thus, as the martensite fraction increases, the distance between the martensite particle decreases, leading to the development of many high stress/strain regions in austenite. Those high stress/strain fields lead to the formation of deformation band-like structures (**Figure 5.8(c-f)** and **Figure 5.9(c-i)**), thus the generation of various defects, which may further accelerate the rate of martensitic transformation and, subsequently, influence the non-Masing behavior of 304L SS. It should be noted that the development of the stress/strain fields was significantly more at higher martensite fraction and high strain amplitude.

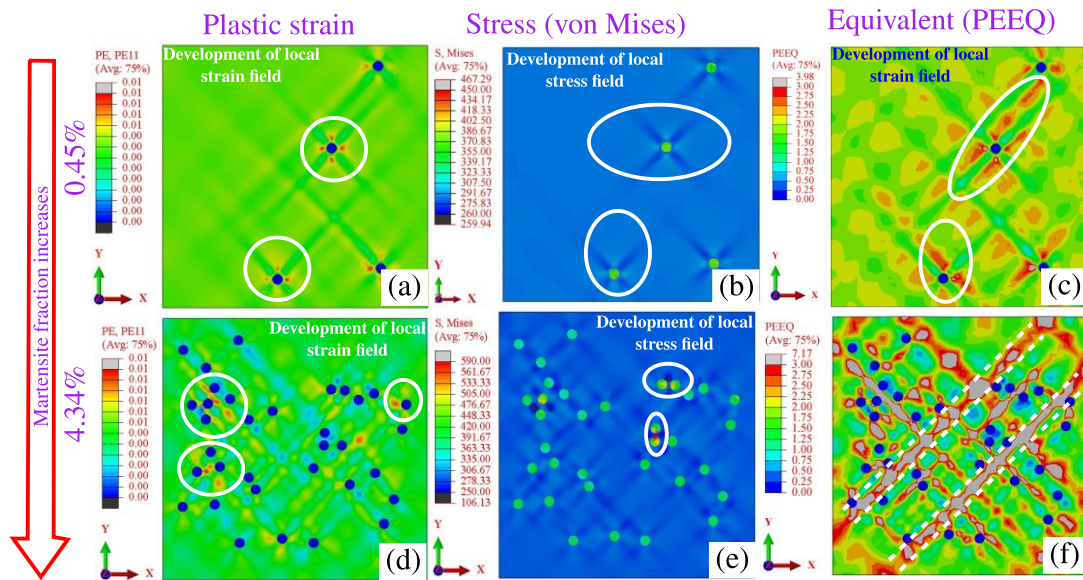


Figure 5.8 Variation of the plastic strain, von Mises stress (MPa), and equivalent plastic strain distribution at $\pm 0.6\%$ of strain amplitude for martensite fractions of (a-c) 0.45% and (d-f) 4.34%. Note: X is the loading direction, and the plastic strain is PE11 *i.e.* along X-direction and on a plane normal to X.

The increase in the deformation band-like structure with increased martensite fraction in the simulation indicates that, in reality, the fraction of martensite will increase with fatigue cycling (or strain amplitude) in 304L SS. This is because the region of the band-like structure indicates the highly strained material, which would preferentially undergo deformation-induced martensitic transformation in 304L SS. Such martensitic transformation in the localized areas would cause a significant change in the strain-hardening rate behavior of the bulk material, contrary to the minimal difference observed by simulation, **Figure 5.6(b)**. The material parameters for the austenite phase have been determined from the LCF test data of the first 50 cycles at $\pm 1.0\%$ strain amplitude. During this period, the cyclic hardening rate is very low compared to the secondary hardening region. In reality, the cyclic hardening behavior of the austenite phase will change with cyclic due to the generation of various defects and an increase in martensite fraction, as mentioned above. This kind of change in material parameters could not be considered in the constitutive equation used for the simulation. Moreover, as mentioned in **Section 5.3.1**, only a single internal state variable (*i.e.*, martensite) has been considered for numerical analysis. The influence of the other material internal state variables, such as stacking faults, deformation twins, shear bands, dislocations, and their mutual interaction, has not been considered. For these reasons, the simulated results in **Figure 5.6(b)** show less difference in the strain hardening rate behavior with strain amplitude (or cycling) for different martensite fractions. Therefore, we can say the strain hardening and heterogeneities in the microstructure

(Figure 5.8(d-f) and Figure 5.9(d-i)) increase with martensite fraction, thereby leading towards the non-Masing behavior of 304L SS under LCF.

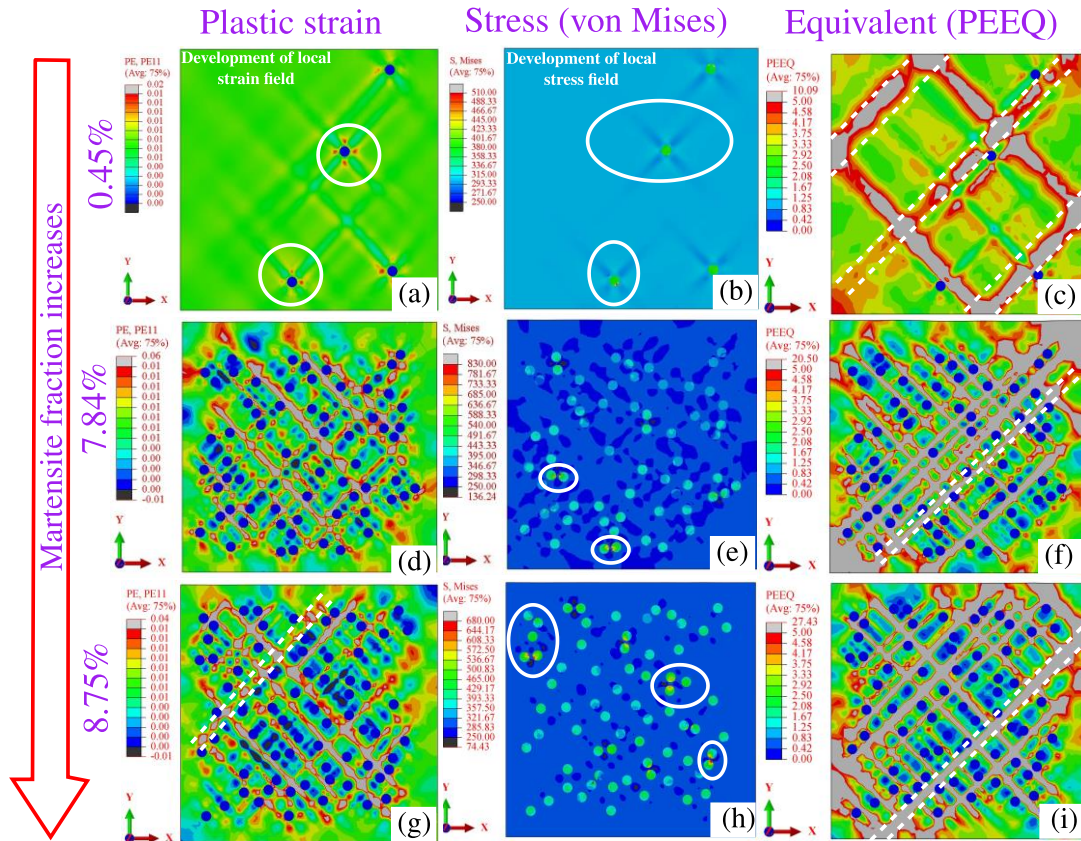


Figure 5.9 Variation of plastic strain, von Mises stress (MPa), and equivalent plastic strain at $\pm 1.0\%$ of strain amplitude for martensite fractions of (a-c) 0.45%, (d-f) 7.84%, and (g-i) 8.75%.

Note: X is the loading direction, and the plastic strain is PE11 *i.e.* along X-direction and on a plane normal to X.

5.5 Cyclic stress response (CSR)

The variation of peak tensile stress with the number of cycles at different strain amplitudes and the martensite fractions is shown in Figure 5.10(a). It is found that the hardening increases with the martensite fraction up to ~ 20 cycles at $\pm 0.6\%$ of strain amplitude, whereas it increases up to only ~ 10 cycles at $\pm 1.0\%$ of strain amplitude. The peak stress value increases as the martensite fraction increases at a particular strain amplitude. The peak tensile stress does not change (*i.e.*, saturates) after a certain number of cycles. This indicates that no further cyclic hardening will occur in the material. However, the LCF experiment of 304L SS shows continuous cyclic hardening (*i.e.*, secondary hardening) until the material fails by fracture. Such deviation is observed as the martensite fraction does not change with cycling in simulation. Moreover, the experimental hysteresis loop shapes at $\pm 1.0\%$ (Figure 5.3(a)) indicate that the kinematic hardening saturates rapidly with plastic strain. In 304L SS, the

martensite fraction will change continuously with cycling due to deformation-induced martensitic transformation [7]. This will cause excessive cyclic hardening, especially at the increased number of cycles. It should be noted that the saturation stage (by simulation) has been achieved in fewer cycles (**Figure 5.10(a)**) at high strain amplitude owing to the higher plastic strain accumulation per cycle compared to that at lower strain amplitude. It is observed (shown in **Figure 5.10(b)**) that the strain accumulated after ten cycles at $\pm 0.6\%$ of strain amplitude is approximately equal to the accumulated strain after 20 cycles at $\pm 1.0\%$ strain amplitude.

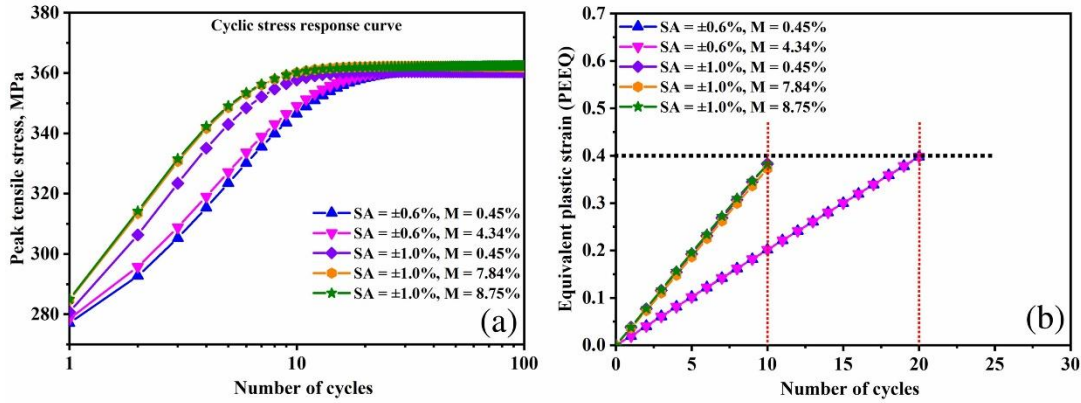


Figure 5.10 (a) The variation of peak tensile stress with martensite fraction for 100 cycles at different strain amplitudes, and (b) variation of the equivalent plastic strain (PEEQ) with the number of cycles for different martensite fractions at $\pm 0.6\%$ and $\pm 1.0\%$ of strain amplitude.

In the present investigation, the influence of martensite on cyclic plastic deformation of 304L SS has been investigated at $\pm 0.6\%$ and $\pm 1.0\%$ of strain amplitude for different martensite fractions. It provides insight into the cyclic stress-strain evolution and distribution of stress, plastic strain, and equivalent plastic strain (PEEQ) inside and between the phases. It should be noted that the other internal state variables, such as dislocations, stacking faults, deformation twins, shear bands, dislocation cells, local heterogeneity, martensite morphology and orientation also influence the cyclic plastic deformation and non-Masing behavior of 304L SS. Therefore, more dedicated experimental and numerical studies are required to further investigate the influence of martensite's morphology, orientation, and other internal state variables on the cyclic plastic behavior and non-Masing behavior of 304L SS under LCF.

5.6 Summary and conclusions

The following conclusions can be drawn from the simulation results-

1. Under low cycle fatigue, the presence of martensite in austenitic 304L SS would cause the development of inhomogeneous strain/stress fields in the material due to strain incompatibility between the martensite and the austenite phases.

2. The strain/stress field intensity increases with the increment in martensite fractions, the distance between the martensite particles, and the amplitude of loading.
3. Interaction of the stress/strain fields around the martensite particles causes the development of the deformation band-like structure in the material. Under fatigue, these deformation band-like structures would act as the nucleation sites for martensitic transformation in 304L SS. This is because those regions undergo higher plastic strain accumulation, representing the creation of many defects of various kinds and possible interaction among them for martensitic transformation.
4. It is observed that the material between the martensite particles undergoes preferential plastic deformation. Therefore, it can be said that once martensite particles are nucleated at multiple locations in 304L SS under fatigue, the interparticle regions will undergo a martensitic transformation, and growth will take place under cyclic loading.
5. The strain localization, equivalent plastic strain, and effective stress increase with the increase in martensite content in 304L SS. This type of plastic strain localization would promote more martensitic transformation and, thereby, changes in the material's strain hardening rate and mechanical properties, leading to non-Masing behavior.

5.7 Some highlights and remarks

Some highlights of the chapter:

- Development of stress/strain field around the martensite phase has been noticed.
- The severity of the stress/strain field depends on the distance between the martensite phase particles, mass fraction, and applied strain amplitude.
- The formation of deformation band-like structures has been observed. The deformation band fraction increases with increased martensite and strain amplitude.
- The deformation band-like structures essentially indicate the region of high-strain accumulation, where in actual specimens, a preferential martensitic transformation would happen, causing non-Masing behavior.

Remarks:

This chapter deals with the influence of martensite on the cyclic plastic deformation and non-Masing behavior of 304L SS. The high strain hardening and more heterogeneity govern the cyclic plastic deformation and non-Masing behavior of 304L SS.



Chapter – 6

6. Conclusions and Scope of Future Work

6.1 Summary and conclusions

The study contributes to a better understanding of the inherent complexities involved in analyzing materials' Masing/non-Masing behavior under low cycle fatigue. The various factors influencing materials' Masing/non-Masing behavior have been identified based on the extensive literature review and analysis. The significance and modeling aspects of Masing/non-Masing behavior concerning the development of the constitutive model have been presented and discussed. The various assessment methods of the Masing/non-Masing analysis has been thoroughly reviewed and discussed with their limitation. A non-dimensional parameter based on the cyclic plastic strain energy density (CPSED), called “Normalized CPSED Difference,” has been proposed to assess materials' Masing/non-Masing behavior. The evolution of the hysteresis loop with strain amplitude has been critically examined and concluded that the non-Masing behavior could be classified into Type-I (construction of master curve is possible) and Type-II (construction of master curve is not possible). Further, a model has been proposed to predict the cyclic plastic strain energy density (CPSED) and, subsequently, the fatigue life of different classes of materials. The model has been validated with 13 different types of materials, including the Masing, Type-I non-Masing, and Type-II non-Masing behaviors. The underlying mechanism of Type-I and Type-II non-Masing behaviors of 304L SS has been identified. Subsequently, the qualitative correlation between the non-Masing behavior and the material's internal state variable has been established. Finally, the influence of deformation-induced martensite on cyclic plastic deformation and non-Masing behavior has been investigated and analyzed using the numerical simulation approach. Although the research findings and conclusions have been written at the end of every chapter, the major contributions/outcomes to the technical literature on Masing/non-Masing behavior are as follows.

1. Strain amplitude, temperature, stacking fault energy, and loading sequence are the important factors that influence materials' Masing/non-Masing behavior under fatigue owing to their influence on the microstructure in materials.
-

2. Bauschinger strain method, probability density function method, change in proportional stress limit method, and cyclic plastic strain energy density method (proposed by the author) are the most popular methods applicable to assess/evaluate the degree of non-Masing behavior. The first two give qualitative information, whereas the last two methods provide a quantitative estimation of the degree of non-Masing behavior.
 3. In the literature, material behavior is classified into two categories: Masing and non-Masing. We discovered a new kind of non-Masing behavior, termed the Type-II non-Masing behavior. Thus, the non-Masing behavior of materials has been classified into two categories, viz. (i) Type-I non-Masing behavior (*i.e.*, when construction of the master curve is possible) and (ii) Type-II non-Masing behavior (*i.e.*, when construction of the master curve is not possible).
 4. A new model is proposed to estimate cyclic plastic strain energy density (CPSED) and predict fatigue life. The model has been validated with 13 different classes of materials, and it is found to give a very good prediction (within a scatter band of 1.2) of CPSED. The materials' fatigue life could also be predicted within a scatter band of 2. The model proposed is simple to implement and can be used for any material irrespective of Masing or non-Masing.
 5. The proposed model quantifies the non-Masing behavior in terms of a strain energy density-based non-dimensional parameter, termed "normalized CPSED difference." This non-dimensional parameter is found to vary almost linearly with strain amplitude for all the materials. Thus, this parameter provides a more general and fundamental definition and quantification of the non-Masing behavior of material compared to those available in the literature. It can be used for all behaviors, such as Masing, Type-I non-Masing, and Type-II non-Masing.
 6. The low cycle fatigue testing of 304L SS shows that the material exhibits the Type-I non-Masing behavior up to a life fraction of 10% and Type-II non-Masing behavior beyond 10%.
 7. At 8% of life fraction, the dislocation tangles, deformation twins, and very low (phase fraction < 2.5%) amount of martensite have been observed. At higher life fractions (30% and 50%), high dislocation density, stacking faults, deformation twins, shear bands, dislocation walls, dislocation cells, and a high amount of martensite have been observed.
 8. At higher life fractions (30% and 50%), the generation of the various types of defects and interaction between them and a high amount of martensitic transformation caused a significant difference in the strain hardening rate behavior at different strain amplitudes and, thereby, non-Masing behavior of Type-II. However, at a low life
-

fraction (8%), the differences in the strain hardening rate behavior are low due to the low fraction of martensite and the absence of various types of defects, except for the deformation twins and dislocation tangles.

9. Analysis of hysteresis loops reveals that for Masing behavior, the proportional stress limit and strain hardening rate behavior do not change with strain amplitude. However, for the non-Masing behavior of Type-I, only the proportional stress limit changes with strain amplitude, not the strain hardening rate behavior. For the non-Masing behavior of Type-II, both the proportional stress limit and strain hardening rate behavior change with strain amplitude.
10. The localization and level of equivalent plastic strain and effective stress increase with the increase in martensite content in 304L SS under fatigue. The strain/stress field intensity increases with the increment in martensite fractions, inter-particle distance, and loading amplitude. The interaction of the stress/strain fields around the martensite particles causes the development of the deformation band-like structure. This type of plastic strain localization would promote more martensitic transformation and, thereby, changes in the material's strain hardening rate behavior and mechanical properties, leading to non-Masing behavior.

6.2 Scope of future work

1. We have investigated the influence of the strain amplitude on the Masing/non-Masing behavior of the 304L SS, strain-controlled fatigue tested at room temperature. This material exhibited Type-II non-Masing behavior, which was not reported earlier in the literature. Thus, more studies should be conducted to understand the role of temperature, initial microstructural state, degree of cold work, and loading conditions on the Masing/non-Masing behavior of 304L SS. Such investigations would help in understanding the Type-II non-Masing behavior in great detail and identifying the internal material changes responsible for the non-Masing behavior.
 2. When a material shows non-Masing behavior, the material parameters change with strain amplitude or other factors causing the non-Masing behavior. Then the simulation of the fatigue behavior of such material becomes difficult. The development of constitutive models for the non-Masing behavior of such material under fatigue has been a challenging issue. This can be accomplished by conducting a comprehensive investigation of the Masing/non-Masing behavior of various materials and investigating the mechanistic and microstructural behavior. The first step forward is the quantification of non-Masing, and is achieved in the current investigation for 304L SS.
-

3. Masing/non-Masing behavior under uniaxial cyclic loading is investigated and reported in the literature. However, Masing/non-Masing behavior under multiaxial, random, and mixed fatigue loading conditions is unexplored. Thus, more research is required in that direction.
 4. A large number of articles have been published in the literature investigating the Masing/non-Masing behavior of materials under different loading and environmental conditions. Thus, it would be useful to generate a database of the Masing/non-Masing behavior of the materials based on the research findings of the published articles. The generation/creation of the material's database for Masing/non-Masing behavior under fatigue is required because it will help researchers/scientists to study/analyze (or explore) the different aspects of non-Masing behavior.
-

References

- [1] J. Bauschinger, On the changes of the elastic limit and the strength of iron by straining in tension and in compression, *Mitth. Aus Dem Mech. Laboratorium Der K. Tech. Hochschule Munchen*. 13 (1886) 1–115.
 - [2] V.G. Masing, Zur Heyn'schen theorie der verfestigung der metalle durch verborgen elastische spannungen., *Wissenschaftliche Veröffentlichungen Aus Dem Siemens-Konzern*. (1923) 231–239. https://doi.org/10.1007/978-3-642-99663-4_17.
 - [3] F. Ellyin, D. Kujawski, Plastic strain energy in fatigue failure, *J. Press. Vessel Technol.* 106 (1984) 342–347. <https://doi.org/10.1115/1.3264362>.
 - [4] S.S. Yadav, S.C. Roy, S. Goyal, A comprehensive review and analysis of Masing/non-Masing behavior of materials under fatigue, *Fatigue Fract. Eng. Mater. Struct.* 46 (2023) 759–783. <https://doi.org/10.1111/ffe.13906>.
 - [5] G. Shi, Y. Gao, X. Wang, Y. Cui, Energy-based low cycle fatigue analysis of low yield point steels, *J. Constr. Steel Res.* 150 (2018) 346–353. <https://doi.org/10.1016/j.jcsr.2018.08.026>.
 - [6] J. Fumfera, J. Džugan, J. Kuželka, R. Procházka, M. Španiel, Strain-amplitude dependent cyclic hardening of 08Ch18N10T austenitic stainless steel, *IOP Conf. Ser. Mater. Sci. Eng.* 179 (2017) 012026. <https://doi.org/10.1088/1757-899X/179/1/012026>.
 - [7] S.S. Yadav, S.C. Roy, J. Veerababu, S. Goyal, Quantitative assessment and analysis of non-Masing behavior of materials under fatigue, *J. Mater. Eng. Perform.* 30 (2021) 2102–2112. <https://doi.org/10.1007/s11665-021-05494-w>.
 - [8] L. Xu, X. Nie, J. Fan, M. Tao, R. Ding, Cyclic hardening and softening behavior of the low yield point steel BLY160: experimental response and constitutive modeling, *Int. J. Plast.* 78 (2016) 44–63. <https://doi.org/10.1016/j.ijplas.2015.10.009>.
 - [9] K.O. Lee, S.B. Lee, A comparison of methods for predicting the fatigue life of gray cast iron at elevated temperatures, *Fatigue Fract. Eng. Mater. Struct.* 39 (2016) 439–452. <https://doi.org/10.1111/ffe.12368>.
 - [10] J. Colin, A. Fatemi, S. Taheri, Cyclic hardening and fatigue behavior of stainless steel 304L, *J. Mater. Sci.* 46 (2011) 145–154. <https://doi.org/10.1007/s10853-010-4881-x>.
 - [11] K.B.S. Rao, M. Valsan, S.L. Mannan, Strain-controlled low cycle fatigue behaviour of type 304 stainless steel base material, type 308 stainless steel weld metal and 304-308 stainless steel weldments, *Mater. Sci. Eng. A*. 130 (1990) 67–82. [https://doi.org/10.1016/0921-5093\(90\)90082-E](https://doi.org/10.1016/0921-5093(90)90082-E).
 - [12] S.G.S. Raman, K.A. Padmanabhan, Influence of martensite formation and grain size on room temperature low cycle fatigue behaviour of AISI 304LN austenitic stainless steel, *Mater. Sci. Technol.* 10 (1994) 614–620. <https://doi.org/10.1179/mst.1994.10.7.614>.
 - [13] M. Šmíd, I. Kuběna, M. Jambor, S. Fintová, Effect of solution annealing on low cycle fatigue of 304L stainless steel, *Mater. Sci. Eng. A*. 824 (2021) 141807. <https://doi.org/10.1016/j.msea.2021.141807>.
 - [14] M.S. Pham, C. Solenthaler, K.G.F. Janssens, S.R. Holdsworth, Dislocation structure evolution and its effects on cyclic deformation response of AISI 316L stainless steel, *Mater. Sci. Eng. A*. 528 (2011) 3261–3269. <https://doi.org/10.1016/j.msea.2011.01.015>.
 - [15] A. Plumtree, H.A. Abdel-Raouf, Cyclic stress-strain response and substructure, *Int. J. Fatigue*. 23 (2001) 799–805. [https://doi.org/10.1016/S0142-1123\(01\)00037-8](https://doi.org/10.1016/S0142-1123(01)00037-8).
 - [16] H. Mughrabi, H.-J. Christ, Cyclic deformation and fatigue of selected ferritic and austenitic steels: specific aspects, *ISIJ Int.* 37 (1997) 1154–1169. <https://doi.org/10.2355/isijinternational.37.1154>.
-

- [17] F. Ellyin, Effect of tensile-mean-strain on plastic strain energy and cyclic response, *J. Eng. Mater. Technol.* 107 (1985) 119–125. <https://doi.org/10.1115/1.3225786>.
 - [18] H.R. Jhansale, T.H. Topper, Engineering analysis of the inelastic stress response of a structural metal under variable cyclic strains, *Cycl. Stress. Behav. Exp. Fail. Predict. ASTM STP 5* (1971) 246–270.
 - [19] S.S. Yadav, S.C. Roy, J. Veerababu, S. Goyal, Prediction of cyclic plastic strain energy density and fatigue life of non-Masing behavior materials without master curve, *Trans. Indian Natl. Acad. Eng.* 7 (2022) 411–416. <https://doi.org/10.1007/s41403-021-00274-3>.
 - [20] S. Sivaprasad, S.K. Paul, N. Narasaiah, S. Tarafder, Experimental investigation on cyclic deformation behaviour of primary heat transport piping materials: Masing analysis of hysteresis loops, *Trans. Indian Inst. Met.* 63 (2010) 559–563. <https://doi.org/10.1007/s12666-010-0082-1>.
 - [21] S. Goyal, S.K. Gupta, S. Sivaprasad, S. Tarafder, V. Bhasin, K.K. Vaze, A.K. Ghosh, Low cycle fatigue and cyclic plasticity behavior of Indian PHWR/AHWR primary piping material, *Procedia Eng.* 55 (2013) 136–143. <https://doi.org/10.1016/j.proeng.2013.03.232>.
 - [22] N. Khutia, P.P. Dey, S.K. Paul, S. Tarafder, Development of non Masing characteristic model for LCF and ratcheting fatigue simulation of SA333 C-Mn steel, *Mech. Mater.* 65 (2013) 88–102. <https://doi.org/10.1016/j.mechmat.2013.05.016>.
 - [23] N. Ohno, J.D. Wang, Kinematic hardening rules with critical state of dynamic recovery, part I: formulation and basic features for ratchetting behavior, *Int. J. Plast.* 9 (1993) 375–390. [https://doi.org/10.1016/0749-6419\(93\)90042-O](https://doi.org/10.1016/0749-6419(93)90042-O).
 - [24] N. Ohno, J.D. Wang, Kinematic hardening rules with critical state of dynamic recovery, part II: application to experiments of ratchetting behavior, *Int. J. Plast.* 9 (1993) 391–403. [https://doi.org/10.1016/0749-6419\(93\)90043-P](https://doi.org/10.1016/0749-6419(93)90043-P).
 - [25] H.J. Maier, P. Gabor, N. Gupta, I. Karaman, M. Haouaoui, Cyclic stress-strain response of ultrafine grained copper, *Int. J. Fatigue.* 28 (2006) 243–250. <https://doi.org/10.1016/j.ijfatigue.2005.05.004>.
 - [26] M. Bayerlein, H.J. Christ, H. Mughrabi, Plasticity-induced martensitic transformation during cyclic deformation of AISI 304L stainless steel, *Mater. Sci. Eng. A.* 114 (1989) L11–L16. [https://doi.org/10.1016/0921-5093\(89\)90871-X](https://doi.org/10.1016/0921-5093(89)90871-X).
 - [27] R. Dey, S. Tarafder, H. Bar, S. Sivaprasad, Correlating effect of temperature on cyclic plastic deformation behavior with substructural developments for austenitic stainless steel, *J. Mater. Eng. Perform.* 29 (2020) 480–496. <https://doi.org/10.1007/s11665-020-04569-4>.
 - [28] S. Goyal, S. Mandal, P. Parameswaran, R. Sandhya, C.N. Athreya, K. Laha, A comparative assessment of fatigue deformation behavior of 316 LN SS at ambient and high temperature, *Mater. Sci. Eng. A.* 696 (2017) 407–415. <https://doi.org/10.1016/j.msea.2017.04.102>.
 - [29] Y. Li, C. Laird, Masing behavior observed in monocrystalline copper during cyclic deformation, *Mater. Sci. Eng. A.* 161 (1993) 23–29. [https://doi.org/10.1016/0921-5093\(93\)90471-P](https://doi.org/10.1016/0921-5093(93)90471-P).
 - [30] S. Sivaprasad, S.K. Paul, A. Das, N. Narasaiah, S. Tarafder, Cyclic plastic behaviour of primary heat transport piping materials: influence of loading schemes on hysteresis loop, *Mater. Sci. Eng. A.* 527 (2010) 6858–6869. <https://doi.org/10.1016/j.msea.2010.07.041>.
 - [31] D. Lefebvre, F. Ellyin, Cyclic response and inelastic strain energy in low cycle fatigue, *Int. J. Fatigue.* 6 (1984) 9–15. [https://doi.org/10.1016/0142-1123\(84\)90003-3](https://doi.org/10.1016/0142-1123(84)90003-3).
 - [32] P.P. Sarkar, P.S. De, S.K. Dhua, P.C. Chakraborti, Strain energy based low cycle fatigue damage analysis in a plain C-Mn rail steel, *Mater. Sci. Eng. A.* 707 (2017) 125–135.
-

- <https://doi.org/10.1016/j.msea.2017.09.035>.
- [33] W. Cui, A state-of-the-art review on fatigue life prediction methods for metal structures, *J. Mar. Sci. Technol.* 7 (2002) 43–56. <https://doi.org/10.1007/s007730200012>.
- [34] L.F. Coffin, A study of the effects of cyclic thermal stresses on a ductile metal, *Trans. Am. Soc. Mech. Eng.* (1954) 931–949. <https://doi.org/10.1115/1.4015020>.
- [35] S. Manson, Behavior of materials under conditions of thermal stress, in: *Natl. Advis. Board Comm. Aeronaut.* 110. Cleveland, OH Lewis Flight Propuls. Lab., 1954.
- [36] O.H. Basquin, The exponential law of endurance tests, in: *Proc Am Soc Test Mater*, 1910: pp. 625–630.
- [37] P. Paris, F. Erdogan, A critical analysis of crack propagation laws, *J. Basic Eng.* 85 (1963) 528–533. <https://doi.org/10.1115/1.3656900>.
- [38] T. Hassan, M. Rahman, Constitutive models in simulating low-cycle fatigue and ratcheting responses of elbow, *J. Press. Vessel Technol.* 137 (2015) 031002. <https://doi.org/10.1115/1.4029069>.
- [39] C. Wang, J. Fan, L. Xu, X. Nie, Cyclic hardening and softening behavior of the low yield point steel: implementation and validation, *Eng. Struct.* 210 (2020) 110220. <https://doi.org/10.1016/j.engstruct.2020.110220>.
- [40] M.S. Pham, S.R. Holdsworth, K.G.F. Janssens, E. Mazza, Cyclic deformation response of AISI 316L at room temperature : mechanical behaviour, microstructural evolution, physically-based evolutionary constitutive modelling, *Int. J. Plast.* 47 (2013) 143–164. <https://doi.org/10.1016/j.ijplas.2013.01.017>.
- [41] C. Laird, Z. Wang, B.T. Ma, H.F. Chai, Low energy dislocation structures produced by cyclic softening, *Mater. Sci. Eng. A.* 113 (1989) 245–257. [https://doi.org/10.1016/0921-5093\(89\)90313-4](https://doi.org/10.1016/0921-5093(89)90313-4).
- [42] J.W. Pegues, S. Shao, N. Shamsaei, J.A. Schneider, R.D. Moser, Cyclic strain rate effect on martensitic transformation and fatigue behaviour of an austenitic stainless steel, *Fatigue Fract. Eng. Mater. Struct.* 40 (2017) 2080–2091. <https://doi.org/10.1111/ffe.12627>.
- [43] R.L. Woolley, The Bauschinger effect in some face-centred and body-centred cubic metals, *Philos. Mag.* 44 (1953) 597–618. <https://doi.org/10.1080/14786440608521038>.
- [44] C.E. Feltner, J.D. Morrow, Microplastic strain hysteresis energy as a criterion for fatigue fracture, *J. Basic Eng.* 83 (1961) 15–22. <https://doi.org/10.1115/1.3658884>.
- [45] G.R. Halford, The energy required for fatigue (Plastic strain hysteresis energy required for fatigue in ferrous and nonferrous metals), *J. Mater.* 1 (1966) 3–18.
- [46] J. Morrow, Cyclic plastic strain energy and fatigue of metals, *Intern. Frict. Damping Cycl. Plast. Am. Soc. Test. Mater.* (1965) 45–86.
- [47] H. Abdel-Raouf, T.H. Topper, A. Plumtree, Cyclic plasticity and Masing behaviour in metals and alloys, *Adv. Res. Strength Fract. Mater.* (1977) 1207–1215. <https://doi.org/10.1016/b978-0-08-022140-3.50076-8>.
- [48] Z. Wang, C. Laird, Relationship between loading process and Masing behavior in cyclic deformation, *Mater. Sci. Eng. A.* 101 (1988) L1–L5. [https://doi.org/10.1016/0921-5093\(88\)90072-X](https://doi.org/10.1016/0921-5093(88)90072-X).
- [49] D. Ye, D. Ping, Z. Wang, H. Xu, X. Mei, C. Xu, X. Chen, Low cycle fatigue behavior of nickel-based superalloy GH4145/SQ at elevated temperature, *Mater. Sci. Eng. A.* 373 (2004) 54–64. <https://doi.org/10.1016/j.msea.2004.01.045>.
- [50] H. Li, H. Jing, L. Xu, Y. Han, L. Zhao, Z. Tang, K. Song, Microstructure mechanism, cyclic deformation behavior of an Fe-Ni-Cr alloy considering non-Masing behavior, *Int. J. Fatigue.* 127 (2019) 537–550. <https://doi.org/10.1016/j.ijfatigue.2019.06.035>.
-

- [51] J. Nellessen, S. Sandlöbes, D. Raabe, Effects of strain amplitude, cycle number and orientation on low cycle fatigue microstructures in austenitic stainless steel studied by electron channelling contrast imaging, *Acta Mater.* 87 (2015) 86–99. <https://doi.org/10.1016/j.actamat.2014.12.024>.
 - [52] D. Ye, S. Matsuoka, N. Nagashima, N. Suzuki, The low-cycle fatigue, deformation and final fracture behaviour of an austenitic stainless steel, *Mater. Sci. Eng. A.* 415 (2006) 104–117. <https://doi.org/10.1016/j.msea.2005.09.081>.
 - [53] M.A. Jameel, P. Peralta, C. Laird, Masing behavior in copper single crystals fatigued under load control, *Mater. Sci. Eng. A.* 297 (2001) 48–53. [https://doi.org/10.1016/S0921-5093\(00\)01275-2](https://doi.org/10.1016/S0921-5093(00)01275-2).
 - [54] J. Liu, C. Chen, Q. Feng, X. Fang, H. Wang, J. Lu, D. Raabe, W. Yang, Dislocation activities at the martensite phase transformation interface in metastable austenitic stainless steel: an in-situ TEM study, *Mater. Sci. Eng. A.* 703 (2017) 236–243. <https://doi.org/10.1016/j.msea.2017.06.107>.
 - [55] D. Molnár, X. Sun, S. Lu, W. Li, G. Engberg, L. Vitos, Effect of temperature on the stacking fault energy and deformation behaviour in 316L austenitic stainless steel, *Mater. Sci. Eng. A.* 759 (2019) 490–497. <https://doi.org/10.1016/j.msea.2019.05.079>.
 - [56] D.T. Pierce, J.A. Jiménez, J. Bentley, D. Raabe, J.E. Wittig, The influence of stacking fault energy on the microstructural and strain-hardening evolution of Fe–Mn–Al–Si steels during tensile deformation, *Acta Mater.* 100 (2015) 178–190. <https://doi.org/10.1016/j.actamat.2015.08.030>.
 - [57] S.K. Varma, V. Caballero, J. Ponce, A. De La Cruz, D. Salas, The effect of stacking fault energy on the microstructural development during room temperature wire drawing in Cu, Al and their dilute alloys, *J. Mater. Sci.* 31 (1996) 5623–5630. <https://doi.org/10.1007/BF01160807>.
 - [58] H. Mughrabi, Dislocation wall and cell structures and long-range internal stresses in deformed metal crystals, *Acta Metall.* 31 (1983) 1367–1379. [https://doi.org/10.1016/0001-6160\(83\)90007-X](https://doi.org/10.1016/0001-6160(83)90007-X).
 - [59] H. Yaguchi, H. Mitani, K. Nagano, T. Fujii, M. Kato, Fatigue-damage evaluation in aluminum heat transfer tubes by measuring dislocation cell wall thickness, *Mater. Sci. Eng. A.* 315 (2001) 189–194. [https://doi.org/10.1016/S0921-5093\(01\)01156-X](https://doi.org/10.1016/S0921-5093(01)01156-X).
 - [60] E.S. Kayali, A. Plumtree, Stress-substructure relationships in cyclically and monotonically deformed wavy slip mode metals, *Metall. Trans. A.* 13 (1982) 1033–1041. <https://doi.org/10.1007/BF02643400>.
 - [61] O. Bouaziz, N. Guelton, Modelling of TWIP effect on work-hardening, *Mater. Sci. Eng. A.* 319–321 (2001) 246–249. [https://doi.org/10.1016/S0921-5093\(00\)02019-0](https://doi.org/10.1016/S0921-5093(00)02019-0).
 - [62] Y.-K. Lee, S.-J. Lee, J. Han, Critical assessment 19: stacking fault energies of austenitic steels, *Mater. Sci. Technol.* 32 (2016) 1–8. <https://doi.org/10.1080/02670836.2015.1114252>.
 - [63] A. Das, Revisiting stacking fault energy of steels, *Metall. Mater. Trans. A.* 47 (2016) 748–768. <https://doi.org/10.1007/s11661-015-3266-9>.
 - [64] Z. Dong, W. Li, G. Chai, L. Vitos, Strong temperature - dependence of Ni - alloying influence on the stacking fault energy in austenitic stainless steel, *Scr. Mater.* 178 (2020) 438–441. <https://doi.org/10.1016/j.scriptamat.2019.12.013>.
 - [65] A. Abbasi, A. Dick, T. Hickel, J. Neugebauer, First-principles investigation of the effect of carbon on the stacking fault energy of Fe-C alloys, *Acta Mater.* 59 (2011) 3041–3048. <https://doi.org/10.1016/j.actamat.2011.01.044>.
 - [66] X. Tian, H. Li, Y. Zhang, Effect of Al content on stacking fault energy in austenitic Fe-Mn-Al-C alloys, *J. Mater. Sci.* 43 (2008) 6214–6222. <https://doi.org/10.1007/s10853-008-2919-0>.
 - [67] S.K. Huang, N. Li, Y.H. Wen, J. Teng, S. Ding, Y.G. Xu, Effect of Si and Cr on stacking fault probability
-

- and damping capacity of Fe-Mn alloy, *Mater. Sci. Eng. A.* 479 (2008) 223–228. <https://doi.org/10.1016/j.msea.2007.06.063>.
- [68] L. Rémy, A. Pineau, B. Thomas, Temperature dependence of stacking fault energy in close-packed metals and alloys, *Mater. Sci. Eng.* 36 (1978) 47–63. [https://doi.org/10.1016/0025-5416\(78\)90194-5](https://doi.org/10.1016/0025-5416(78)90194-5).
- [69] P. Verma, N.C.S. Srinivas, V. Singh, Low cycle fatigue behavior of modified 9Cr-1Mo steel at 300 °C, *Mater. Sci. Eng. A.* 715 (2018) 17–24. <https://doi.org/10.1016/j.msea.2017.12.105>.
- [70] H. Jing, Z. Luo, L. Xu, L. Zhao, Y. Han, Low cycle fatigue behavior and microstructure evolution of a novel 9Cr-3W-3Co tempered martensitic steel at 650 °C, *Mater. Sci. Eng. A.* 731 (2018) 394–402. <https://doi.org/10.1016/j.msea.2018.06.071>.
- [71] E. Watanabe, T. Asao, M. Toda, M. Yoshida, S. Horibe, Relationship between Masing behavior and dislocation structure of AISI 1025 under different stress ratios in cyclic deformation, *Mater. Sci. Eng. A.* 582 (2013) 55–62. <https://doi.org/10.1016/j.msea.2013.06.020>.
- [72] X. Gong, T. Wang, Q. Li, Y. Liu, H. Zhang, W. Zhang, Q. Wang, Q. Wang, Cyclic responses and microstructure sensitivity of Cr-based turbine steel under different strain ratios in low cycle fatigue regime, *Mater. Des.* 201 (2021) 109529. <https://doi.org/10.1016/j.matdes.2021.109529>.
- [73] K. Peng, K. Qian, W. Chen, Effect of dynamic strain aging on high temperature properties of austenitic stainless steel, *Mater. Sci. Eng. A.* 379 (2004) 372–377. <https://doi.org/10.1016/j.msea.2004.03.004>.
- [74] L. Xu, F. Bao, L. Zhao, Y. Han, H. Jing, H. Yu, X. Gong, Characterizing microstructural evolution and low cycle fatigue behavior of 316H austenitic steel at high-temperatures, *J. Nucl. Mater.* 546 (2021) 152758. <https://doi.org/10.1016/j.jnucmat.2020.152758>.
- [75] B. Neding, Y. Tian, J.Y.P. Ko, P. Hedström, Correlating temperature-dependent stacking fault energy and in-situ bulk deformation behavior for a metastable austenitic stainless steel, *Mater. Sci. Eng. A.* 832 (2022) 142403. <https://doi.org/10.1016/j.msea.2021.142403>.
- [76] G. Kumar, H.N. Bar, A. Kumar, S. Sivaprasad, A comparative assessment of cyclic deformation behavior of SA333 Gr-6 steel at ambient and elevated temperatures, *Int. J. Mater. Res.* 110 (2019) 1000–1009. <https://doi.org/doi:10.3139/146.111840>.
- [77] K. Guguloth, S. Sivaprasad, D. Chakrabarti, S. Tarafder, Low-cyclic fatigue behavior of modified 9Cr-1Mo steel at elevated temperature, *Mater. Sci. Eng. A.* 604 (2014) 196–206. <https://doi.org/10.1016/j.msea.2014.02.076>.
- [78] A. Malka-Markovitz, D. Mordehai, Cross-slip in face-centered cubic metals: a general Escaig stress-dependent activation energy line tension model, *Philos. Mag.* 98 (2018) 347–370. <https://doi.org/10.1080/14786435.2017.1406194>.
- [79] C.V. Rao, N.C.S. Srinivas, G.V.S. Sastry, V. Singh, Low cycle fatigue, deformation and fracture behaviour of Inconel 617 alloy, *Mater. Sci. Eng. A.* 765 (2019) 138286. <https://doi.org/10.1016/j.msea.2019.138286>.
- [80] Z. Zhang, Z. Hu, S. Schmauder, B. Zhang, Z. Wang, Low cycle fatigue properties and microstructure of P92 ferritic-martensitic steel at room temperature and 873 K, *Mater. Charact.* 157 (2019) 109923. <https://doi.org/10.1016/j.matchar.2019.109923>.
- [81] Borrego, L.M. Abreu, J.M. Costa, J.M. Ferreira, Analysis of low cycle fatigue in ALMgSi aluminium alloys, *Eng. Fail. Anal.* 11 (2004) 715–725. [https://doi.org/10.1016/0142-1123\(95\)00078-X](https://doi.org/10.1016/0142-1123(95)00078-X).
- [82] S. Nandy, A.P. Sekhar, T. Kar, K.K. Ray, D. Das, Influence of ageing on the low cycle fatigue behaviour of an Al-Mg-Si alloy, *Philos. Mag.* 97 (2017) 1978–2003. <https://doi.org/10.1080/14786435.2017.1322729>.
-

- [83] H.J. Christ, H. Mughrabi, Cyclic stress-strain response and microstructure under variable amplitude loading, *Fatigue Fract. Eng. Mater. Struct.* 19 (1996) 335–348. <https://doi.org/10.1111/j.1460-2695.1996.tb00971.x>.
 - [84] R. Branco, J.D.M. Costa, F. Berto, S.M.J. Razavi, J.A.M. Ferreira, C. Capela, L. Santos, F. Antunes, Low-cycle fatigue behaviour of AISI 18Ni300 maraging steel produced by selective laser melting, *Metals (Basel)*. 8 (2018) 32. <https://doi.org/10.3390/met8010032>.
 - [85] J. Talonen, P. Nenonen, G. Pape, H. Hänninen, Effect of strain rate on the strain-induced $\gamma \rightarrow \alpha'$ -martensite transformation and mechanical properties of austenitic stainless steels, *Metall. Mater. Trans. A*. 36 (2005) 421–432. <https://doi.org/10.1007/s11661-005-0313-y>.
 - [86] Z. Qin, Y. Xia, Role of strain-induced martensitic phase transformation in mechanical response of 304L steel at different strain-rates and temperatures, *J. Mater. Process. Technol.* 280 (2020) 116613. <https://doi.org/10.1016/j.jmatprotec.2020.116613>.
 - [87] R. Dey, S. Tarafder, S. Sivaprasad, Influence of phase transformation due to temperature on cyclic plastic deformation in 304LN stainless steel, *Int. J. Fatigue*. 90 (2016) 148–157. <https://doi.org/10.1016/j.ijfatigue.2016.04.030>.
 - [88] F. Hahnenberger, M. Smaga, D. Eifler, Fatigue behavior and phase transformation in austenitic steels in the temperature range $-60^{\circ}\text{C} \leq T \leq 25^{\circ}\text{C}$, *Procedia Eng.* 10 (2011) 625–630. <https://doi.org/10.1016/j.proeng.2011.04.104>.
 - [89] J. Kaleta, G. Ziętek, Representation of cyclic properties of austenitic steels with plasticity-induced martensitic transformation, *Fatigue Fract. Eng. Mater. Struct.* 21 (1998) 955–964. <https://doi.org/10.1046/j.1460-2695.1998.00086.x>.
 - [90] G. Baudry, A. Pineau, Influence of strain-induced martensitic transformation on the low-cycle fatigue behavior of a stainless steel, *Mater. Sci. Eng.* 28 (1977) 229–242. [https://doi.org/10.1016/0025-5416\(77\)90176-8](https://doi.org/10.1016/0025-5416(77)90176-8).
 - [91] F.-M. Bai, H.-W. Zhou, X.-H. Liu, M. Song, Y.-X. Sun, H.-L. Yi, Z.-Y. Huang, Masing behavior and microstructural change of quenched and tempered high-strength steel under low cycle fatigue, *Acta Metall. Sin. (English Lett.)* 32 (2019) 1346–1354. <https://doi.org/10.1007/s40195-019-00893-4>.
 - [92] I. Nikulin, T. Sawaguchi, A. Kushibe, Y. Inoue, H. Otsuka, K. Tsuzaki, Effect of strain amplitude on the low-cycle fatigue behavior of a new Fe-15Mn-10Cr-8Ni-4Si seismic damping alloy, *Int. J. Fatigue*. 88 (2016) 132–141. <https://doi.org/10.1016/j.ijfatigue.2016.03.021>.
 - [93] G.S. Rao, J.K. Chakravarty, S. Nudurupati, G.S. Mahobia, K. Chattopadhyay, N.C.S. Srinivas, V. Singh, Low cycle fatigue behavior of zircaloy-2 at room temperature, *J. Nucl. Mater.* 441 (2013) 455–467. <https://doi.org/10.1016/j.jnucmat.2013.05.068>.
 - [94] S.C. Roy, S. Goyal, R. Sandhya, S.K. Ray, Analysis of hysteresis loops of 316L(N) stainless steel under low cycle fatigue loading conditions, *Procedia Eng.* 55 (2013) 165–170. <https://doi.org/10.1016/j.proeng.2013.03.237>.
 - [95] P. Verma, N.C.S. Srinivas, S.R. Singh, V. Singh, Low cycle fatigue behavior of modified 9Cr-1Mo steel at room temperature, *Mater. Sci. Eng. A*. 652 (2016) 30–41. <https://doi.org/10.1016/j.msea.2015.11.060>.
 - [96] A. Kundu, D.P. Field, P.C. Chakraborti, Influence of strain amplitude on the development of dislocation structure during cyclic plastic deformation of 304 LN austenitic stainless steel, *Mater. Sci. Eng. A*. 762 (2019) 138090. <https://doi.org/10.1016/j.msea.2019.138090>.
 - [97] X. Liao, Y. Wang, L. Feng, H. Ban, Y. Chen, Fatigue crack initiation and energy-based life analysis for
-

- Q345qD bridge steel at low temperatures, *J. Constr. Steel Res.* 180 (2021) 106571. <https://doi.org/10.1016/j.jcsr.2021.106571>.
- [98] A. Sarkar, B.K. Kumawat, J.K. Chakravarty, Low cycle fatigue behavior of a ferritic reactor pressure vessel steel, *J. Nucl. Mater.* 462 (2015) 273–279. <https://doi.org/10.1016/j.jnucmat.2015.04.015>.
- [99] P. Mallick, N.K. Tewary, S.K. Ghosh, P.P. Chattopadhyay, Effect of cryogenic deformation on microstructure and mechanical properties of 304 austenitic stainless steel, *Mater. Charact.* 133 (2017) 77–86. <https://doi.org/10.1016/j.matchar.2017.09.027>.
- [100] S.G.S. Raman, K.A. Padmanabhan, Effect of prior cold work on the room - temperature low cycle fatigue behavior of 304LN stainless steel, *Int. J. Fatigue.* 18 (1996) 71–79. <https://doi.org/https://www.sciencedirect.com/science/article/pii/014211239500078X>.
- [101] K. Nohara, Y. Ono, N. Ohashi, Composition and grain size dependence of strain induced martensitic transformation in metastable austenitic stainless steels, *Tetsu-To-Hagane/Journal Iron Steel Inst. Japan.* 63 (1977) 772–782. https://doi.org/10.2355/tetsutohagane1955.63.5_772.
- [102] L.E. Murr, K.P. Staudhammer, S.S. Hecker, Effects of strain state and strain rate on deformation-induced transformation in 304 stainless steel: part II. microstructural study, *Metall. Trans. A.* 13 (1982) 627–635. <https://doi.org/10.1007/BF02644428>.
- [103] M. Mansourinejad, M. Ketabchi, Modification of Olson–Cohen model for predicting stress-state dependency of martensitic transformation, *Mater. Sci. Technol.* 33 (2017) 1948–1954. <https://doi.org/10.1080/02670836.2017.1342016>.
- [104] N. Tsuchida, Y. Morimoto, T. Tonan, Y. Shibata, K. Fukaura, R. Ueji, Stress-induced martensitic transformation behaviors at various temperatures and their TRIP effects in SUS304 metastable austenitic stainless steel, *ISIJ Int.* 51 (2011) 124–129. <https://doi.org/10.2355/isijinternational.51.124>.
- [105] V. Shrinivas, S.K. Varma, L.E. Murr, Deformation-induced martensitic characteristics in 304 and 316 stainless steels during room-temperature rolling, *Metall. Mater. Trans. A.* 26 (1995) 661–671. <https://doi.org/10.1007/BF02663916>.
- [106] A. Belattar, L. Taleb, A. Hauet, S. Taheri, Dependence of the cyclic stress-strain curve on loading history and its interaction with fatigue of 304L stainless steel, *Mater. Sci. Eng. A.* 536 (2012) 170–180. <https://doi.org/10.1016/j.msea.2011.12.097>.
- [107] F. Zhou, L. Li, Experimental study on hysteretic behavior of structural stainless steels under cyclic loading, *J. Constr. Steel Res.* 122 (2016) 94–109. <https://doi.org/10.1016/j.jcsr.2016.03.006>.
- [108] Y. Jiang, P. Kurath, An investigation of cyclic transient behavior and implications on fatigue life estimates, *J. Eng. Mater. Technol.* 119 (1997) 161–170. <https://doi.org/10.1115/1.2805989>.
- [109] S.K. Paul, S. Sivaprasad, S. Dhar, S. Tarafder, Key issues in cyclic plastic deformation: experimentation, *Mech. Mater.* 43 (2011) 705–720. <https://doi.org/10.1016/j.mechmat.2011.07.011>.
- [110] M. Heilmaier, H.J. Maier, A. Jung, M. Nganbe, F.E.H. Müller, H.J. Christ, Cyclic stress-strain response of the ODS nickel-base, superalloy PM 1000 under variable amplitude loading at high temperatures, *Mater. Sci. Eng. A.* 281 (2000) 37–44. [https://doi.org/10.1016/S0921-5093\(99\)00739-X](https://doi.org/10.1016/S0921-5093(99)00739-X).
- [111] P. Arora, S.K. Gupta, V. Bhasin, R.K. Singh, S. Sivaprasad, S. Tarafder, Testing and assessment of fatigue life prediction models for Indian PHWRs piping material under multi-axial load cycling, *Int. J. Fatigue.* 85 (2016) 98–113. <https://doi.org/10.1016/j.ijfatigue.2015.12.002>.
- [112] J. Polák, M. Klesnil, The hysteresis loop I. a statistical theory, *Fatigue Fract. Eng. Mater. Struct.* 5 (1982) 19–32. <https://doi.org/10.1111/j.1460-2695.1982.tb01221.x>.
-

- [113] S. Mukherjee, K. Barat, S. Sivaprasad, S. Tarafder, S.K. Kar, Elevated temperature low cycle fatigue behaviour of Haynes 282 and its correlation with microstructure – Effect of ageing conditions, *Mater. Sci. Eng. A.* 762 (2019) 138073. <https://doi.org/10.1016/j.msea.2019.138073>.
 - [114] B. Das, A. Singh, Influence of hydrogen on the low cycle fatigue performance of P91 steel, *Int. J. Hydrogen Energy.* 45 (2020) 7151–7168. <https://doi.org/10.1016/j.ijhydene.2019.12.154>.
 - [115] A.A. Mamun, R.J. Moat, J. Kelleher, P.J. Bouchard, Origin of the Bauschinger effect in a polycrystalline material, *Mater. Sci. Eng. A.* 707 (2017) 576–584. <https://doi.org/10.1016/j.msea.2017.09.091>.
 - [116] H.J. Maier, H.J. Chirst, Modeling of cyclic stress-strain behavior and mechanisms under thermomechanical fatigue conditions, *Int. J. Fatigue.* 19 (1997) 267–274. [https://doi.org/10.1016/S0142-1123\(97\)00022-4](https://doi.org/10.1016/S0142-1123(97)00022-4).
 - [117] S. Sivaprasad, H.N. Bar, S.K. Gupta, P. Arora, V. Bhasin, S. Tarafder, A comparative assessment of cyclic deformation behaviour in SA333 Gr.6 steel using solid, hollow specimens under axial and shear strain paths, *Int. J. Fatigue.* 61 (2014) 76–86. <https://doi.org/10.1016/j.jfatigue.2013.11.005>.
 - [118] N.N. Afanasyev, Statistical theory of fatigue strength of metals (in Russian), Kiev AN USSR. (1953).
 - [119] J. Polak, F. Fardoun, S. Degallaix, Analysis of the hysteresis loop in stainless steels I. austenitic and ferritic steels, *Mater. Sci. Eng. A.* 297 (2001) 144–153. [https://doi.org/10.1016/S0921-5093\(00\)01251-X](https://doi.org/10.1016/S0921-5093(00)01251-X).
 - [120] R.P. Skelton, H.J. Maier, H.J. Chirst, The Bauschinger effect, Masing model and the Ramberg-Osgood relation for cyclic deformation in metals, *Mater. Sci. Eng. A.* 238 (1997) 377–390. [https://doi.org/10.1016/S0921-5093\(97\)00465-6](https://doi.org/10.1016/S0921-5093(97)00465-6).
 - [121] M.A. Bakkar, B. Kanrar, R. Saha, D. Das, High-strain low-cycle fatigue behavior of thermomechanically treated rebar, *J. Fail. Anal. Prev.* 20 (2020) 1029–1037. <https://doi.org/10.1007/s11668-020-00911-z>.
 - [122] J.K. Mahato, P.S. De, A. Kundu, P.C. Chakraborti, Role of stacking fault energy on symmetric and asymmetric cyclic deformation behavior of FCC metals, in: *Struct. Integr. Assessment, Lect. Notes Mech. Eng.* R.V. Prakash, R.S. Kumar, A. Nagesha, G. Sasikala, A.K. Bhaduri, Eds., Springer Singapore, Springer Singapore, 2020: pp. 691–702. https://doi.org/10.1007/978-981-13-8767-8_59.
 - [123] P. Chellapandi, S.C. Chetal, S.B. Bhoje, Application of viscoplastic theory to high temperature design of fast breeder reactor components, *Trans. 14th Int. Conf. Struct. Mech. React. Technol. (SMiRT 14)*, Lyon Fr. (1997) 173–180.
 - [124] C.O. Frederick, P.J. Armstrong, A mathematical representation of the multiaxial Bauschinger effect, *Mater. High Temp.* 24 (1996) 1–26.
 - [125] J.L. Chaboche, Constitutive equations for cyclic plasticity and cyclic viscoplasticity, *Int. J. Plast.* 5 (1989) 247–302. [https://doi.org/10.1016/0749-6419\(89\)90015-6](https://doi.org/10.1016/0749-6419(89)90015-6).
 - [126] S. Bari, T. Hassan, An advancement in cyclic plasticity modeling for multiaxial ratcheting simulation, *Int. J. Plast.* 18 (2002) 873–894. [https://doi.org/10.1016/S0749-6419\(01\)00012-2](https://doi.org/10.1016/S0749-6419(01)00012-2).
 - [127] X. Chen, R. Jiao, Modified kinematic hardening rule for multiaxial ratcheting prediction, *Int. J. Plast.* 20 (2004) 871–898. <https://doi.org/10.1016/j.ijplas.2003.05.005>.
 - [128] M. Abdel-Karim, N. Ohno, Kinematic hardening model suitable for ratchetting with steady-state, *Int. J. Plast.* 16 (2000) 225–240. [https://doi.org/10.1016/S0749-6419\(99\)00052-2](https://doi.org/10.1016/S0749-6419(99)00052-2).
 - [129] N. Suman, S.C. Roy, Cyclic behavior of material after single loading of cavitation peening, *Mater. Today Proc.* 62 (2022) 7480–7486. <https://doi.org/10.1016/j.matpr.2022.03.508>.
 - [130] S.C. Roy, S. Goyal, R. Sandhya, S.K. Ray, Low cycle fatigue life prediction of 316 L(N) stainless steel based on cyclic elasto-plastic response, *Nucl. Eng. Des.* 253 (2012) 219–225.
-

- <https://doi.org/10.1016/j.nucengdes.2012.08.024>.
- [131] J. Zhou, Z. Sun, P. Kanouté, D. Retraint, Experimental analysis and constitutive modelling of cyclic behaviour of 316L steels including hardening/softening and strain range memory effect in LCF regime, *Int. J. Plast.* 107 (2018) 54–78. <https://doi.org/10.1016/j.ijplas.2018.03.013>.
- [132] G. Kang, N. Ohno, A. Nebu, Constitutive modeling of strain range dependent cyclic hardening, *Int. J. Plast.* 19 (2003) 1801–1819. [https://doi.org/10.1016/S0749-6419\(03\)00016-0](https://doi.org/10.1016/S0749-6419(03)00016-0).
- [133] T. Mayama, K. Sasaki, H. Ishikawa, A constitutive model of cyclic viscoplasticity considering changes in subsequent viscoplastic deformation due to the evolution of dislocation structures, *Int. J. Plast.* 23 (2007) 915–930. <https://doi.org/10.1016/j.ijplas.2006.10.003>.
- [134] Z. Li, J. Han, W. Li, L. Pan, Low cycle fatigue behavior of Cr-Mo-V low alloy steel used for railway brake discs, *Mater. Des.* 56 (2014) 146–157. <https://doi.org/10.1016/j.matdes.2013.10.093>.
- [135] A. Buch, Prediction of constant-amplitude fatigue life to failure under pulsating tension by use of the local-strain approach, *Int. J. Fatigue* 12 (1990) 505–512. [https://doi.org/10.1016/0142-1123\(90\)90223-2](https://doi.org/10.1016/0142-1123(90)90223-2).
- [136] X. Wang, W. Zhang, T. Zhang, J. Gong, M.A. Wahab, A new empirical life prediction model for 9–12% Cr steels under low cycle fatigue and creep fatigue interaction loadings, *Metals (Basel)* 9 (2019) 183. <https://doi.org/10.3390/met9020183>.
- [137] J.H. Hwang, G.D. Song, D.W. Kim, Y.H. Huh, B.C. Park, J. Hahn, S.G. Hong, Tensile and fatigue properties of Super304H welded joint at elevated temperatures, *Int. J. Fatigue* 143 (2021) 105989. <https://doi.org/10.1016/j.ijfatigue.2020.105989>.
- [138] K.O. Lee, S.G. Hong, S.B. Lee, A new energy-based fatigue damage parameter in life prediction of high-temperature structural materials, *Mater. Sci. Eng. A* 496 (2008) 471–477. <https://doi.org/10.1016/j.msea.2008.07.035>.
- [139] W. Zhang, T. Jiang, L. Liu, Low cycle fatigue life prediction model of 800H alloy based on the total strain energy density method, *Materials (Basel)* 13 (2020) 76. <https://doi.org/10.3390/ma13010076>.
- [140] K. Golos, F. Ellyin, A total strain energy density theory for cumulative fatigue damage, *J. Press. Vessel Technol.* 110 (1988) 36–41. <https://doi.org/10.1115/1.3265565>.
- [141] S.R. Mediratta, V. Ramaswamy, P. Rama Rao, On the estimation of the cyclic plastic strain energy of dual-phase steels, *Int. J. Fatigue* 10 (1988) 13–19. [https://doi.org/10.1016/0142-1123\(88\)90016-3](https://doi.org/10.1016/0142-1123(88)90016-3).
- [142] H. Wittke, J. Olfe, K.T. Rie, Description of stress-strain hysteresis loops with a simple approach, *Int. J. Fatigue* 19 (1997) 141–149. [https://doi.org/10.1016/S0142-1123\(96\)00059-X](https://doi.org/10.1016/S0142-1123(96)00059-X).
- [143] C.S. Chang, W.T. Pimbley, H.D. Conway, An analysis of metal fatigue based on hysteresis energy, *Exp. Mech.* 8 (1968) 133–137. <https://doi.org/10.1007/BF02326108>.
- [144] W. Song, X. Liu, F. Berto, S.M.J. Razavi, Low-cycle fatigue behavior of 10CrNi3MoV high strength steel and its undermatched welds, *Materials (Basel)* 11 (2018) 661. <https://doi.org/10.3390/ma11050661>.
- [145] L. Fang, W. Zhao, Y. Wei, Q. Zhang, L. Zhang, N. Ali, H. Zhou, H. Wei, Characterization of dislocation structure in a Nb-bearing austenitic stainless steel after low cycle fatigue via TEM and EBSD, *Mater. Res.* 25 (2021). <https://doi.org/10.1590/1980-5373-MR-2021-0401>.
- [146] S.K. Manwatkar, K.S. Kuhite, S.V.S.N. Murty, Metallurgical analysis of failed AISI 304L stainless steel tubes used in launch vehicle applications, *Metallogr. Microstruct. Anal.* 4 (2015) 497–507. <https://doi.org/10.1007/s13632-015-0247-8>.
- [147] R. Kreethi, P. Sampark, G.K. Majhi, K. Dutta, Martensitic transformation during compressive deformation of a non-conventional stainless steel and its quantitative assessment, *J. Mater. Eng. Perform.* 24 (2015)
-

- 4219–4223. <https://doi.org/10.1007/s11665-015-1724-6>.
- [148] A. Fatemi, L. Yang, Cumulative fatigue damage and life prediction theories: A survey of the state of the art for homogeneous materials, *Int. J. Fatigue*. 20 (1998) 9–34. [https://doi.org/10.1016/S0142-1123\(97\)00081-9](https://doi.org/10.1016/S0142-1123(97)00081-9).
- [149] S. Goyal, J. Veerababu, G.V.P. Reddy, R. Sandhya, K. Laha, Assessment of fatigue response of thermally aged reduced activation ferritic-martensitic steel based on finite element analysis, *Mater. High Temp.* 33 (2016) 170–178. <https://doi.org/10.1179/1878641315Y.0000000020>.
- [150] J. Talonen, P. Aspegren, H. Hänninen, Comparison of different methods for measuring strain induced α' -martensite content in austenitic steels, *Mater. Sci. Technol.* 20 (2004) 1506–1512. <https://doi.org/10.1179/026708304X4367>.
- [151] W. Wei, L. Han, H. Wang, J. Wang, J. Zhang, Y. Feng, T. Tian, Low-cycle fatigue behavior and fracture mechanism of HS80H steel at different strain amplitudes and mean strains, *J. Mater. Eng. Perform.* 26 (2017) 1717–1725. <https://doi.org/10.1007/s11665-017-2575-0>.
- [152] A. Das, S. Sivaprasad, P.C. Chakraborti, S. Tarafder, Connection between deformation-induced dislocation substructures and martensite formation in stainless steel, *Philos. Mag. Lett.* 91 (2011) 664–675. <https://doi.org/10.1080/09500839.2011.608385>.
- [153] A. Das, S. Tarafder, P.C. Chakraborti, Estimation of deformation induced martensite in austenitic stainless steels, *Mater. Sci. Eng. A*. 529 (2011) 9–20. <https://doi.org/10.1016/j.msea.2011.08.039>.
- [154] A. Das, Cyclic plasticity induced transformation of austenitic stainless steels, *Mater. Charact.* 149 (2019) 1–25. <https://doi.org/10.1016/j.matchar.2018.12.002>.
- [155] W. Ramberg, W.R. Osgood, Description of stress-strain curves by three parameters, National Advisory Committee for Aeronautics, Washington D.C., 1943.
- [156] N. Tak, J.-S. Kim, J.-Y. Lim, An energy-based unified approach to predict the low-cycle fatigue life of type 316L stainless steel under various temperatures and strain-rates, *Materials (Basel)*. 12 (2019) 1090. <https://doi.org/10.3390/ma12071090>.
- [157] S. Kalnaus, Y. Jiang, Fatigue of AL6XN stainless steel, *J. Eng. Mater. Technol.* 130 (2008) 031013. <https://doi.org/10.1115/1.2931154>.
- [158] S.S. Yadav, S.C. Roy, J. Veerababu, S. Goyal, Type-I to Type-II non-Masing behavior of 304L SS under low cycle fatigue: Material's internal changes, *Int. J. Fatigue*. 175 (2023) 107789. <https://doi.org/10.1016/j.ijfatigue.2023.107789>.
- [159] M. Soleimani, A. Kalhor, H. Mirzadeh, Transformation-induced plasticity (TRIP) in advanced steels: A review, *Mater. Sci. Eng. A*. 795 (2020) 140023. <https://doi.org/10.1016/j.msea.2020.140023>.
- [160] E. Ghassemali, R. Sonkusare, K. Biswas, N.P. Gurao, Dynamic precipitation at elevated temperatures in a dual-phase AlCoCrFeNi high-entropy alloy: an in situ study, *Philos. Mag. Lett.* 98 (2018) 400–409. <https://doi.org/10.1080/09500839.2018.1563728>.
- [161] W. Bleck, X. Guo, Y. Ma, The TRIP effect and its application in cold formable sheet steels, *Steel Res. Int.* 88 (2017) 1700218. <https://doi.org/10.1002/srin.201700218>.
- [162] H. Wang, H. Jing, L. Zhao, Y. Han, X. Lv, L. Xu, Dislocation structure evolution in 304L stainless steel and weld joint during cyclic plastic deformation, *Mater. Sci. Eng. A*. 690 (2017) 16–31. <https://doi.org/10.1016/j.msea.2017.02.090>.
- [163] C.-J. Miao, J. Zheng, X. Gao, Z. Huang, A.-B. Guo, D.-Y. Ye, L. Ma, Investigation of low-cycle fatigue behavior of austenitic stainless steel for cold-stretched pressure vessels, *J. Zhejiang Univ. A (Applied*
-

- Phys. Eng. 14 (2013) 31–37. <https://doi.org/10.1631/jzus.A1200140>.
- [164] M. Pelegatti, A. Lanzutti, E. Salvati, J.S. Novak, F. De Bona, D. Benasciutti, Cyclic plasticity and low cycle fatigue of an AISI 316L stainless steel: Experimental evaluation of material parameters for durability design, *Materials (Basel)*. 14 (2021) 3588. <https://doi.org/10.3390/ma14133588>.
- [165] A. Das, S. Sivaprasad, P.C. Chakraborti, S. Tarafder, Morphologies and characteristics of deformation induced martensite during low cycle fatigue behaviour of austenitic stainless steel, *Mater. Sci. Eng. A*. 528 (2011) 7909–7914. <https://doi.org/10.1016/j.msea.2011.07.011>.
- [166] L. Zeng, X. Song, N. Chen, Y. Rong, X. Zuo, N. Min, A new understanding of transformation induced plasticity (TRIP) effect in austenitic steels, *Mater. Sci. Eng. A*. 857 (2022) 143742. <https://doi.org/10.1016/j.msea.2022.143742>.
- [167] X.F. Fang, W. Dahl, Strain hardening and transformation mechanism of deformation-induced martensite transformation in metastable austenitic stainless steels, *Mater. Sci. Eng. A*. 141 (1991) 189–198. [https://doi.org/10.1016/0921-5093\(91\)90769-J](https://doi.org/10.1016/0921-5093(91)90769-J).
- [168] T. Zhang, J. Tang, S. He, F. Jiang, D. Fu, J. Teng, J. Wang, Kinematical barriers enhanced dislocation strengthening mechanisms in cold-worked austenitic steels, *Scr. Mater.* 226 (2023) 115237. <https://doi.org/10.1016/j.scriptamat.2022.115237>.
- [169] Z.G. Hu, P. Zhu, J. Meng, Fatigue properties of transformation-induced plasticity and dual-phase steels for auto-body lightweight: Experiment, modeling and application, *Mater. Des.* 31 (2010) 2884–2890. <https://doi.org/10.1016/j.matdes.2009.12.034>.
- [170] S.R. Mediratta, V. Ramaswamy, P. Rama Rao, Low cycle fatigue behaviour of dual-phase steel with different volume fractions of martensite, *Int. J. Fatigue*. 7 (1985) 101–106. [https://doi.org/10.1016/0142-1123\(85\)90040-4](https://doi.org/10.1016/0142-1123(85)90040-4).
- [171] K. Ismail, A. Perlade, P.J. Jacques, T. Pardoen, L. Brassart, Impact of second phase morphology and orientation on the plastic behavior of dual-phase steels, *Int. J. Plast.* 118 (2019) 130–146. <https://doi.org/10.1016/j.ijplas.2019.02.005>.
- [172] S.K. Paul, N. Stanford, T. Hilditch, Effect of martensite morphology on low cycle fatigue behaviour of dual phase steels: Experimental and microstructural investigation, *Mater. Sci. Eng. A*. 644 (2015) 53–60. <https://doi.org/10.1016/j.msea.2015.07.044>.
- [173] F.M. Al-Abbasi, J.A. Nemes, Micromechanical modeling of the effect of particle size difference in dual phase steels, *Int. J. Solids Struct.* 40 (2003) 3379–3391. [https://doi.org/10.1016/S0020-7683\(03\)00156-2](https://doi.org/10.1016/S0020-7683(03)00156-2).
- [174] W. Prager, A new method of analyzing stresses and strains in work-hardening plastic solids, *J. Appl. Mech.* 19 (1956) 493–496. <https://doi.org/10.1115/1.4011389>.
- [175] J.L. Chaboche, K.D. Van, G. Cordier, Modelization of the strain memory effect on the cyclic hardening of 316 stainless steel, in: *Trans. Int. Conf. Struct. Mech. React. Technol.*, 1979.
- [176] J.L. Chaboche, On some modifications of kinematic hardening to improve the description of ratchetting effects, *Int. J. Plast.* 7 (1991) 661–678. [https://doi.org/10.1016/0749-6419\(91\)90050-9](https://doi.org/10.1016/0749-6419(91)90050-9).
- [177] D. Kalkhof, M. Grosse, M. Niffenegger, H.J. Leber, Monitoring fatigue degradation in austenitic stainless steels, *Fatigue Fract. Eng. Mater. Struct.* 27 (2004) 595–607. <https://doi.org/10.1111/j.1460-2695.2004.00784.x>.
- [178] X. Chen, R. Jiao, K.S. Kim, On the Ohno-Wang kinematic hardening rules for multiaxial ratcheting modeling of medium carbon steel, *Int. J. Plast.* 21 (2005) 161–184. <https://doi.org/10.1016/j.ijplas.2004.05.005>.
-

- [179] S. Bari, T. Hassan, Anatomy of coupled constitutive models for ratcheting simulation, *Int. J. Plast.* 16 (2000) 381–409. [https://doi.org/10.1016/S0749-6419\(99\)00059-5](https://doi.org/10.1016/S0749-6419(99)00059-5).
 - [180] P. Kumar, A. Singh, Experimental and numerical investigations of cyclic plastic deformation of Al-Mg alloy, *J. Mater. Eng. Perform.* 28 (2019) 1428–1440. <https://doi.org/10.1007/s11665-019-03906-6>.
 - [181] User manual of ferrite meter, Diverse Cambridge England, 2020.
 - [182] S. Ma, X. Zhang, T. Chen, X. Wang, Microstructure-based numerical simulation of the mechanical properties and fracture of a Ti-Al3Ti core-shell structured particulate reinforced A356 composite, *Mater. Des.* 191 (2020) 108685. <https://doi.org/10.1016/j.matdes.2020.108685>.
 - [183] A. Ramazani, K. Mukherjee, A. Abdurakhmanov, U. Prah, M. Schleser, Micro – macro-characterisation and modelling of mechanical properties of gas metal arc welded (GMAW) DP600 steel, 589 (2013) 1–14. <https://doi.org/10.1016/j.msea.2013.09.056>.
 - [184] J. Zhou, A.M. Gokhale, A. Gurumurthy, S.P. Bhat, Realistic microstructural RVE-based simulations of stress-strain behavior of a dual-phase steel having high martensite volume fraction, *Mater. Sci. Eng. A.* 630 (2015) 107–115. <https://doi.org/10.1016/j.msea.2015.02.017>.
 - [185] A.K. Rana, S.K. Paul, P.P. Dey, Effect of martensite volume fraction on cyclic plastic deformation behavior of dual phase steel: Micromechanics simulation study, *J. Mater. Res. Technol.* 8 (2019) 3705–3712. <https://doi.org/10.1016/j.jmrt.2019.06.022>.
 - [186] P. Basu, S.K. Acharyya, P. Sahoo, 2D RVE based micro-mechanical modeling with real microstructures of heat-treated 20MnMoNi55 steel, *Mater. Res. Express.* 5 (2018) 126506. <https://doi.org/10.1088/2053-1591/aadfbf>.
 - [187] E. V. Brusnitsyna, K.A. Badekha, V.I. Grokhovsky, R.F. Muftakhetdinova, Martensite morphology in different types of meteorites, in: 81st Annu. Meet. Meteorit. Soc. 2018, 2018: pp. 6290–6290.
 - [188] X. Sun, K.S. Choi, W.N. Liu, M.A. Khaleel, Predicting failure modes and ductility of dual phase steels using plastic strain localization, *Int. J. Plast.* 25 (2009) 1888–1909. <https://doi.org/10.1016/j.ijplas.2008.12.012>.
 - [189] Z. Du, K. Tang, P. Ferro, Quantitative analyses on geometric shape effect of microdefect on fatigue accumulation in 316L stainless steel, *Eng. Fract. Mech.* 269 (2022) 108517. <https://doi.org/10.1016/j.engfracmech.2022.108517>.
 - [190] N. Switzer, Z. Yu, Austenitic stainless steel cladding interface microstructures evaluated for petrochemical applications, *Weld. J.* 98 (2019) 50S–61S. <https://doi.org/10.29391/2019.98.004>.
 - [191] A.K. Rana, S.K. Paul, P.P. Dey, Effect of martensite volume fraction on strain partitioning behavior of dual phase steel, *Phys. Mesomech.* 21 (2018) 333–340. <https://doi.org/10.1134/S1029959917040070>.
 - [192] P.V.R. Narendra, K. Prasad, E. Hari, V. Kumar, Low-cycle-fatigue (LCF) behavior and cyclic plasticity modeling of E250A mild steel, *Structures.* 20 (2019) 594–606. <https://doi.org/10.1016/j.istruc.2019.06.014>.
 - [193] M.J. Afzal, F. Maqbool, R. Hajavifard, J. Buhl, F. Walther, M. Bambach, Modeling the residual stresses induced in the metastable austenitic stainless steel disc springs manufactured by incremental sheet forming by a combined hardening model with phase transformation, *Procedia Manuf.* 47 (2020) 1410–1415. <https://doi.org/10.1016/j.promfg.2020.04.300>.
 - [194] S.K. Paul, S. Sivaprasad, S. Dhar, M. Tarafder, S. Tarafder, Simulation of cyclic plastic deformation response in SA333 C-Mn steel by a kinematic hardening model, *Comput. Mater. Sci.* 48 (2010) 662–671. <https://doi.org/10.1016/j.commatsci.2010.02.037>.
-

- [195] S. Mal, S. Bhattacharjee, M. Jana, P. Das, S.K. Acharyya, Optimization of Chaboche kinematic hardening parameters for 20MnMoNi55 reactor pressure vessel steel by sequenced genetic algorithms maintaining the hierarchy of dependence, *Eng. Optim.* 53 (2021) 335–347. <https://doi.org/10.1080/0305215X.2020.1726340>.
 - [196] A.H. Mahmoudi, S.M. Pezeshki-Najafabadi, H. Badnava, Parameter determination of Chaboche kinematic hardening model using a multi objective genetic algorithm, *Comput. Mater. Sci.* 50 (2011) 1114–1122. <https://doi.org/10.1016/j.commatsci.2010.11.010>.
 - [197] D. Nejc, S. Iztok, K. Simon, Optimization of Chaboche material parameters with a genetic algorithm, *Materials (Basel)*. 16 (2023) 1821.
-